UNIVERSITY OF CALIFORNIA, SAN DIEGO

Locally Controlled Deeply Saturated Fiber Optic Parametric Amplifiers

A dissertation submitted in partial satisfaction of the
requirements for the degree Doctor of Philosophy

in

Electrical Engineering (Photonics)

by

Ron Reuven Nissim

Committee in charge:

Professor Stojan Radic, Chair
Professor Prabhakar R. Bandaru
Professor Leonid V. Butov
Professor Joseph E. Ford
Professor Shayan Mookherjea

2014

The Dissertation of Ron Reuven Nissim is approved, and it is acceptable in quality and form for publication on microfilm and electronically:

Chair

University of California, San Diego

2014

DEDICATION

For Simon *z”l*, Doris, Carolina *z”l*,

Mordechai, Mariana, and Keren

EPIGRAPH

In our history, one should distinguish between two different things. The distinction is between those who speak and those who act. History is made not in words, but by acts. Only those who act are making history.

David Ben-Gurion

TABLE OF CONTENTS

LIST OF ABBREVIATIONS

BW	Bandwidth
CE	Conversion efficiency
cSHG/DFG	cascaded second harmonic generation / difference frequency generation
DCF	Dispersion compensated fiber
DFF	Dispersion flattened fiber
DFG	Difference frequency generation
DF-HNLF	Dispersion flattened – Highly nonlinear fiber
DSF	Dispersion shifted fiber
EAM	Electro-absorption modulator
ER	Extinction ratio
FCA	Free carrier absorption
FoM	Figure of Merit
FOPA	Fiber optic parametric amplifier
FWM	Four wave mixing
HNLF	Highly nonlinear fiber
ISBT	Inter sub-band transition
MI	Modulation instability
MQW	Multiple quantum wells
MZM	Mach-Zender modulation
NLO	Nonlinear optics
NLS	Nonlinear Schrodinger
NLSE	Nonlinear Schrodinger equation

OEO	Optical-electrical-optical
OPA	Optical parametric amplifier
PCF	Photonic crystal fiber
PePSi	Periodically polled Silicon
PhC	Photonic crystal
PIC	Photonic integrated circuits
PMD	Polarization mode dispersion
PPLN	Periodically polled Lithium Niobate
QED	Quantum electro dynamic
QPM	Quasi phase matching
RF	Radio frequency
RHS	Right hand side
RI	Refractive index
RPE	Reverse proton exchange
SBS	Stimulated Brillouin Scattering
SHG	Second harmonic generation
SMF	Single mode fiber
SPM	Self Phase Modulation
SRS	Stimulated Raman Scattering
TPA	Two photon absorption
WDM	Wavelength Division Multiplexing
WG	Waveguide
XPM	Cross Phase Modulation

LIST OF SYMBOLS

Δk	Phase matching
λ_0	Zero dispersion wavelength
k_i	Wave-vector at wavelength associated with- i
$\chi^{(k)}$	k-th order susceptibility
z	Coordinate along the propagation direction of the fiber
L	Length of the fiber
n_2	Nonlinear refractive coefficient
γ	Nonlinearity coefficient of waveguide (fiber)
D	Dispersion
S	Dispersion slope
S'	Slope derivative
α	Propagation loss
a	Core radius
β	Propagation constant
σ	Standard-variation of the zero-dispersion wavelength along the fiber
$\Delta\lambda$	Signal-Pump detuning
P	Pump power
P_{ON}	Pump power at the output of the fiber in presence of an input signal
P_{OFF}	Pump power at the output of the fiber in absence of an input signal
P_{SIG}	Signal input power

LIST OF FIGURES

LIST OF TABLES

ACKNOWLEDGMENTS

I would like to acknowledge Professor Stojan Radic for accepting me to his laboratory and for allowing me to work with him. Attending UC San Diego as an international student was truly a life-changing experience. I could not have asked for a better advisor, with a brilliant mind and personality, who is also motivating and supporting. His professional and scientific approach will continue to serve me as an inspiration in my future life.

To the many members and visitors of the photonic systems group, from September 2009 to August 2014, it was a pleasure to meet, chat, and work with each and every one of you. You have provided me with pleasant, multicultural, intellectual, and challenging environment. This is a great group to practice one of my many mottos: "study, learn, and do fun science"; I enjoyed growing professionally in this group and hope I was able to successfully provide you with a similar feeling. I would like to acknowledge my closer collaborators Ana Pejkic and Evgeny Myslivets.

I would like to acknowledge Prof. Dan Marom of the Hebrew University who enabled the connection between me and Prof. Radic. I would like to acknowledge Matthew de Stadler, who made my transition to the United States of America as easy as possible and for being an excellent roommate and a friend.

I would like to express my deep appreciation to my family at home, who always cheered and supported me, including my will to study abroad, one of the most unselfish deeds family members can do. I would like to express special thanks for Nancy Plummer, my future mother-in-law, who made me feel at home away from home. Lastly I would like to acknowledge Rachel Plummer, my bright and amazing

bride, who for the past four years not only accompanied me through the journey of graduate school but provided me companionship, love, and support; and who I so lucky to have in my life. I simply cannot imagine going through this experience without her. I would also like to acknowledge Rachel for patiently proof reading over eighty percent of the text in this dissertation, not including Chapter 2.

Chapter 3, in part or in full, has been submitted for publication of the material as it may appear in IEEE/OSA Journal of Lightwave Technology, 2014, Ron R. Nissim, Evgeny Myslivets, and Stojan Radic. The dissertation author was the primary investigator, and a primary co-author of this article.

Chapter 4, in part or in full, has been submitted for publication of the material as it may appear in OSA Optics Express, 2014, Ron R. Nissim, and Stojan Radic. The dissertation author was the primary investigator, and the primary author of this article.

Chapter 5, in part, is currently being prepared for submission for publication of the material. Ron R. Nissim, Ana Pejkic, Evgeny Myslivets, Nikola Alic, and Stojan Radic. The dissertation author was the primary investigator, and the primary author of this material.

Chapter 5, in part, is a reprint of material as it appears in *Science* **345**(6195), 417-419 (2014), Ron Nissim, Ana Pejkic, Evgeny Myslivets, Bill P. Kuo, Nikola Alic, and Stojan Radic. The dissertation author was a co-primary investigator.

VITA

1983	Born, Tel Aviv, Israel.
2001-2004	Military service.
2007	B. Sc., Physics, Ben Gurion University, Beer Sheva, Israel.
2010	M.Sc., Applied Physics, Hebrew University, Jerusalem, Israel.
2014	Ph.D., Electrical and Computer Engineering (Photonics), University of California, San Diego, California.

PUBLICATIONS

R. Nissim*, A. Pejkic*, E. Myslivets, B. P. Kuo, N. Alic, and S. Radic, "Ultrafast optical control by few photons in engineered fiber," *Science* **345**(6195), 417-419 (2014).
*Equal contribution

R. R. Nissim, E. Myslivets, and S. Radic, "Performance Limits of Inhomogeneous Fiber Optic Parametric Amplifiers Operated in Saturated Regime" (Accepted).

A. Pejkic, R. R. Nissim, E. Myslivets, A. O. J. Wiberg, N. Alic, and S. Radic, "All-Optical Switching in a Highly Efficient Parametric Fiber Mixer: Design Study" (Submitted).

R. R. Nissim and S. Radic, "Response Enhancement of Deeply Saturated Fiber Optic Parametric Amplifier via Inhomogeneous Fiber" (Submitted).

R. R. Nissim, A. Pejkic, E. Myslivets, N. Alic, and S. Radic, "Origin of non-Reciprocal Response in Fiber Optics Parametric Amplifiers" (In preparation).

A. O. J. Wiberg, E. Myslivets, R. R. Nissim, A. Danicic, D. J. Blessing, B. P.-P. Kuo, and S. Radic, "Linearized Parametric Gate for Real-Time Photonic-Sampled Analog-to-Digital Conversion," in *Proc. OFC OThW5*, Los Angeles, 2011.

ABSTRACT OF THE DISSERTATION

Locally Controlled Deeply Saturated Fiber Optic Parametric Amplifiers

by

Ron Reuven Nissim

Doctor of Philosophy in Electrical Engineering (Photonics)

University of California, San Diego, 2014

Professor Stojan Radic, Chair

A new class of highly efficient Optical Parametric Amplifiers (OPA) is explored in this dissertation, which have the potential to reduce the power requirement on the pump and enable new functionalities. This originates from the simple notion that figure of merit (FoM) of an OPA is proportional to the product of the pump power and amplifier's length and nonlinearity. Silica fibers have been developed for over five decades and offer unparalleled transparency. By merely extending the fiber, i.e. the amplifier's length, a high FoM amplifier can be formed while keeping the pump at a

moderate, sub-Watt power level. Unfortunately, optical fibers are inherently non-uniform. Their core size fluctuates along the fiber on a nanometer scale which is on the order of the fiber's molecular constituents. It is currently established that the performance of a fiber-based OPA (FOPA) is dictated by its stochastic nature. In fact, given a moderate pump power level, the highly efficient OPA will be required to maintain a strict phase matching condition across hundreds of meters. Facing this challenge, this dissertation focuses on a locally-controlled, high FoM FOPA.

A high FoM FOPA operates in the deeply saturated regime in which a weak signal saturates the amplifier and depletes the pump power, effectively generating an inverse response of the pump output power to the signal input power. Given FOPAs' *inhomogeneous nature*, the performance limit of deeply saturated FOPAs is studied. So far, FOPAs have been commonly treated as a uniform entity; however, this study discovers unique features of the system which originate from and are strongly influenced by the fiber's inhomogeneous nature. One major example is the non-reciprocal response of deeply saturated FOPAs.

It was found that deeply saturated FOPAs perform very highly, as the pump can respond to a rapidly varying (sub-THz) weak (sub-μW) signal. This is a novel method which obtained orders of magnitude improvement over current alternative technologies and relies on spectrally uninhibited construction in an open architecture. Successful ways to harness local dispersion are bound to benefit both science and engineering by enabling access to highly efficient FOPAs' full potential and creating viable technology.

Chapter 1

Introduction

1.1. Background

The origin of this dissertation dates back to recent points in history. One is the study of nonlinear optics (NLO) [1] which was proliferated by the invention of the laser [2]. The second is the invention of low loss optical fibers [3] which enabled today's fiber-optic communication systems [4]. Fiber-optic communication systems have experienced major changes since their early days in the mid-seventies. In the past forty years, lightwave systems evolved through several generations. These changes include: replacing multi-mode with single-mode fibers; lowering fibers' propagation loss and dispersion; developing faster integrated circuits (ICs); introducing optical amplifiers' and developing WDM techniques. Presently, the main challenge of the field focuses on sustainable growth of optical communication networks. This growth is driven by the continuously increasing number of users and high bit-rate applications. This challenge is addressed at two levels: Increasing the energy efficiency of (sub-) systems and extending their capacity-distance product.

Currently, the capacity-distance product limit of fiber-optics communication systems continues to be pushed further by the development of complex optical modulation techniques; PIC (which is also relevant for energy consideration); SDM; coding methods (ECC/FEC), and by flexible and efficient use of the network resources

in the form of network virtualization (SDN). On the other hand, this work aims to enable reduction in complexity and power consumption of the next generation of high speed optical communication systems, and may also impact areas outside of optical communication.

This dissertation pertains to two concurrent challenges in the optical communication industry. One is the growing gap between optical transmission data rates and electrical signal processing speed. There is a growing demand for faster networks due to the continuous increase in the number of users and the type of content they consume, which consequently requires improvement in network design and infrastructure. For example, previous changes were driven by the transition from stationary to mobile devices and from plain text to high-definition content. While optical waves are used to transmit data, the routing at the junctions of the network is done in the electrical domain. At the junctions, the incoming optical signal is converted into the electrical domain where the signal is processed, which is followed by conversion of the post processed electrical signal back to the optical domain for further transmission, commonly known as OEO architecture [5]. The growing data rate and complexity (complex modulation formats) of the optical signal [6], which is orders of magnitude faster than the electrical domain, makes the two domains incompatible with each other. Consequently, OEO solutions become increasingly complex and of a higher power consumption. Additional power consumption is incurred by the tendency of RF waveguides and devices to operate inefficiently with increased dissipation at higher frequencies.

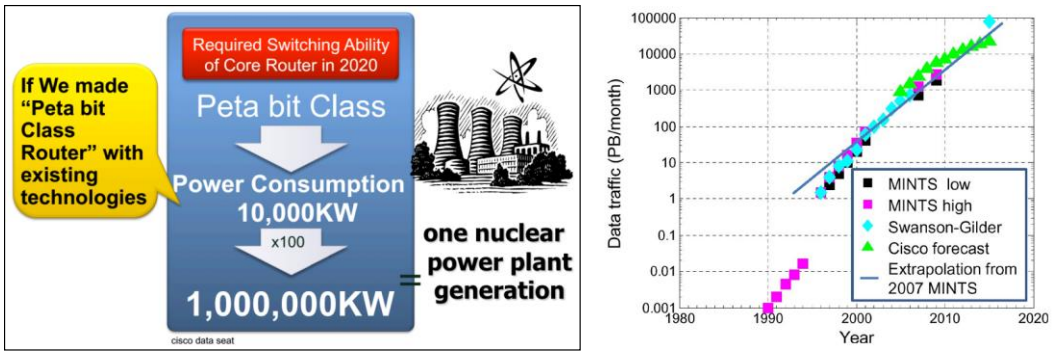

Figure 1: Sustainability Challenge in Optical Communication | Current routing technology cannot support sustainable internet growth (**left**) Power consumption of Peta bit Class Router; after reference [7] © 2010 NICT. (**right**) North American internet traffic; after reference [8] © 2012 IEEE.

The second challenge concerns the growth rate of internet networks and their associated power consumption, which as shown in Figure 1, is not sustainable [7], [9]. Consequently this motivates the exploration for energy efficient technologies. One aspect of the solution to telecommunication's energy crisis is to minimize the power consumption of various power consuming elements in the network, such as modulators, receivers, amplifiers, switches, etc. The other aspect is their speed of operation. Namely, any future solution must have compatible processing speed and lower power consumption.

For example, it will be highly desirable to switch or process the optical signal without the need to convert it to the slow and highly dissipative electrical domain. All optical switching and signal processing have been proposed as a potential replacement for OEO configuration and such investigation was underway by 1990 [10]. The idea is obviously not to replace electronics completely but to use these solutions where it is suitable. In the literature it is occasionally referred to as O/O architecture. The premise of this proposition is to directly manipulate the optical beam carrying the data, thus avoiding the conversion of the optical signal to electrical domain. This technology is

based on NLO where optical beams can efficiently interact inside a nonlinear optical medium. Generally the NLO interactions can be divided into two types: resonant and non-resonant, where the latter has a faster response but requires higher optical intensity and vice versa for the resonant NLO. Additionally, resonant NLO incurs absorption loss. Section 1.3 provides a review on a variety of platforms and technologies.

This work explores a type of non-resonant NLO effect, known as parametric amplification; specifically, four waves mixing (FWM). NLO platforms are typically divided into bulk crystal, chip scale waveguides and fiber based platforms. The various platforms are compared by evaluating their Figure of Merit (FoM). A basic expression to the FoM of an optical parametric amplifier (OPA) is given by the product of the pump power P and the amplifier's nonlinear coefficient γ and length L. Other versions of FoM may include dispersion and parasitic effects such as two photon absorption (TPA) and free carrier absorption (FCA) [11]. NLO crystal offers no optical beam confinement, and consequently the beam divergence limits the interaction length [12], [13], which is typically compensated for by the use of high optical power. In contrast to free space optics, waveguides confine the beam size, and thus support longer interaction length. Still, relative to fibers, chip scale platforms are considered short, millimeter- to centimeter- long waveguides, with core material made of high nonlinearity coefficient and small core size to obtain high intensities. Unfortunately, such waveguides typically suffer from high (linear) propagation loss (~dB/cm) and parasitic effects (nonlinear photon absorption), which limit their length. On the other hand, silica fiber based OPAs are characterized with unparalleled low

propagation loss (< 0.2 dB/km) which, despite their relatively low nonlinear coefficient, can achieve superior nonlinear interaction length in comparison with chip scale waveguide and other competing technologies (see Section 1.3). In some cases, amplifiers are placed in a cavity to enhance their light-matter interaction; however this adds a spectral constraint which limits their speed of operation.

Having been developed for over four decades, silica fibers possess highly controlled low dispersion, specifically in the region of interest – the telecom band. By utilizing the unparalleled transparency of silica fibers, it is possible to extend the amplifier's length and reach very high FoM while keeping the pump at a moderate, sub-Watt, power level. In fact, given a power-limited pump, silica fibers can provide the highest FoM. A very high FoM OPA operates in a deeply saturated regime where a weak signal can saturate the amplifier and deplete the pump. If properly designed, such an OPA can provide very high performance in terms of: power consumption, efficiency, sensitivity, and response time. Silica's near-instantaneous response [14] in such a high performance device could be exploited for diverse applications such as: sensors, novel modulators, switches, amplifiers, receivers, etc.

Fibers in general and silica fibers specifically are commonly treated as a longitudinally uniform structure, which usually is indeed a practical description. Unfortunately, a silica fiber is not an absolute uniform entity. Minute random variations are created along the fiber during the fiber-drawing process, and are also due to fiber handling in the form of twists and pressure points; consequently, the OPA experiences performance degradation [15]. Longitudinal variations in the fiber's transverse core geometry generate a *local* dispersion in the fiber and have a local

affect on the amplification process in the OPA (see Section 1.2.1). It will therefore be important to quantify this effect and establish engineering rules necessary for the construction of high FoM Fiber OPA (FOPA). This work studies the physical limits of such a system and its future potential. Developing such a device will be a far reaching contribution to the creation of highly efficient parametric amplifiers. Such a device can act as a building block for various applications: it will consume less power; amplify light more efficiently; and exhibit unparalleled combination of high sensitivity and high speed.

From the technological perspective, this work is studying the feasibility of utilizing highly nonlinear fiber (HNLF) based OPAs as a platform for ultrafast few photons control. The premise is that by operating the system in a spectrally uninhibited manner, it will be possible to manipulate the FOPA using a rapidly varying, weak control beam. In practical terms, the goal is to control a device using only a few photons at speed rates compatible with the next generation of optical communication. The scientific aspect of this work is the study of FWM in a FOPA which operates in the deeply saturated regime while taking into account vacuum noise[1] and the FOPA's inhomogeneous nature.

[1] Section 1.2.2 and Chapter 3 include information on the importance of vacuum noise in high FoM FOPAs.

1.2. Challenges

This section details the challenges in the research of deeply saturated FOPAs. As this is a new research topic, it involves many challenges, scientific as well as technical, and therefore can grow in many directions. The following paragraphs describe scientific challenges which are most relevant to this work, whereas the rest may be found at Section 6.2 (Future Directions). Technical challenges are described in the body of this dissertation, each at their relevant section.

1.2.1. Local Dispersion in Distributed Amplification

A FOPA is typically described as a lumped device. That is one which has a short (< 100 m) length and has a fixed gain coefficient, g_0. Indeed, if the amplifier is not saturated, then the pump is undepleted and the gain coefficient is constant. Moreover, in such a case, the fiber propagation loss may be neglected. In the case of distributed amplification, the gain assumes a spatial dependence, $g(z)$, and the Non Linear Schrodinger (NLS) equation needs to be solved along the fiber's axis. A high FoM FOPA operates in the regime of deep saturation. Additionally, we limit the pump to a moderate power level, which mandates the use of a long silica fiber. Hence, a high FoM FOPA is necessarily a distributed amplifier.

Recent studies have shown, experimentally and numerically, the degradation of FOPA performance due to longitudinal variation in the fiber's core geometry. In fact, this variation occurs at nanometer scale which is on the order of the molecular

constituent of the fiber – that is at the limit of fabrication control. The ability to carefully characterize in a non-destructive manner the minute variations in the local structure of the fiber is currently unique. This work studied and demonstrated the importance of fiber variations to the understanding of high FoM FOPA. For example: (1) Locally dissimilar fibers with identical global properties show drastically different parametric amplification behavior. (2) A high FoM FOPA has a non-reciprocal transfer function. (3) Locally varying fiber can reach performance levels which are not attainable by uniform fibers. All of which require modeling high FoM FOPA using locally varying fiber.

The vast majority of FOPA studies neglects the local dispersion of fibers and assumes only global properties, thus effectively describing them as a perfectly uniform entity. Indeed, the uniform fiber model is an excellent approximation for many fiber-optics studies. However, in the case of high FoM FOPA, any study which neglects the fiber's local properties will be very limited. Unfortunately, this approximation eliminates critical features of high FoM FOPAs and fails to represent physical limitations one meets when approaching to build such device. For example, a high FoM FOPA that is longitudinally inhomogeneous (spatially non-uniform) can have superior performance compared to when modeled using a perfectly uniform fiber.

1.2.2. Rapidly Varying Low Power Switching

The quest for an optical transistor has been an ongoing, long pursuit. It deals with the ability to directly control a strong (many photon) beam using a weak (few photons) beam. To implement such a device, the common approach is to use either

cavity resonances to enhance the optical power levels in the cavity; or molecular resonances to enhance the nonlinear susceptibility coefficient; or both. Although this approach has proved to be efficient in achieving light manipulation at the few photon level, it is inherently slow and is orders of magnitude below optical communication transmission rates. Cavity resonances are limited by spectral inhibition while molecular resonances are limited by the material response time (T_1, T_2). Additionally, for the latter, the strong beam is usually limited in power to a weak, micro-Watt, level.

Conversely, this work takes a different approach which removes the use of resonances; as it relies on long interaction length in transparent silica fibers. A long silica fiber can be used to create a FOPA with a high FoM. Such a device will not only be sensitive to weak inputs, but can also have a wide bandwidth. However, such a device supposedly has two drawbacks which require investigation. (1) The fiber local structure will need to be addressed as previously described. (2) This wideband device operates as a saturated amplifier with a weak input. Consequently wideband noise will be seeded into the amplifier. The wideband noise is expected to compete with a rapidly varying weak input signal, consequently limiting the sensitivity of the device. For this reason fast devices are inherently noisy, and sensitive devices are inherently slow.

This work asks for to create a fast device and to keep it sensitive, which intuitively is contradictory in nature.

1.2.3. Optical non-Reciprocity

As the vast majority of optical systems are reciprocal in nature, the idea of having an optical diode is intriguing. Certain areas in science and engineering make use of the Faraday's effect by placing a magnetic media in a magnetic field to construct optical isolators and circulators. Such devices are normally used to stabilize and protect communication systems and lasers, which can be disturbed by external inputs. Other applications which use optical isolators are typically affected by scattering effects, back reflections or bi-directional light propagation, for example as in optical systems which rely on SBS [16].

In recent years there has been a renewed interest in optical non-reciprocity: effect and devices. Driven by advancement in nanotechnology fabrication techniques, emerging platforms, such as PIC and SPP, are pursuing miniaturization of optical systems, including that of isolator. The new methods seek more than simply scaling down existing Faraday's devices, but instead focus on creating new technologies.

Fundamentally, non-reciprocal devices rely on (breaking) Lorentz reciprocity theory and Parity-Time symmetry. Various reports [17,18,19,20,21,22,23,24,25], theoretical and experimental, were published on this topic, which in fact sparked a debate in the community regarding basic definitions [26].

This dissertation demonstrates for the first time, a silica-based non-reciprocal device. The non-reciprocal behavior relies on the existence of local structure in glass fiber. Specifically, it is shown here that it is the random core scaling which dominates the effect. In conjunction, this work extends FOPA reciprocity theory by operating the

FOPA in its nonlinear regime. The physical limits of FOPA non- reciprocity outlined here are yet to be found and may be applied in equivalent platforms such as chip-scale parametric waveguides. It is an open question as to whether FOPA non- reciprocity can be explained in term of PT symmetry or Lorentz Theorem.

1.3. Literature Review

1.3.1. Saturated Parametric Amplification

This section provides a current image on the state of the field with respect to this dissertation. The topic of fiber-optic parametric amplification is considered a well-established research field. Surprisingly, little research has been done so far on deeply saturated *parametric* amplifiers. Indeed, most of the published work in the field was performed in FOPA's linear amplification regime. Whereas research which was done in the saturated regime was only weakly saturated and studied in the context of optical regeneration and impairment mitigation.[2] Equally important, previous discussions on saturation did not include the role of local dispersion.

The reason most of the focus has been on the linear amplification regime is practicality. The majority of amplifiers operate in the linear amplification regime where the noise figure is lower; and in general is theoretically simpler. With respect to OPAs, the linear regime adheres to a relatively simple theory, whereas in the nonlinear

[2] Readers who are familiar with EDFA literature would be able to make an analogy between the term "self-saturation" in the context of EDFA and "deep-saturation" in the context of FOPA. Self saturation is a regime in which power of ASE is comparable to that of the pump.

regime the amplification involves many simultaneous processes and may be considered as inefficient. From a standpoint of optical communication, cross talk effects (interaction between various input signals) are enhanced and signal amplification is less efficient as it gives raise to generation of spurious optical tones.

Other types of experiments which seemingly studied saturated parametric amplification had made use of bulk crystals or short wave guide. These were employed in a cavity configuration to overcome losses, weak focusing, and short interaction length – which resulted in poor efficiencies. Similar experiments which did investigate a cavity free apparatus, used high intensity beams (i.e. pump and signal) to drive the interaction. Seemingly, such an experiment could be considered as a saturated amplifier since both beams are comparable in power, $P_S \approx P_P$. However, these amplifiers were usually inefficient and did not cause the pump power to deplete; thus lacking an important component of saturated parametric amplification. In fact, this dissertation explored saturated parametric amplification specifically in the limit of weak input signal, $P_S << P_P$.

Nevertheless, several relevant studies to this field were made. In the early nineties, Cappellini and Trillo found an exact solution to $\chi^{(3)}$ three CW wave mixing. The instructive solution indicated the possibility of strongly depleting the pump wave using an extremely weak signal [27]. The conditions to such an effect were detailed while highlighting the fact this phenomenon is bandwidth limited. However, this article did not include three major factors: vacuum noise, higher order idlers, and local dispersion. All of which play a role in physical saturated parametric systems. Later, Kylemark et al. published a semi-analytical saturation theory of FOPA [28]. It

provided a successful description of MI wavelength-dependent gain under weak saturation conditions. The article mainly focused on signal/idler gain variation. The validity of this model was studied for gain above 20 dB but was limited to a region where the system's gain could not affected by noise amplification. Then, saturation is caused by signal and idler amplification. At signal input power levels above the small signal gain approximation, the model is less suitable due to the increasing role of higher order idlers which were not directly included in the model. In fact, as described in the following chapter, the region of strong saturation by weak input signal is vastly different since saturation is caused by amplification of noise, signal, and idlers; and currently doesn't not have a known analytic solution. The first demonstration of FOPAs' viability, specifically of silica fibers, as an efficient mediator for fast photon-photon interaction was made by Andrekson et al [29]. The majority of all optical experiments use resonances, for example by form of cavity structures, molecular transitions or both, to enhance the nonlinear interaction; an enhancement which is needed in order to operate at low power levels. With this in mind, these resonances also limit the operational speed by restricting the spectrum. Conversely, silica fibers are able to break the tradeoff between efficiency and speed, by providing high γL (excess of $100\,W^{-1}$) while offering femtosecond scale response time. Similar experiments which did not employ resonances, used unpractical power levels to drive the process, thus not only making the device unappealing but also forbidding its continuous operation due to the lack of ability to continuously provide extreme power levels. Thus far, the role of fibers' local dispersion in this system was ignored; this

critical component to the study of deeply saturated FOPAs and their limits is studied here for the first time.

1.3.2. Wave Guiding Platforms for Parametric Amplification: $\chi^{(2)}$ and $\chi^{(3)}$

Even though Kerr nonlinearity exists in a variety of materials, so far, the only platform in which a deeply saturated parametric amplifier was demonstrated, specifically using Watt scale CW light, was silica fibers. This is mainly the result of silica fiber fitting properties as an optical medium. Table 1 lists the properties of state of the art optical waveguide possessing of Kerr nonlinearity of which silica fibers are among the weakest. Nevertheless the interaction length in the medium is equally important and could be effectively limited by both linear and nonlinear losses. Additionally, the efficiency of the nonlinear process depends on the dispersion properties of the waveguide which are derived by the materials as well by the geometry and the quality of fabrication. Evidently, given a limited power budget, silica fiber unparalleled loss compensates for its low nonlinearity well above and beyond the alternative platforms. Chalcogenide platform seems to have a great potential but currently their fibers are limited by high dispersion and TPA. Similarly, photonic crystal chalcogenide waveguides are also limited by dispersion and TPA, and gain has yet been demonstrated. On the other hand silica fibers dispersion tailoring in the telecom band is by far more advanced, routinely demonstrating wideband amplification (covering C+L bands) and high gain. The performance of PCF silica fibers is currently limited in the telecom due to complex fabrication requirements [30].

Table 1: Characteristics of $\chi^{(3)}$ Optical Waveguides

Material	γ ($W^{-1}km^{-1}$)	α (dB/m)	γ/α (W^{-1})	Dispersion (ps/nm/km)	TPA† (m/W)	Ref.
Silica						
Fiber	18	0.0013	60.13	0		[31]
	20	0.0005	173.72	0		[32]
	25	0.0010	108.57	0		[33]
	25	0.0012	90.48	0	N/A	[34]
	10	0.0005	86.86	0		[35]
	30	0.0013	100.22	0		[36]
WG	5	0.0800	0.27	-		[37,38]
PCF	70	0.1900	1.60	0		[39]
Bi_2O_3						
Fiber	1,100	0.8000	5.97	-260		[40]
	1,360	1.9000	3.11	-260	N/A	[41]
	1,360	0.8000	7.38	-260		[42]
PCF	1,100	3.4000	1.41	+40		[43]
TeO_2 HF	675	0.4000	7.33	-25	6.2e-12	[44]
$PbSiO_3$ HF	1,860	3.0000	2.69	+210	7.2e-15	[45]
Chalcogenide						
As_2Se_3						
Fiber	1,200	1.0000	5.21	-504	2.5e-12	[46]
Fiber Taper	93,400	1.0000	405.63	+282	2.5e-12	[47]
As_2S_3						
Fiber	160	0.8800	0.79	+410	6.2e-15	[48]
Rib WG	1,700	5.0000	1.48	-342	6.2e-15	[49]
	9,900	60.0000	0.72	+29	6.2e-15	[50]
Ag-As_2Se_3						
PhC WG*	26,000,000	1,000.0000	112.92	-	4.1e-12	[51]
	63,000.000	21,000.0000	13.03	+40	-	[52]
GeAsSe nanowire	136,000	250.0000	2.36	+70	1.0e-13	[53]
AlGaAs WG	521,000	650.0000	3.48	-	Neg.	[54]
Silicon**						
WG	(146,308)	125.0000	5.08	+500	-	[55]
	(175,570)	150.0000	5.08	+800	(1.3e-11)‡	[56]
	(52,671)	30.0000	7.62	-	-	[57]
	150,000	400.0000	1.63	-	5.0e-12	[58]
	52,671	27.4000	8.35	-	-	[59]
Hydex™ Glass	233	4.0000	0.25	-	Neg.	[60]

Note: Values in prentices were calculated based on the reported information in the references.
†TPA cutoff wavelength: SiO_2: 0.3 μm [61]; Bi_2O_3: 1.2 μm [62]; TeO_2: 0.7 μm [61]; $PbSiO_3$: 1 μm [63,64]
*Gain has not been demonstrated
**Silicon TPA cutoff wavelength is 2.2μm was measured to be 1.0e-11 m/W [65].
‡Includes TPA and FCA

When inspecting the performance of state of the art quasi phase matched $\chi^{(2)}$ waveguides, shown in Table 2, to check for existence of suitable alternatives to saturated parametric amplification, it is evident none are currently available.

Table 2: Characteristics of $\chi^{(2)}$ Quasi Phase Matched Optical Waveguides

Material	$\sqrt{\eta}$ (1/√(W).km)	α (dB/m)	$\sqrt{\eta}/\alpha$ (1/√W)	P_P (W)	CE (dB)	Type	Ref.
PPLN WG							
ZnO:LiNbO3	(93,808)	30	13.58	0.60	+8.00	cSGH/DFG	[66]
RPE	87,178	-	-	0.12	-1.19	SFG	[67,68]
	(122,474)	60	8.86	0.12	+10.00	DFG	[69,70]
	(122,474)	60	8.86	0.20	+10.00	cSGH/DFG	[69]
GaP PhC WG	(41,595)	-	-	2mW	-63.01	SHG	[71]
PePSi							
WG	(27)	200	5.8e-4	0.70	-	SHG	[72]
GaAs/AlGaAs							
QPM WG	187,083	565	1.44	209.00	-41.76	SHG (Type II)	[73]
	354,965	391	3.94	-	-	SHG (Type I)	[73]
GaP/AlGaP							
QPM WG	40,000	3,000	0.06	0.08	-47.10	DFG (Type I)	[74]
KTP							
WG	30,166	800	0.16	0.13	-19.83	SHG (Type II)	[75]
BULK	5,916	-	-	1.00	-24.81	SHG (Type II)	[75]
PPKTP WG	34,799	120	1.26	1.60	-7.13	SHG (Type II)	[76]
PPLT							
WG	-	200	-	0.10	-51.76	cSHG/DFG	[77]
	(8,868)	200	0.19	0.02	-32.00	SHG	[77]

Notes: Values in prentices were calculated based on the reported information in the references. The equivalent FoM for $\chi^{(2)}$ waveguides is $\sqrt{(\eta P)}L$.

These waveguides possess several key problems. Their temperature requires constant regulation. In fact, an optical beam, if sufficiently strong will modify the geometrical structure of the waveguide [76]. This is mainly due to heating effects cause by waveguide absorption and results in resonance shift. In fact, their high insertion loss forbids launching the sufficient amount of power levels needed for gain, which is often not observed in these platforms. Recently, progress has been made regarding their limited phase matched bandwidth. This was done by utilizing a good conversion scheme, which cannot produce gain, particularly using a-periodic poling [78] – this is conceptually connected to the challenge of local dispersion. Nevertheless, until these platforms could demonstrate strong gain, they will not be suitable for the study of deeply saturated parametric amplification.

1.3.3. Optical Switching

The former discussion resulted in the recognition that silica fiber is the most suitable platform to study deeply saturated amplification. Moreover, given a moderate pump power levels, currently, this is the only platform which could produce the required high FoM. This dissertation studies the limits of deeply saturated parametric amplification, including in the context of switching. This means to control the pump state using a rapidly varying signal input. To provide a perspective on the quality of results shown in this dissertation, a survey on the state of the art of optical switching is shown in Table 3 and Figure 2. The comparison is based on five categorize: energy consumption per bit, switching (control) energy per bit, switching speed, extinction ratio, and demonstrated repetition rate. The survey consisted of a variety of platforms: MQW_ISBT – based on fast intersubband transition [79]; PhC – a PhC WG with a defect (cavity), using FCA to shift the cavity's resonance [80]; PhC-MZM – the arms are coated with quantum dots which induce a nonlinear phase [81]; SlotWG – A slot WG filled with Organic Polymer for FWM [82]; μ-Ring – optically modulating the ring transfer function using a plasma-dispersion effect [83]; μ-Disk – optically toggling between the two lasing mode, clockwise and counter clockwise, of an whispering gallery resonator [84]; EAM – GeSi electro-absorption modulator [85]; Cold Rb/PCF – Cold Rubidium gas trapped in PCF [86]; Hot Rb/PCF – Rubidium gas trapped in PCF [87]; BBO – Degenerate down conversion in a $\chi^{(2)}$ bulk crystal [88]; μ-Cavity – Kerr effect is used to shift the resonance [89]; Cavity QED – a strong

Table 3: Optical Switching Survey

Total Energy Per Bit	**Switching Energy Per Bit**	**Switching Speed**	**Extinction Ratio**	**Repetition Rate**
PhC_{3dB} (0.42 fJ)	BBO (0.25 aJ)	BBO (0.2 ps)	μ-Disk (11 dB)	μ-Cavity (3.33 THz)
PhC_{10dB} (0.66 fJ)	HNLF*$_{3dB}$ (2.7 aJ)	μ-Cavity (0.3 ps)	MQW ISBT (10 dB)	HNLF* (160 GHz)
Cold Rb/PCF (1 fJ)	Hot Rb/$PCF_{1.2dB}$ (5 aJ)	MQW_ISBT (0.6 ps)	HNLF* (10 dB)	HNLF* (160 GHz)
EAM_{3dB} (13 fJ)	HNLF*$_{10dB}$ (19 aJ)	HNLF* (2 ps)	PhC (10 dB)	Slot WG (42.7 GHz)
Cavity QED (45 fJ)	Hot Rb/PCF_{3dB} (50 aJ)	HNLF* (2 ps)	μ-Ring (9 dB)	μ-Disk (10 GHz)
EAM_{8dB} (50 fJ)	Cold Rb/PCF (0.18 fJ)	SlotWG (3 ps)	EAM (8 dB)	EAM (1 GHz)
PhC-MZM (100 fJ)	PhC_{3dB} (0.42 fJ)	PhC –MZM (15ps)	Slot WG (7.7dB)	EAM (1 GHz)
SlotWG (180 fJ)	PhC_{10dB} (0.66 fJ)	μ-Ring (25 pJ)	BBO (7 dB)	Hot Rb/ PCF (200 MHz)
μ-Disk (380 fJ)	μ-Disk (1.8 fJ)	PhC (35 ps)	PhC MZM (5.4 dB)	Hot Rb/ PCF (200 MHz)
μ-Ring (1 pJ)	EAM_{3dB} (13 fJ)	PhC (35 ps)	HNLF* (3 dB)	μ-Ring (80 MHz)
MQW_ISBT (6.9 pJ)	Cavity QED (14.9 fJ)	Cavity QED (55 ps)	PhC (3 dB)	PhC MZM (80 MHz)
HNLF*$_{3dB}$ (8.25 pJ)	EAM_{8dB} (50 fJ)	μ-Disk (60 ps)	EAM (3 dB)	Cavity QED (76.3 MHz)
HNLF*$_{10dB}$ (8.25 pJ)	PhC –MZM (100 fJ)	EAM (1 ns)	Hot Rb/PCF (3 dB)	MQW ISBT (76 MHz)
Hot Rb/$PCF_{1.2dB}$ (60 pJ)	SlotWG (144 fJ)	EAM (1 ns)	Cold Rb/PCF (3 dB)	PhC (10 MHz)
μ-Cavity (127 pJ)	μ-Ring (1 pJ)	Hot Rb/PCF (5.3 ns)	Hot Rb / PCF (1.2 dB)	PhC (10 MHz)
Hot Rb/PCF_{3dB} (60 pJ)	MQW_ISBT (6.9 pJ)	Hot Rb/PCF (5.3 ns)	μ-Cavity (0.97 dB)	Cold Rb/PCF (500 kHz)
BBO (39 μJ)	μ-Cavity (127 pJ)	Cold Rb/PCF (1 μs)	Cavity QED (0.36 dB)	BBO (1 kHz)

Note: Subscripts were added to prevent ambiguity as they indicate the extinction ratio associated with the result.
*Based on this dissertation (High FoM FOPA)

coupled system of quantum dot and a cavity (Jaynes–Cummings) [90]. While some platforms have excelled in one or two categorize, clearly, high FoM FOPA (HNLF*) over-all performed extremely well, except in its total energy consumption. When judging these results in terms of speed *vs.* switching power, as summarized in Figure 2, given moderate power levels, HNLFs are orders of magnitude ahead of alternative

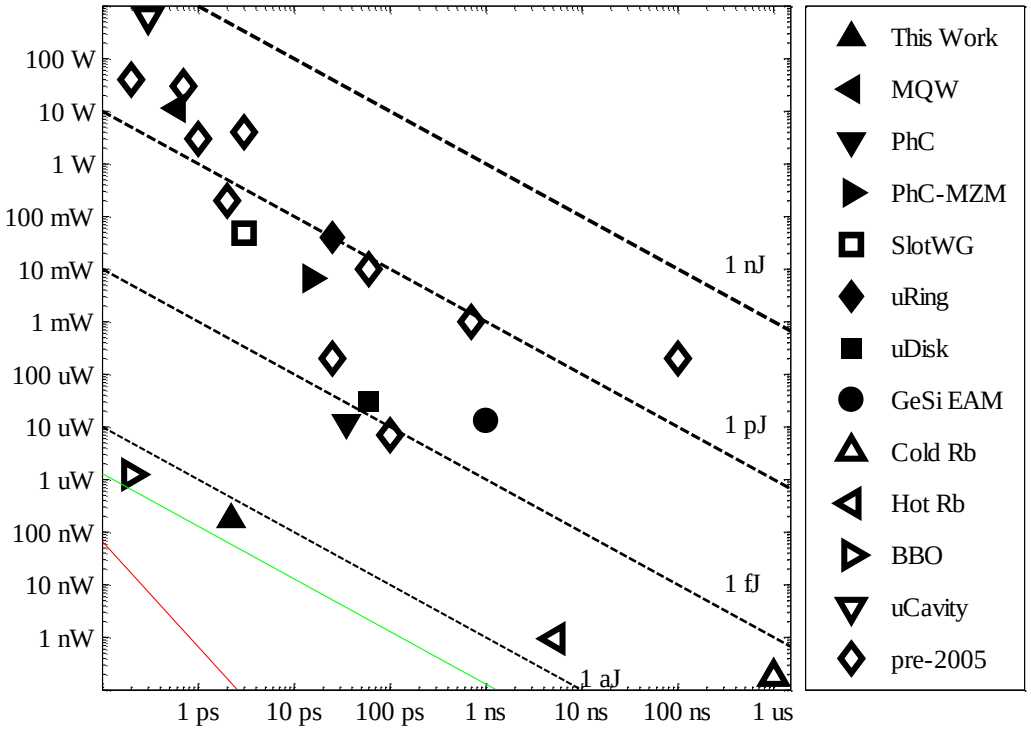

Figure 2: Optical Switching Survey: Control Power *vs.* Switching Time | This figure shows a graphical representation of Table 3, where the x and y axes are the switching time and the amount power needed to control the switch. The green line represents the energy of a single photon in the telecom's C band, while the red trace is associated with the uncertainty principal.

technologies. Results which were reported before 2005 were taken from [91]. Bear in mind these reports are not equivalent, since each one is measured at a different ER. For example, in the μDisk experiment, 11 dB of ER was reported while only 1 dB was observed in the μCavity. Future reduction of high FoM FOPA total power consumption will be the result of harnessing local dispersion, albeit at the expense of latency (fiber length).

1.4. Outline of The Dissertation

The following four chapters are the core of this dissertation. Chapter 2 discusses the preliminaries of deeply saturated parametric amplification. It includes introductory material and continues to properties of HNLF: their physical description and relation to parametric amplification.

Chapter 3 describes a numerical analysis of deeply saturated parametric amplification in physical fibers. It explains consideration in physical fiber modeling and the required modification to the NLS model which are needed to incorporate between them. This chapter studies the performance limit of this system, proposes a characterization method, and provides predictions, which are experimentally confirmed in the succeeding chapters. Additionally, the results of this chapter yield engineering rules regarding design considerations one faces in realizing saturated FOPAs.

In Chapter 4, a conception as to whether indeed longitudinally uniform fibers are the most desirable for deeply saturated FOPAs is challenged. This study is performed using numerical methods and describes a search for a “golden” dispersion profile. This chapter contains a description of the method and the computational challenge associated with this problem. The results of this chapter indicate on a wealth of opportunities with regards to enhancing the performance of FOPAs via local dispersion engineering. The computational cost associated with this problem is computationally expensive and was enabled by the recent introduction of multi-cores GPU to this field.

Chapter 5 combines both numerical and experimental content. For the first time, the non-reciprocal nature of deeply saturated FOPAs is experimentally demonstrated and its origin is validated. The chapter begins by showing a simple manifestation of the non-reciprocal nature of this system. Subsequently, this result is leveraged in a novel simulation method to characterize the system which proves it is governed by its local properties, specifically by geometrical scaling effects, and confirms the predictions made in the preceding chapters. Next, a static characterization technique is presented and demonstrated; and the simulation technique is shown to be accurately describes the FOPA's non-reciprocal behavior. Additionally, the results of this characterization are analyzed, and predict record dynamical capabilities to the saturated amplifier. These results prove that local dispersion is a key factor in the behavior of saturated FOPAs.

Finally, Chapter 6 summarizes the dissertation, and discusses future research.

Chapter 2

Preliminaries to Deeply Saturated Parametric Amplification

This chapter contains basic information pertaining to the study of deeply saturated FOPAs, including coverage of essential points in a wide variety of topics, with the aim of introducing this topic to new researchers in the field. This text is written from both experimental and numerical perspective, and is mostly focused on qualitative understanding, with references for more details.

2.1. Introduction

2.1.1. Linear and Nonlinear Optics

Linear and Nonlinear optics refers to the way in which light interacts with matter. In everyday life, we are costumed that every material has color (frequency) dependent optical properties and that these will remain the same regardless of the optical field's amplitude. However, if the optical field's amplitude is sufficiently strong, the material's optical properties will also exhibit dependence on it. The former realm is known as linear optics, while the latter is described as nonlinear optics.

Nonlinear optics originates from the polarization term in Maxwell's equation. This term is associated with the effect of light on matter. Conversely to a conductor, which to a certain extent can be modeled as an electron gas with free charge carriers,

in dielectric materials electrons are bounded to the nucleus. In the example of non-polar molecules, external electric field may polarize the molecule: displace the electron cloud of the molecule from its positive counterpart and induce polarization (a collection of induced dipoles). Under illumination, the collection of oscillating dipoles will in turn radiate and affect the illuminating field. The derivation of this interaction shown in the following part of this section follows [92].

The phenomenon can be described using two of Maxwell's equations:

$$\nabla \times \vec{E}(t) = -\frac{\partial}{\partial t}\vec{B}(t) \tag{1}$$

and

$$\nabla \times \vec{H}(t) = \varepsilon_0 \frac{\partial}{\partial t}\vec{E}(t) + \vec{J}(t). \tag{2}$$

The current density $\vec{J}$ is composed from conduction current $\vec{J}_C$ and displacement (polarization) current $\partial\vec{P}/\partial t$. As nonlinear optics is the result of oscillating dipoles in dielectric materials, conduction currents may be neglected. Consequently, Eqs. (1) and (2) can be used to derive Maxwell's wave equation in the following form:

$$\nabla \times \nabla \times \vec{E}(\omega) = \frac{\omega^2}{c^2}\vec{E}(\omega) + \omega^2 \mu_0 \vec{P}(\omega) \tag{3}$$

The full form of the polarization vector is in fact complicated and is not necessary for the purpose of this section. The polarization vector can be expressed as a series of orders,

$$\vec{P}(t) = \vec{P}^{(0)}(t) + \vec{P}^{(1)}(t) + \vec{P}^{(2)}(t) + \vec{P}^{(3)}(t) + \ldots. \tag{4}$$

The 0^{th} order polarization term can be neglect and is associated with polar molecules or crystals' static polarization. The 1^{st} order is associated with the material's linear response; the 2^{nd} order has quadratic field dependence and it can be neglected in

materials with inversion symmetry such as silica fibers. More information on silica fibers is given in Section 2.2. The 3rd order polarization has a cubic field dependence and is considered the dominant (nonlinear optical) term when the 2nd order can be neglected. The 4th order term and higher are not relevant to this dissertation and are beyond the scope of this discussion. The 1st order polarization can be written in the following form,

$$\vec{P}^{(1)}(t) = \varepsilon_0 \int_{-\infty}^{\infty} \vec{\vec{\chi}}^{(1)}(\omega)\vec{E}(\omega)e^{-i\omega t}d\omega \tag{5}$$

where $\vec{\vec{\chi}}^{(1)}$ is the linear susceptibility tensor. In the case of linear optics, Eq. (3) may assume the known form,

$$\nabla\times\nabla\times\vec{E}(\omega) = \frac{\omega^2}{c^2}\left(1+\vec{\vec{\chi}}^{(1)}(\omega)\right)\vec{E}(\omega) = \frac{\omega^2}{c^2}\vec{\vec{\varepsilon}}(\omega)\vec{E}(\omega) \tag{6}$$

and the dielectric tensor will be defined as, $\vec{\vec{\varepsilon}}(\omega) = 1+\vec{\vec{\chi}}^{(1)}(\omega)$.

The 2nd order polarization is expressed using the second order susceptibility tensor. This is shown in Eq. (7) which is written using suffix notation for the sake of completeness.

$$P_{\mu}^{(2)}(t) = \varepsilon_0 \int_{-\infty}^{\infty} d\omega_1 \int_{-\infty}^{\infty} d\omega_2 \chi_{\mu\alpha\beta}^{(2)}(\omega_1,\omega_2)E_{\alpha}(\omega_1)E_{\beta}(\omega_2)e^{-i(\omega_1+\omega_2)t} \tag{7}$$

Generally, the susceptibility tensor contains permutation symmetry, which gives rise to a numerical factor associated with each phenomenon. It is therefore recommended to use existing tables to find the numerical coefficient. For example, if ω_1 and ω_2 are degenerate ($\omega_1 = \omega_2$) the numerical factor is reduced by half compare to the general case ($\omega_1 \neq \omega_2$).

The special property of nonlinear optics is to enable waves at different frequencies to interact with each other and to create waves at new frequencies which were not present before the (nonlinear) interaction. This can be seen by writing Maxwell's wave equation in the nonlinear regime:

$$\nabla \times \nabla \times \vec{E}(\omega) = \frac{\omega^2}{c^2} \vec{\varepsilon}(\omega) \vec{E}(\omega) + \omega^2 \mu_0 \vec{P}^{NL}(\omega) \tag{8}$$

where P^{NL} is usually either $P^{(2)}$ or $P^{(3)}$. In a simple case of second order polarization, assume a monochromatic input field at frequency ω_0, where P^{NL} can be expressed as follows,

$$P^{NL}(t) = \varepsilon_0 \chi^{(2)} [E_0 \cos(\omega_0 t)]^2 = \varepsilon_0 \chi^{(2)} \frac{E_0^2}{2} (\cos(2\omega_0 t) + 1). \tag{9}$$

Although this example can be made in the frequency domain, it would then require dealing with 16 terms. This would unnecessarily complicate the point of this example, and was therefore written in the time domain. Nevertheless, the susceptibility tensor, $\chi^{(n)}$, is defined in the frequency domain, and it is used in jointly with the time-dependent field and polarization vectors, which is seemingly wrong. However, this is allowed under the adiabatic limit in which the field's envelope is assumed to be changing much slower than the dipoles' relaxation time. As seen in Eq. (9), a fundamental wave ω_0 generates both a DC term and a second harmonic ($2\omega_0$) term. In a similar manner quadratic and cubic field dependences give raise to terms with new harmonics in Maxwell's wave equation. The following example is non-degenerate and is again based on a $\chi^{(2)}$ process. Assume the field is a superposition of two monochromatic waves, at wavelengths, λ_1 and λ_2 corresponding to 0.8 μm and 1.5 μm. Repeating the computation in Eq. (9),

$$\begin{aligned} P^{NL} &= \varepsilon_0 \chi^{(2)} \left[E_0 \cos(\omega_1 t) + E_0 \cos(\omega_2 t) \right]^2 \\ &= \varepsilon_0 \chi^{(2)} E_0^2 \left(\cos^2(\omega_1 t) + 2\cos(\omega_1 t)\cos(\omega_2 t) + \cos^2(\omega_2 t) \right) \\ &= \varepsilon_0 \chi^{(2)} E_0^2 \left(\frac{\cos(2\omega_1 t) + \cos(2\omega_2 t)}{2} + \cos\left[(\omega_1 + \omega_2) t \right] + \cos\left[(\omega_1 - \omega_2) t \right] + 1 \right) \end{aligned} \tag{10}$$

, yielded five terms. The first two terms are related to second harmonic generation of wavelengths λ_1 and λ_2 with corresponding wavelengths of 1.6 μm and 3 μm; the third and fourth terms are related to sum and difference frequency generation with corresponding wavelengths of 0.52 μm and 1.72 μm; and the last term is associated with a static electric field generation. Using a $\chi^{(2)}$ process, it seems the two original waves will generate five new tones, however in practice, only one term will be observed.

The reason is that new waves need to be generated in a (constructively) coherent manner, commonly known as the phase matching condition. The structure of the condition generally depends on the specific process, for example, whether it is sum or difference frequency generation. In practical terms, the phase matching condition requires satisfying a certain relation between the refractive index of the participating waves (including the new wave), and is related to the material's linear response, $\chi^{(1)}$. By further examining Maxwell's wave equation, Eq. (8), the mathematical manifestation of the phase matching condition can be revealed. Assume a field consisted of co-polarized, infinite plane waves propagating in the +z direction of a losses, isotropic medium. This assumption coupled with the slowly varying envelope approximation, enables us to simplify the wave equation:

$$\frac{\partial}{\partial z} E(\omega) = i \frac{\omega^2 \mu_0}{2k} P^{NL}(\omega) e^{-ikz} . \tag{11}$$

Generally, Eq. (11) couples between the spectral components of the field through P^{NL}. However, in practice, only few components will need to be taken into consideration. Consequently, a set of coupled mode equation will be generated. The reason for this simplification is the result of limited phase matching, resonant behavior of the susceptibility tensor, a dominant process, or a combination of these. The set of coupled mode equations can be decoupled in case the wave driving the nonlinear process (known as the pump beam) effectively remains constant. Following the previously mentioned simplification, Eq. (11) may take an explicit form. Equation (12) is written for a generic $\chi^{(3)}$ process involving monochromatic waves:

$$\frac{\partial}{\partial z}E(\omega_\sigma) = i\frac{\omega_\sigma^2}{2k_\sigma c^2}K(\omega_1,\omega_2,\omega_3)\chi^{(3)}(\omega_1,\omega_2,\omega_3)E(\omega_1)E(\omega_2)E(\omega_3)e^{i\Delta k\ z}, \qquad (12)$$

where K is the numerical factor which depends on the specific process; $\omega_\sigma = \omega_1 + \omega_2 + \omega_3$, and $\Delta k = k_1 + k_2 + k_3 - k_\sigma$ where $k_i = n(\omega_i)\frac{\omega_i}{c}$. If for example, Eq. (12) were to describe a modulation instability process, where power from $E(\omega_1)$ and $E(\omega_2)$ is transferred to $E(\omega_3)$ and $E(\omega_\sigma)$, it would be written in the following form,

$$\frac{\partial}{\partial z}E(\omega_\sigma) = i\frac{\omega_\sigma^2}{2k_\sigma c^2}K(\omega_1,\omega_2,-\omega_3)\chi^{(3)}(\omega_1,\omega_2,-\omega_3)E(\omega_1)E(\omega_2)E^*(\omega_3)e^{i\Delta k\ z}, \qquad (13)$$

and Δk would be set as $k_1 + k_2 - k_3 - k_\sigma$. Given that all the parameters on the right hand side of the equation are constants (except z), as the waves (ω_1, ω_2, and ω_3) propagate in the nonlinear ($\chi^{(3)}$) medium, the amplitude of $E(\omega_\sigma)$ will change depending on the value of $\Delta k\, L$, where L represents the distance the waves propagate. Integration over the rotating exponential yields the following:

$$\int_0^L \exp(i\Delta k\, z)dz = \left\{\alpha = \frac{\Delta k\, L}{2}\right\} = -i\, L\, e^{i\alpha}\, \frac{\sin(\alpha)}{\alpha}\,. \tag{14}$$

This is the manifestation of the phase-matching condition: for any given L, the amplitude of this expression is maximized when $\Delta k = 0$. Figure 3 shows a graphical illustration of Eq. (14), and its dependence on Δk. Generally, satisfying the phase matching condition is not straight forward as it calls for precise matching between the participating frequencies and the available mediums. Evidently, when working with bulk material, the properties of the crystal are given, and the user is left to utilize material's birefringence to achieve a minimal Δk. Additionally, the power efficiency of this process is limited due to tradeoff between the focal length and beam spot size [92]. As the beam size becomes smaller so will the focal length be shorten, and vice versa. On the other hand, using a bigger spot size will require more power to drive the

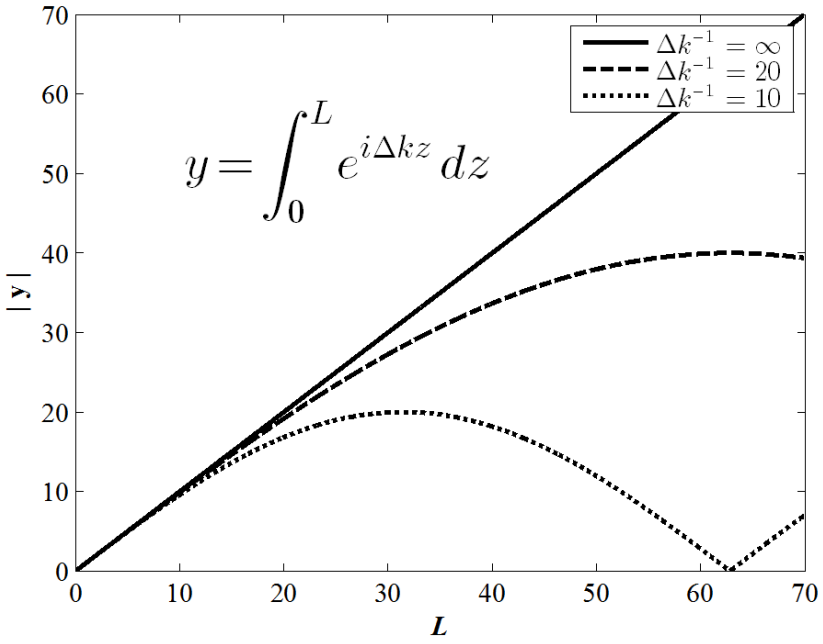

Figure 3: Phase Matching Concept in Optical Frequency Generation | In its most simplified form, optical generation is a periodic process with a characteristic length associated with Δk, where only one half of the period is constructively generating light.

process, as it is in fact driven be the beam intensity. The benefit of using an optical waveguide is in its ability to resolve these issues. Waveguides' dispersion can be tailored to achieve phase matching, confine the light to small spot size, and maintain significantly longer interaction length. Additionally, waveguides have technological significance in many other applications.

Further information on NLO in HNLFs is provided in Section 2.2.2.

2.1.2. Waveguide Physics and Fiber-Optics

Dielectric Optical waveguides are very-high aspect ratio structures capable of confining, guiding, and bending light. Additionally, they can be designed to perform variety of operations on light fields, including amplification, modulation, detection, filtering, multiplexing, and more. Their cross sectional structure is made of core-cladding geometry, where the core is surrounded by a relatively lower refractive index cladding material.[3] Analytical models of waveguides are based on core geometries such as slab, rectangular, or circular, but in practice they may have a different shape in accordance with the selected architecture and fabrication process. Nevertheless, these models provide much insight on the physics of waveguides.[4]

Waveguides are based on the principle of total internal reflection: if a ray incident an interface between two spaces, coming from one refractive index (RI) space toward a lower one, at a shallow angle according to Snell's law, the beam will be

[3] Waveguides which are based on the photonic band gap principal, e.g. holey fiber, are an exception.
[4] More information may be found in [4], [136].

completely reflected. This explains the reason a waveguide's core RI needs to be higher than its cladding in order to guide light. Using wave-optics, given a complete description (geometry and materials) of a waveguide's structure, its mode profile (field distribution) and associated effective index, n_{eff}, can be evaluated. The guiding mode will have an effective wave-vector, β, known as the propagation constant, where $\beta = \omega n_{\text{eff}}(\omega) / c$. In fact, a waveguide can support a number of guiding modes each having its own propagation constant. The maximum number of propagating modes for a given wavelength can be pre-determined by properly engineering the structure of the waveguide. This is done by applying boundary conditions matching the waveguide's structure on Maxwell's wave equation. Then, an eigenvalue equation can be solved where each solution provides a mode profile and its associated effective index. The number of propagating modes supported by the waveguide will be the amount of solutions with effective index greater than the index of the cladding.

The term effective index is used since the value of the wave-vector is dictated by the structure of the waveguide. In fact, the propagating mode's effective index will have an upper and lower limit corresponding to the RI of the core and cladding, respectively. Generally, modes with higher effective index will be better confined and more resilient to bending. Using a unit less parameter known as *normalized frequency*, *V*, it is possible to evaluate the cutoff wavelength of the WG. For example, in the case of a fiber WG the expression for *V* will be

$$V = \frac{2\pi}{\lambda_0} a \sqrt{n_{Core}^2 - n_{Clad}^2}\,, \tag{15}$$

where λ_0, a, n_{Core}, and n_{Clad} denotes the free space wavelength, core radius, core RI, and cladding RI, respectively. For such a structure, Eq. (15) must satisfy $V < 2.4$ to ensure the fiber supports only a single mode. Regarding the ratio between the wavelength and the radius of the core, since the fundamental mode doesn't have a cutoff frequency, it may seem that V can be made arbitrarily small. In practice, if the core size (diameter) is smaller than the wavelength, effective medium theory will be applied and the mode will quickly lose its confinement, making it impractically susceptible to any perturbation. On the other hand, high mode confinement increases the sensitivity of the waveguide's specification to structural imperfections; this point is elaborated in the following section. To provide a perspective, a standard single mode fiber (SMF) typically has the following structure: a core and a cladding size of 8 μm and 125 μm, respectively. The fiber is made of amorphous silica glass (SiO_2) and its core is doped with GeO_2 to increase the RI. The core-cladding RI difference is $(n_{Core} - n_{Clad})/n_{Core} \sim 0.3\%$; where $n_{Core} \cong n_{Clad}$ and is around 1.47 at 1.55 μm wavelength, resulting in $V = 2$ and a mode size of 10 μm – making the mode well isolated from the environment. In more advanced fibers, the doping profile is carefully tailored to achieve specific dispersion properties, as reflected by n_{eff} frequency dependence. Over time novel doping profiles were introduced resulting in new types of fibers including dispersion shifted fiber (DSF), dispersion flattened fiber (DFF), and dispersion compensating fiber (DCF).

The creation of these fibers is part of the evolution of fiber-optics communication systems and the result of an effort to reduce fiber related limitations which are fiber propagation loss, dispersion, and nonlinearity. Generally, the challenge

in optical communication is to minimize and balance these three properties to maximize the fiber reach-capacity product. The propagation loss α describes the mode power-loss in the fiber as a function distance; it is measured and expressed in units of dB/km. This quantity indicates on the distance a signal propagates before it is detected or amplified. With regards to NLO, it tells us the effective interaction length between a pump and a signal, after which their power will be too weak to further drive the interaction. The dispersion of a fiber, expressed using the frequency dependent mode's wave-vector, $\beta(\omega)$, is usually related to modulated signal (data) transmission. As a parameter, it is customary to express the wave-vector as will be shown later in this section as a series of Taylor expansion, and describe its higher order terms as a function of experimental data. Dispersion in fibers can temporally broaden pulses, and more generally distort signals. In the context of NLO, a phase matching and a bandwidth of a nonlinear process are dictated by the dispersion of the fiber. The nonlinearity of the fiber γ is expressed and measured in units of $\mathrm{W^{-1}km^{-1}}$. In the context of optical communication, the fiber nonlinearity couples between signals and distort them. In fact, nonlinearity in fibers, currently pose a limit on fiber capacity. The source of nonlinearity in silica fiber is $\chi^{(3)}$ and it is described using nonlinear refractive coefficient n_2 in units of $\mathrm{m^2\,W^{-1}}$. Details on the relation between $\chi^{(3)}$, n_2, and γ, are available in [13], [92]. $\chi^{(3)}$ [$\mathrm{m^2\,V^{-2}}$] is quantity associated with the electric field, n_2 [$\mathrm{m^2\,W^{-1}}$] is associated with to the intensity, and γ – which incorporate n_2 and the fiber's mode-area – is associated with the power launched into the fiber.

Modeling of light propagation in fibers is done using the Non Linear Schrodinger (NLS) model which incorporate $\alpha, \beta,$ and γ. This universal approach successfully enables comparison between waveguides, and is a straight forward method to simulating them. For the purpose of this dissertation it will be sufficient to focus on the scalar version of NLS equation (NLSE) in its following form,

$$\frac{\partial A}{\partial z} + i\frac{\beta_2}{2!}\frac{\partial^2 A}{\partial T^2} - \frac{\beta_3}{3!}\frac{\partial^3 A}{\partial T^3} - i\frac{\beta_4}{4!}\frac{\partial^4 A}{\partial T^4} + \frac{\beta_5}{5!}\frac{\partial^5 A}{\partial T^5} = i\gamma|A|^2 A - \frac{\alpha}{2}A. \qquad (16)$$

Eq. (16) describes light propagation in a fiber along its axis in the *z* direction, in a moving frame-of-reference at a speed of the signal's group velocity $v_g = 1/\beta_1$, where $T = t - \beta_1 z$. *A* represents a slowly varying envelop of an optical carrier ω_0 travelling with a propagation constant β_0 is related to the electric field *E* which can be written as,

$$E = \frac{1}{2}\{F(x,y)A(z,t)\exp[i(\beta_0 z - \omega_0 t)] + c.c.\}, \qquad (17)$$

where $F(x,y)$ represents the (fundamental) mode's field distribution. The state of polarization of the field is ignored because this is a scalar model; therefore we assume that all-spectral components of the field propagating in the fiber are linear and remain co-polarized for the duration of flight inside the fiber. The dispersion in the fiber is represented by $\beta(\omega)$,

$$\beta(\omega) = \beta_0 + \beta_1(\omega - \omega_0) + \frac{\beta_2}{2!}(\omega - \omega_0)^2 + \frac{\beta_3}{3!}(\omega - \omega_0)^3 + \frac{\beta_4}{4!}(\omega - \omega_0)^4 + \ldots. \qquad (18)$$

where the NSLE contain the coefficients of β 's Taylor expansion around the carrier frequency. In the context of numerical simulations, the choice of ω_0 is a matter of convenience and is therefore known as a reference frequency. Since β_1 is related to the group velocity of the fiber at the reference frequency, β_2 is therefore known as the

group velocity dispersion (GVD) parameter, as it represents the group velocity frequency dependence. In the special case where the reference frequency coincide with the ZDW which is denoted by λ_0,

$$\beta_2 = -\frac{\lambda_0^2}{2\pi c} D(\lambda_0) = 0 . \tag{19}$$

If β_2 was set to zero, a propagating pulse would seemingly not experience any temporal broadening, however, in this case the dispersion of the waveguide will be dominated by β_3 which is also associated with the dispersion slope *S*,

$$\beta_3 = \frac{\lambda^3}{(2\pi c)^2}\left[2D(\lambda) + \lambda S(\lambda)\right], \tag{20}$$

and when it is derived at the ZDW it reduces to

$$\beta_3 = \frac{\lambda_0^4}{(2\pi c)^2} S(\lambda_0) . \tag{21}$$

While β is a good parameter for numerical and analytical purposes, it is easier to measure and understand the dispersion of a fiber *D* in terms of ps/nm/km. One method to acquire *D* is by launching a pulse and measure the time it takes the pulse to pass through the fiber (waveguide), and repeating this at different wavelengths, $\tau(\lambda)$. *D* can be evaluated by taking τ's wavelength derivative and normalizing it to the length of the fiber *L*,

$$D(\lambda) = \frac{1}{L}\frac{d\tau}{d\lambda} . \tag{22}$$

Using the general relation between β_2 and *D*,

$$D(\lambda)d\lambda = \beta_2(\omega)d\omega , \tag{23}$$

and given that

$$\beta_i = \left(\frac{d^i}{d\omega^i} \beta \right)_{\omega=\omega_0}, \tag{24}$$

any β coefficient can be expressed in terms of D and its derivatives as shown in Eqs. (19) and (20).

The use of scalar version of NLSE means polarization related effects are neglected. The most common polarization effect in waveguides is the dispersion dependence on light state of polarization, known as polarization mode dispersion (PMD). The effect of PMD is the result of lack of rotational symmetry of the waveguide cross section. For example in fibers, any deviation of the waveguide's cross sectional geometry from a circle can be approximated as an ellipse having a magnitude and orientation, consequently inducing fiber birefringence. Further complication arises from variations in the orientation of the ellipse along the fiber, which leads to coupling between polarization modes and random rotation of the light state of polarization. In the context of this dissertation, the question of whether such an effect can be neglected was experimentally and numerically examined in Chapter 5.

The previous section presented the topic of phase matching in NLO which was described using the instructive example of interaction between monochromatic waves. However, particularly in the case of Saturated FOPA, when many waves and noise are propagating or generated in a waveguide, it would become impractical to track each one of the process. This will result in unreasonably large number of coupled mode equations and be both numerically and analytically difficult to analyze. The common approach is to treat the entire field as a single entity which experiences self phase modulation in the time domain,

$$\frac{\partial A(z,t)}{\partial z} = i\gamma |A|^2 A(z,t), \tag{25}$$

where γ is given by,

$$\gamma = \frac{\omega_0 \, n_2(\omega_0)}{c \, A_{eff}(\omega_0)}. \tag{26}$$

The terms n_2 and A_{eff} represent the nonlinear refractive coefficient and the effective mode area at the reference frequency, ω_0. Further description of γ and its relation to parametric amplification is given in the following sections of this chapter.

2.2. Highly Nonlinear Optical Fibers

2.2.1. General Properties

Highly Nonlinear Fiber (HNLF) is a type of specialty fiber which was introduced in the literature at [93] and have since been gradually maturing to provide high performance [94]. This is a GeO_2 highly doped silica fiber which takes advantage of the high mode-confinement to reduce the mode size. Doing so, as indicated by Eq. (26), produces an increase in the fiber nonlinearity. Thus, along with its low dispersion and low propagation loss, result in light propagation in a fiber with predominant nonlinear parameter γ in comparison to standard single mode fibers [13]. Yet when compared with alternative platforms, HNLF nonlinear parameter is considered to be low (Table 1). This relative deficiency is beyond compensated – primarily by the HNLF's unparalleled transparency in the telecommunication band, which in combination with its highly controlled low dispersion, allows for a long interaction

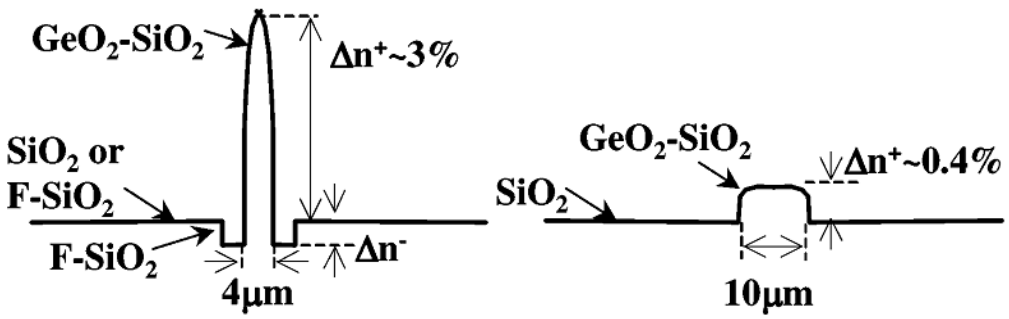

Figure 4: Schematic of Refractive Index Profiles | (left) HNLF (right) Standard SMF. After reference [94] © 2009 IEEE

length [11], [95]. Originally, the future of HNLFs as a practical platform was questioned as it was believed stimulated Brillion scattering (SBS) will inhibit their use [96]. Since then, effective methods for raising the SBS threshold were developed [97]. It is currently accepted that the main limitation of a HNLF based parametric amplification is the fibers' inherent nanometer scale fluctuation of the core size which is caused by limited fabrication control [95].

Despite its high confinement, similarly to a standard SMF, a HNLF is designed to be limited to single mode operation. The HNLF's core has ~30 mol% of GeO_2 doped silica glass, compared with the ~4 mol% doping in a standard SMF's core [98,99]. The core of the HNLF is surrounded by a layer of fluorine doped silica to depress (lower) the refractive index of silica. Its purpose is to make the HNLF a single mode fiber and to add a degree of freedom to its design – for better tailoring of the fiber's dispersion properties [99]. An illustration of the RI profile of a standard SMF and a HNLF is shown in Figure 4. The ratio between the diameter of the core region and the fluorine doped region is ~0.6 [100]. The increased doping in the fiber's core

acts twice by raising both the index contrast and the core's n_2 parameter. The doping result in an increase of n_2 in accordance to [101],

$$n_2\{X{:}GeO_2 - (100\text{-}X){:}SiO_2\} = 2.76 + 0.0974X\ [\times 10^{-20}\ m^2/W], \quad (27)$$

consequently resulting in 2 fold increase of n_2 compared with silica. The index contrast between the core and the silica cladding Δn^+ is proportional to the core doping level, Δn^+ [%] = $0.1X$, where X denotes the doping level in units of mol% [101]. As a result of the increased index contrast, the HNLF's mode area can reduced to ~10 μm^2, that is 8 fold smaller compared with ~80 μm^2 in standard SMF. Hence creating a fiber possessing a nonlinear coefficient γ of ~24 $W^{-1}km^{-1}$ – showing a 16 fold increase compared with a typical 1.5 $W^{-1}km^{-1}$ in standard SMFs [102]. At the same time, however, the increase in mode confinement leads to higher propagation loss α due to enhanced interaction of the mode with the waveguide's core-cladding interface. Therefore causing an increase in the propagation loss α from 0.2 $dB{\cdot}km^{-1}$ in standard SMFs to above 0.5 $dB{\cdot}km^{-1}$ in HNLFs (Table 1). Worse, the tight mode confinement also makes the dispersion properties of the fiber extremely sensitive to the fiber geometry [94], therefore making the efficiency of the nonlinear process vulnerable to random variation in the core area [103].

The relation between the mode confinement in silica fiber and its sensitivity to the fiber's core geometry has been studied in the context of HNLFs. These numerical studies were made by scaling the HNLF's RI profile and solving its eigenvalue equation (at different wavelengths). In this way, the ZDW was calculated as a function of the core's size (diameter), as shown in Figure 5. The RI profile of the core was scaled relative to a 4 μm core diameter and the dependence was plotted for two doping

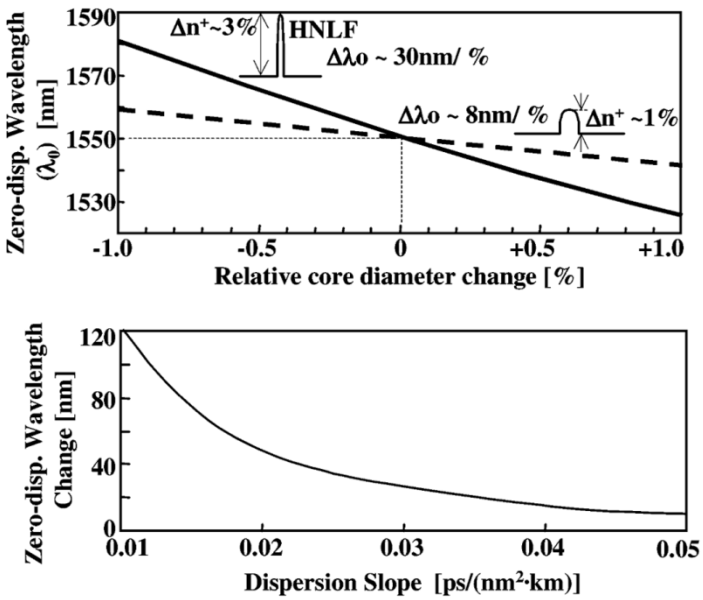

Figure 5: The Relation between Core's Geometry of a HNLF and its Dispersion | (**top**) Claculation of the ZDW as a function of the relative change in the fiber's core diameter .The dispersion slope for the solid and dashed lines is 0.030 and 0.050 ps nm^{-2} km^{-1} respecitvely. (**bottom**) Claculation of the magnitude in which the fiber's ZDW shifts when its core size is scaled from +0.5% to -0.5% as a function of the dispersion slope. After reference [94] © 2009 IEEE

levels. The lower doping level equivalent to 1% core-cladding index contrast, exhibited an 8 nm shift in the ZDW in response to 1% (40 nm) change in the core diameter. Whereas for the profile with higher doping level, simulating a typical HNLF, a 1% change in the core's diameter resulted in a 30 nm shift in the fiber's ZDW. Interestingly, the study showed core variation caused a *linear* shift of the ZDW; this information will be used when simulating this phenomenon. Furthermore, it was shown that HNLFs with a lower dispersion slope *S* will experience a bigger shift in their ZDW in response to core scaling. Generally, lower dispersion slope is highly desired in FOPAs, because then it is possible to achieve better phase matching over a wider range of wavelengths; thus increasing the FOPAs' operating (gain profile) bandwidth. For example, a typical dispersion slope of a HNLF is ~0.030 ps nm^{-2} km^{-1};

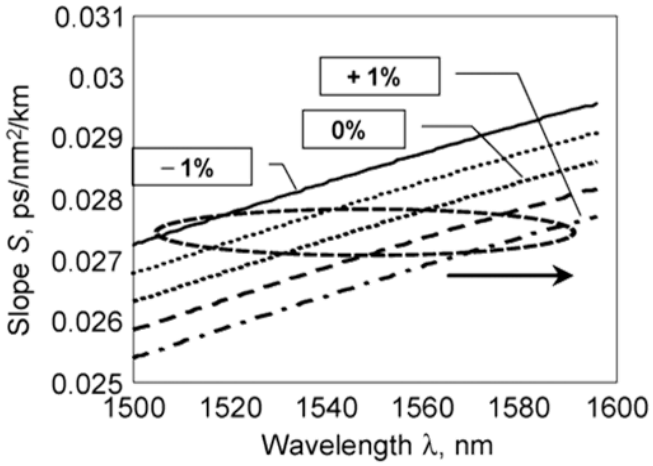

Figure 6: Dispersion Slope Sensitivity to HNLF's Core Scaling | Caluculation of the chromatic dependence of HNLF's dispersion slope at differenct relative changes of its core size. After reference [104] © 2009 IEEE

unfortunately it is difficult to produce dispersion-stable fiber with arbitrarily low *S*. In the case a HNLF is designed with a dispersion slope *S* of 0.010 ps nm^{-2} km^{-1}, the ZDW will shift by 120 nm in response to a 40 nm change in fiber's core diameter (Figure 5), having a detrimental effect on the FOPA's performance.

After describing the affect core scaling has on the fiber's ZDW, another study showed the affect it has on the HNLF's dispersion slope *S* [104]. The study simulated a HNLF RI profile designed with a ZDW at 1560 nm, *S* of 0.028 ps nm^{-2} km^{-1}, and a core diameter of 5 μm[5]. Scaling the core diameter by 1% has shifted the ZDW by 15 nm; meaning a 3.3 nm change in the core diameter leads to 1 nm change in the ZDW. Surprisingly, while the ZDW is highly sensitive to core size variation, the dispersion slope is weakly influenced (Figure 6) and can be effectively described as constant

[5] The information on the core size was omitted from the reference and was obtained through personal communication from its main author.

under nanoscale variations in the core size. This point will be elaborated in the following section which discusses practical FOPA requirements with respect to physical fibers. Reports on the manipulation of ZDW profile of a HNLF, utilize the fact that reduction in the core diameter, e.g. by applying tension on the fiber [105], shifts the ZDW towards longer wavelengths as shown in Figure 5 [94].

In order to provide a perspective on HNLFs' dispersion properties, it's important to present them with respect to conventional fibers such as standard SMF, DSF, and DFF. It is important to note that despise their name DSF and DFF are also single mode fibers. Typical standard fibers will have a ZDW positioned around 1.3 μm, with *S* of 0.090 ps nm^{-2} km^{-1}, and a core area of 80 μm^2. A DSF will have its ZDW shifted towards 1.55 μm, *S* of ~0.060 ps nm^{-2} km^{-1}, and a core area above 50 μm^2. A DFF will typically have two ZDWs, with 1.55 μm wavelength positioned in between, with a value of *D* between –2 and +6 ps nm km^{-1}, and a core area above 50 μm^2. The ZDW of a HNLF is can be similar to either DSF (standard HNLF) or DFF (DF-HNLF). In the case of a standard HNLF, *S* can vary between 0.02 and 0.05 ps nm^{-2} km^{-1}, while for a DF-HNLF the slope will be even smaller, and generally HNLF's affective mode area is smaller than 13 μm^2.

2.2.2. Nonlinear Optical Properties

These unique properties of HNLFs make them a useful platform for nonlinear optics. As was described at the beginning of this chapter, nonlinear optics originates from the polarization of a dielectric by optical fields. Silica fibers including HNLF are made of a centro-symmetric material, causing its $\chi^{(2)}$ coefficient to vanish due to

inversion symmetry. Therefore normally they do not exhibit $\chi^{(2)}$ processes such as SHG. Nevertheless, silica fibers are able to produce such a process, by using either higher order nonlinearities, for example $\chi^{(4)}$, or by treating the fiber using its photo refractive properties [106] to break its inversion symmetry. Hence, the dominating nonlinear optical process in the HNLF is $\chi^{(3)}$. [107]

Third order susceptibility can lead to a variety of optical effects: SPM, XPM, FWM, SBS, SRS, and TPA, all of which can be broadly classified into two groups: parametric and non-parametric. Mathematically, $\chi^{(3)}$ is a complex variable which can be expressed as $\chi_3 = \chi_3' + i\chi_3''$. Parametric interactions originate from the real part of the susceptibility χ_3', while non-parametric interactions stem from its imaginary part χ_3''. Physically, a parametric interaction is classified as an effect in which the process is lossless, namely the material's excitation is virtual (the excitation starts and ends at the same state without using a real intermediate transition) so that no real net power flows from the total field to the material. Therefore a parametric process is far from resonance where Manley-Rowe relations and permutations symmetry are valid. A nonlinear interaction which does not fall into this category can be classified as a non-parametric process. [92]

Amongst the parametric processes: SPM and XPM are independent of phase matching, while FWM is a phase matching dependent process; however the non-parametric processes: SBS, SRS, and TPA are all independent of phase matching (although they do subject to selection rules). In the context of HNLFs, SBS and SRS

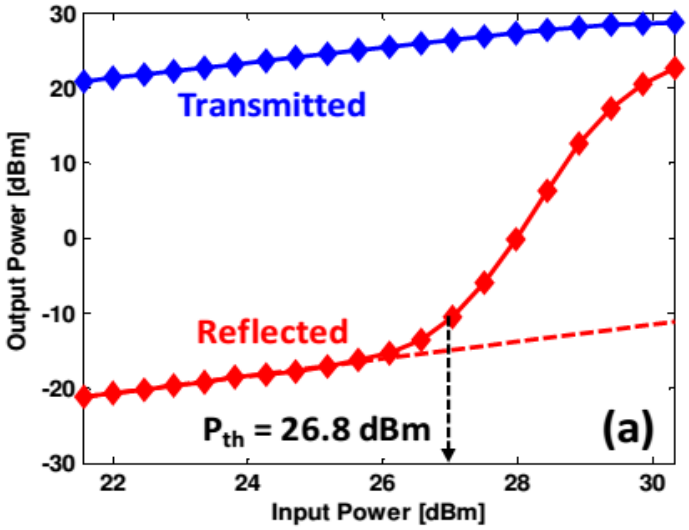

Figure 7: Characterization of the SBS in a HNLF | A measurement of the transferred and back reflected optical power as a function of the HNLF's input power. In the absence of a counter propagating signal the process initiate by spontanous Brillouin scattering. After reference [108]; © 2012 OSA. Reprinted with permission from The Optical Society.

are important effects while TPA in glass doesn't exist in the telecom band region.

SBS is an effect which couples the pump with the fiber's acoustic phonons. As a result of the coupling, initially, pump photons are back reflected in a spontaneous Brillouin scattering process, as a result of this inelastic scattering, the reflected light is frequency down shifted by ~10 GHz. The down shifted scattered light together with the pump excite more phonons which increase the pump scattering. Consequently, SBS puts a limit on the amount of power which can pass through the fiber [109], and has a typical characteristic behavior as shown in Figure 7. Although SBS has a narrow ~50 MHz bandwidth, its SBS gain is considered to be strong, and is inhibiting the pump from reaching to the required CW power level for parametric amplification. Under the assumption of an undepleted pump and negligible propagation loss, the counter propagating signal (from L to 0) in a silica fiber will experience an exponential gain,

$$I(0) = I(L)\exp\left(\frac{g_B}{A_{eff}} PL\right), \tag{28}$$

where the SBS gain g_B is 5×10^{-11} m W^{-1}. In the case of HNLF, g_B/A_{eff} is equivalent to a γ of 5000 W^{-1} km^{-1}. Using Eq. (28), it is possible to extract a threshold pump power level in which a spontaneous Brillouin scattering will cause the scattered light to be amplified to half of the pump power level; and can be expressed as [110]

$$P_{th}^{SBS} = \frac{21A_{eff}}{g_B L_{eff}}\left(\frac{\Delta\nu_B \otimes \Delta\nu_P}{\Delta\nu_B}\right), \tag{29}$$

where $\Delta\nu_B$ and $\Delta\nu_P$ represent the SBS gain BW and the pump BW, respectively. Given silica fiber's SBS gain BW $\Delta\nu_B$ = 20-50 MHz [4], successful methods were able to suppress SBS by either broadening $\Delta\nu_P$ of a CW pump [111] or by operating the pump in a pulsed mode. In the latter case, for a pulse width shorter than the phonon lifetime ($1/\Delta\nu_P$), say ≤ 1 ns, depending on the repetition rate R, the SBS threshold will be calculated as follows: If $R << \Delta\nu_P$ any excitation will have enough time to decay before the arrival of the consecutive pulse. If $R >> \Delta\nu_P$ then it is possible to use the pump average power to evaluate whether the SBS threshold is surpassed. In the last case, if $R \sim \Delta\nu_P$ or alternatively the pulse width is longer, one should resort to SBS dynamic to evaluate SBS threshold level.

SRS is based on the same principals as SBS; however, conversely to the latter, SRS relies on the optical phonons to scatter the pump. For this reason, SRS gain in silica fiber [112] is relatively weaker and has a broader BW. The optical phonons' dispersion relation, enables SRS forward scattering of the pump's photons in SMF,

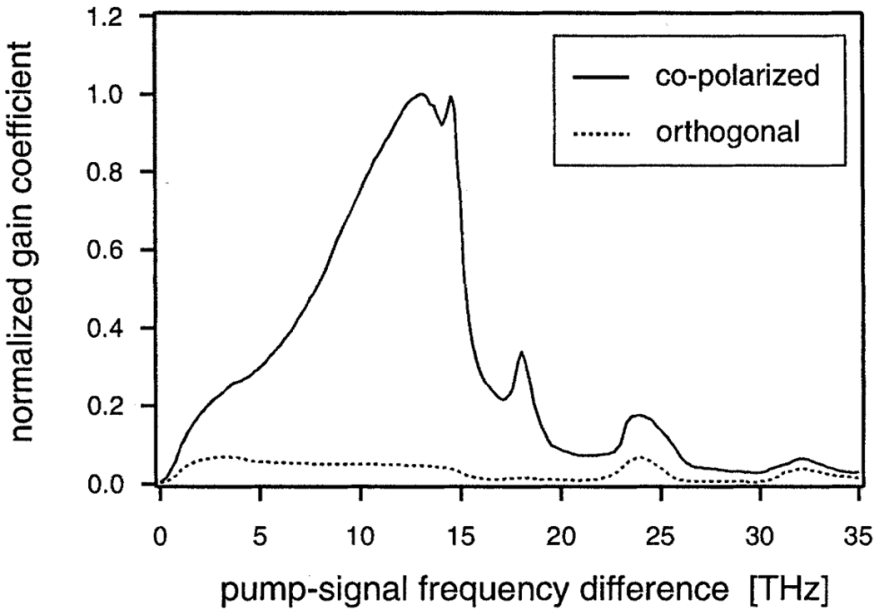

Figure 8: SRS Gain Profile in Fused Silica | Normalized Raman gain g_R frequency dependece in fuesed silica. The peak gain is located at about 13 THz away (lower) from the pump frequency. At its peak value $g_R = 10^{-13}$ m W^{-1} at pump wavelength $\lambda_P = 1$ μm; and its value scales inversly with the pump wavelength [113]. After reference [114] © 2004 IEEE

where its wide BW, as shown in Figure 8, is attributed to the amorphous nature of silica fibers [114]. The peak of the SRS gain profile g_R is down shifted 13 THz away from the frequency of the pump and was evaluated as 6×10^{-14} m W^{-1} when positioning the pump wavelength λ_P at 1.55 μm. Consequently, in a similar manner to Eq. (28), the SRS gain in a HNLF results in g_R/A_{eff} of 6 W^{-1} km^{-1}. When compared with HNLFs nonlinear coefficient ($\gamma \geq 15$ W^{-1} km^{-1}), the effect of SRS can be neglect provided that one or more of the following occurs in a sufficient manner: (1) the parametric process has a good phase matching to provide efficient amplification. (2) SRS peak gain occurs 13 THz (100 nm) away from the pump; in comparison, the input signal of a parametric amplifier is positioned where the parametric gain (phase matching) is maximized (optimized), which is typically positioned closer to the pump, on the order of 10 nm. Thus, unlike the parametric process which is seeded by a

signal, SRS will be seeded by the vacuum noise. (3) As the signal and pump beams interact in the HNLF, by-products in the form of newly generated optical tones will be created, therefore extending the occupied BW around the spectral position of the pump. A properly designed FOPA will reduce the exposure of the optical by-products to SRS gain. [113]

Conversely to SRS and SBS, the parametric response in HNLF is based on the real component of the third order susceptibility χ_3'. Physically, there are two components to χ_3', electronic and nuclei (optical phonons), which can be described as a sum of two individual contributor to the nonlinear refractive coefficient n_2. In practice, (*i*) the electronic response time is sub-femtosecond [115], and (*ii*) the nuclear response time can be evaluated from the measured SRS gain profile (Figure 8) and found to be ~30 fs [14]; additionally, the former contributes to 82% of the parametric process in silica fibers. Generally, unless the field propagating in the fiber forms (1) a sufficiently strong, ultrafast waveform to produce self-steepening, or (2) an efficient wide band parametric mixing process, the system can be described using the adiabatic limit in which the nonlinear response can be approximated as instantaneous, $\gamma|A|^2 A$, in a ~140 nm BW around the pump. [13,116]

For the sake of completeness, an extended description of the nonlinear term in NLSE, Eq. (16), is briefly provided, in case the nonlinear polarization response cannot be treated as instantaneous. Generally, various treatments can be found in the literature, covering different degrees of approximations; as well as a variety of approach for the physical description of this phenomenon. The following derivation is

based on the approach described in [116,13]. In the general case the nonlinear term in NLSE can be modified as follows

$$\gamma|A|^2 A \rightarrow A(z,t)\int_{-\infty}^{t} dt' R(t-t')|A(z,t')|^2 , \tag{30}$$

where R is the response function given as

$$R(t) = (1-f_R)\delta(t-t_e) + f_R h_R(t). \tag{31}$$

The left and right terms on the RHS of eq. 30 represent the electronic and the Raman contribution, respectively; f_R represent the fractional contribution of Raman to the nonlinear response, t_e represents < 1 fs delay in the electronic response, which is often neglected, and $h_R(t)$ represent the Raman's response. By using the relation between $h_R(t)$ and (the measured) SRS gain profile it is possible to both calculate $h_R(t)$ and to extract the value of f_R. In case the BW is significantly wide, it is possible to introduce a chromatic dependence to the nonlinear coefficient of the fiber in the following form,

$$\gamma|A|^2 A \rightarrow i\left(\gamma + i\gamma_1 \frac{\partial}{\partial t}\right)\left(A(z,t)\int_{-\infty}^{t} dt' R(t-t')|A(z,t')|^2\right). \tag{32}$$

The time derivative term represent a linear frequency dependence of γ. In a likewise manner, higher order term may be added. The need for this arises in wide band systems, for example as in octave-combs, where frequency-distant modes experience different levels of confinement. In practice one can always simulate with and without the delayed response, to check whether it is needed.

Chapter 3

Operation of Inhomogeneous Fiber-Optic Parametric Amplifiers in Deep Saturation

3.1. Introduction

Since its early inception [1], optical parametric amplifiers (OPA) have been studied and implemented with variety of physical platforms. In contrast to conventional amplification devices [117,118,119], parametric amplifier response is ultrafast since it originates with either three- [120] or four-photon [121] processes. With inherent frequency conversion capability, ultrafast OPA can manipulate optical frequency and photon state in a manner that cannot be matched by conventional amplifiers even in principle [122].

An OPA can be viewed as a photon-exchange device designed to transfer the pump to signal/idler frequencies [123] and simultaneously control the state of newly generated waves [124]. While simplistic, this model leads to correct description of parametric amplifier operating in the saturation regime [28]. Indeed, weak signal sent to high-gain OPA is not only amplified but can also deplete the pump and create multiple idler beams with comparable powers [125]. Saturated behavior was studied extensively in general [27] and fiber OPA (FOPA) platforms [29,123,126]. Marhic has demonstrated early [123] that near-ideal wavelength exchange is possible with highly

efficient FOPAs. Saturated regime was used to improve signal regeneration performance in one- and two-pump amplifiers [126]. Recently, Andrekson has pointed to an important switching role that ultrafast FOPA operating in saturation can play in high-rate systems [29].

The degree of OPA saturation is defined by the efficiency of the signal-pump parametric exchange. In ideally phase matched device, pump-signal interaction strength scales with product of its nonlinearity, pump power and effective mixer length [28], commonly referred to as nonlinear figure of merit (FoM). While high FoM can be routinely reached with high-peak (pulsed) pumps, it is not of particular interest when the arrival of the signal photon is a random event that dictates either continuous-wave (CW) or quasi-CW OPA operation. With great diversity of physical platforms explored during the last decade [127,11], it can be shown that none, to the best of our knowledge, possess FoM comparable to that of highly nonlinear fiber (HNLF) [94]. This is rather surprising since silica nonlinearity remains nearly two- and three-orders of magnitude below that of silicon and chalcogenide material respectively [65,128]. The weak nonlinearity is balanced by its unmatched transparency, allowing for very long photon interaction lengths and, ultimately, to the superior FoM. Indeed, even if we assume that silicon has no impairments associated with CW pumping [129], its FoM is nearly two orders of magnitude lower than HNLF at practical CW pump levels [130]. Motivated by this fact, we specifically investigate physical limits of saturated, high-FoM FOPAs.

More importantly, this work is also motivated by a need to map a weak, fast signal variations on a strong optical beam. Intuitively, if high-FoM FOPA can be

realized, then even a few-photon signal should be sufficient to deplete many-photon pump in nearly instantaneous manner. This goal seems to be within easy reach since large FoM can be reached by merely increasing the length of low-dispersion HNLF [94]. Not only that such device would represent an ultrafast, low-energy switch as originally pointed by Andrekson [29], but it would also be universally applicable in fast sensing of weak photon beams.

Unfortunately, two basic limitations must be circumvented before the construction of such device is possible. Firstly, the transfer characteristics of high-gain FOPA critically depend on the vacuum noise [131], particularly in a case when the input signal is weak. Secondly, high-FoM FOPA is necessarily a *distributed parametric device that is still governed by a localized phase matching* [105]. While a long fiber implies high FoM in case *when its dispersion can be controlled with arbitrary precision*, this condition cannot be met with physical fibers [103]. Indeed, even nanometer-scale transverse fluctuation will lead to local dispersion variation that can drastically reduce the efficiency of the parametric process [132]. Worse, physical fibers are characterized by *stochastic* transverse fluctuations [104] that can effectively destroy the intuitive notion of high-FoM fiber parametric mixer [103]. While the vacuum noise can be spectrally inhibited [120], randomly fluctuating phase matching in long fiber cannot be easily suppressed.

Recognizing this limitation, we study the performance of dispersion-perturbed, high gain FOPA driven by weak signal to characterize its response. We show that dispersion localization is not only critical for achieving saturation in high-FoM mixer

but prove for the first time, to the best of our knowledge, that dispersive fluctuation lead to nonreciprocal FOPA transfer function.

Consequently, this chapter is organized as follows: in Section 3.2 we introduce a homogeneous (zero-fluctuation) FOPA model incorporating vacuum noise to study saturation with weak input signal; Section 3.3 introduces dispersion fluctuation (inhomogeneous) FOPA model and applies it to physical FOPA driven by weak signal. Finally, in Section 3.4 we show that inhomogeneous FOPA possesses truly nonreciprocal transfer function.

3.2. Small-Signal FOPA Saturation: Homogeneous Model

We limit the discussion in this section to that of a single-pump FOPA [124] to preserve the clarity; while multiple-pump model can be derived by following a similar procedure, it exceeds the scope of this report.

The simplest description of one-pump FOPA is provided by three-wave model in which CW signal and pump waves are launched into a lossless, longitudinally invariant (homogeneous) HNLF section. This model neglects the vacuum noise [131], higher-order idler creation [126] and phase matching independent interactions such as Raman and Rayleigh scattering. Following the analysis of Trillo [27], a FOPA is described by a closed set of coupled-mode equations with unique phase matching solution. It predicts that, when phase matching condition $\Delta k = k_S + k_I - 2k_P$ (S, I and P corresponding to signal, idler and pump waves) reaches a unique value:

$$\Delta k = -\left(1 - 3\frac{P_{SIG}}{P_{IN}}\right)\frac{\gamma P_{IN}}{2}, \tag{33}$$

the pump power P can be transferred to a signal (idler) in monotonic manner [27]. In this case, coupled mode description allows for closed analytic expression for the normalized pump power at the fiber output L:

$$\eta = \frac{P(L)}{P_{IN}} = \frac{\eta_+\eta_-\left(\tanh^2(a\xi) - 1\right)}{\eta_- \tanh^2(a\xi) - \eta_+}, \tag{34}$$

where:

$$\eta_- = \frac{P(0)}{P_{IN}}; \eta_+ = 1 + \frac{25}{7}\frac{P_{SIG}}{P_{IN}}; a = \frac{\sqrt{7\eta_-\eta_+}}{4}; \xi = \gamma P_{IN} L \ ,$$

$P_{IN} = P(0) + P_{SIG}$ is the total input power, and γ is the fiber nonlinear coefficient. In practical terms, Eq. (34) can be used to estimate the pump depletion $P(L)/P(0)$ as a function of the interaction strength $\gamma P(0)L$, input pump power $P(0)$, and input signal power P_{SIG}. Although the interaction strength in Eq. (34) is defined using P_{IN}, for all intended purposes P_{IN} may be approximated as the input pump power. Figure 9 shows the pump depletion when the phase matching is set to the monotonous transfer condition defined by Eq. (33). Since our primary interest is to describe the operation of pump-depleted amplifier driven by a weak signal, the figure maps signal inputs below 10 μW (-20 dBm). As expected, the model predicts that any pump depletion can be realized with arbitrarily small signal, as long as FOPA possesses sufficiently high FoM. As an illustration, consider a realistic HNLF segment (γ = 30 $W^{-1}km^{-1}$, L = 1000 m) pumped by a conventional 500 mW diode. The model predicts that a sub-microwatt (P_{SIG} ~ 0.1 μW) signal is sufficient to cause 99% (-20 dB) pump depletion; similarly, a 50% (-3 dB) depletion requires 1 nW input signal. If we assume that the

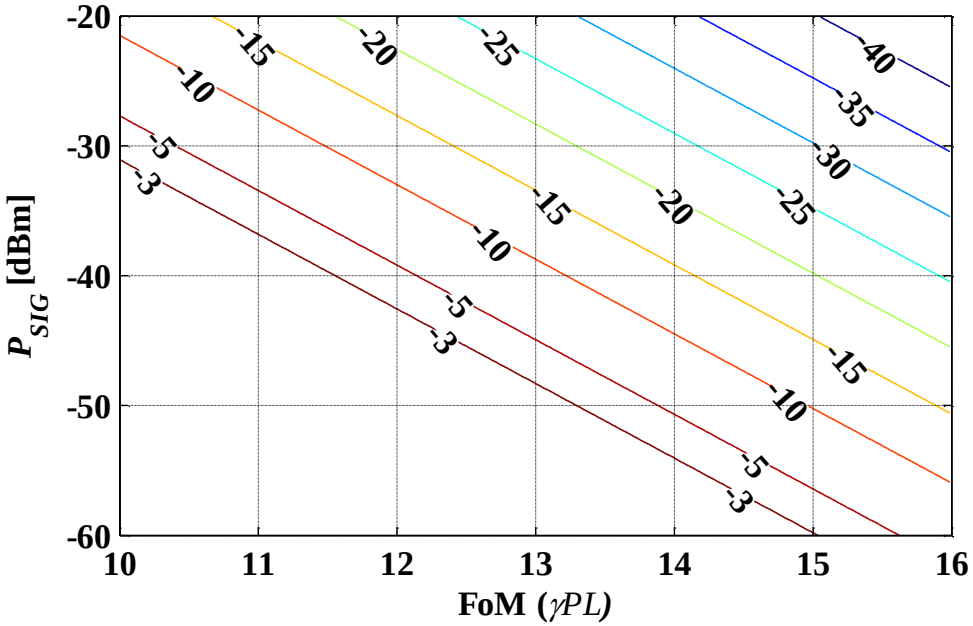

Figure 9: Pump Depletion in a Noise free Three Wave Model | The pump depletion of a single pump FOPA when phase matching condition is set to the monotonous transfer condition defined by Eq. (33). The pump depletion $P(L)/P(0)$ is described in decibels as a function of signal input power and the FOPA figure of merit. The result is based on the analytical solution presented in Eq. (34), given $P(0)$ = 500 mW.

input signal occupies 10 GHz bandwidth, then this power would be approximately equal to the vacuum noise level within the same band. Worse, if the input signal is absent, three wave model predicts no pump depletion, regardless of FOPA FoM, would occur. Both indicate a clear limit of the noiseless, three-wave homogeneous parametric model. Consequently, if FOPA saturation by a small signal is to be described in more physical terms, a three wave homogeneous model must be generalized by the inclusion of vacuum noise and higher-order idler generation.

Even when physical signal is absent, FOPA amplifies virtual photon input [133]. The vacuum noise seeds the parametric amplifier in achromatic manner and FOPA phase matching condition then defines the spectral band over which amplification occurs. In case when FOPA operates as a broadband device (spectrally

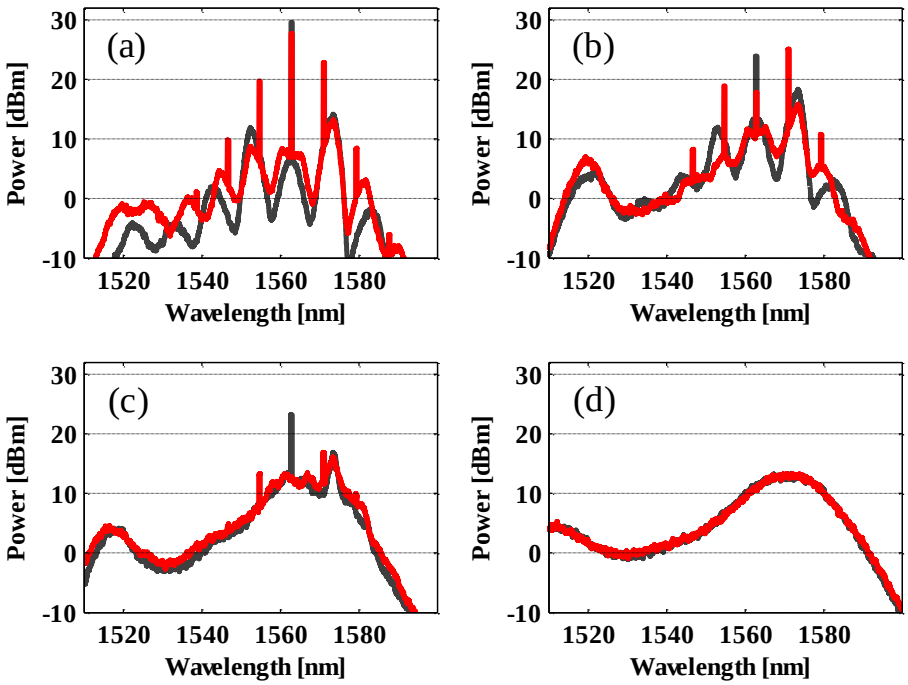

Figure 10: FOPA Spectral Response in the Presense and Absence of a Weak Input Signal | FOPA spectral response is presented at different FoMs: figures (a)-(d) correspond to FOPAs with a FoM of 8, 9, 11.5, and 18, respectively. The gray (bright) and red (dark) traces correspond to signal off and on (-35 dBm) respectively, with a resolution bandwidth set to 0.4 nm. The simulation was solved for the following parameters: λ_0 = 1550 nm; λ_P = 1562.83 nm; $\lambda_{SIG} = \lambda_P$ + 8.21 nm; S = 47.82 s/m^3; α = 0.77 dB/km; γ = 18.29 W^{-1}km^{-1}; $P(0)$ = 31.44 dBm; Time window of 5.12 ns; Sample rate of 25.6 THz. Figures (a) to (d) were generated using fiber length corresponding to 323.04 m, 364.75 m, 470.99 m, and 754.73 m. The FOPA FoM was calculated using the fiber effective length, $L_{eff} = [1-\exp(-\alpha L)]/\alpha$.

uninhibited operation), a significant portion of the originally launched pump can be converted to the amplified vacuum noise (parametric fluorescence), even in case of moderate parametric gain [12,134]. New, noise-seeded frequencies generated via pump modulation instability will act as spectrally continuous signal, leading to further pump depletion even in the absence of the physical input signal. As a result, it will become increasingly difficult to separate pump depletion contribution from amplified vacuum noise and a weak input signal. Contrary to three-wave model prediction shown in Figure 9, decrease in input signal power cannot be matched by mere increase

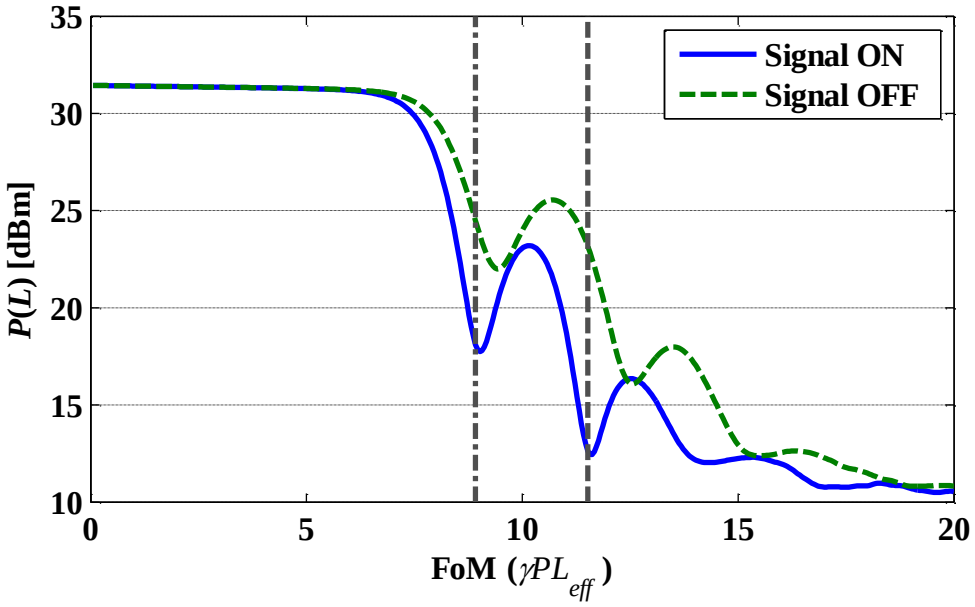

Figure 11: FOPA Saturated Behavior as a Function of its FoM | The output pump power simulated for a FOPA in absence and presence (-35 dBm) of the input signal. The FOPA ON/OFF depletion contrast is locally maximized at FoM of 8.9 (dot-dash) and 11.5 (dash), and shows a contrast of 6.4 dB and 10.45 dB, respectively. The simulation parameters are the same as in Figure 10.

in HNLF length (or, equivalently, increase in FOPA FoM); when spectrally integrated vacuum noise becomes comparable to the input signal, the pump depletion contributions are no longer separable.

Furthermore, a signal-noise induced pump depletion is accompanied by an additional mechanism in high gain FOPA that inherently generates higher-order idlers [125]. To illustrate this, three-wave model is replaced by nonlinear Schrodinger (NLS) model [13] of FOPA seeded by an achromatic vacuum noise. The model was used to calculate FOPA response with increasing FoM, as shown in Figure 10. In case when weak signal (P_{SIG} = -35 dBm) is amplified in FOPA with FoM < 10, pump depletion is clearly driven by signal-idler generation. Conversely, as FoM grows vacuum noise

amplification and signal interaction (FoM = 11.5) dominate the pump depletion process; the input signal role becomes negligible with FoM = 18.

A considerable insight can be obtained in case when pump depletion is compared for FOPA in absence and presence of the input signal, as shown in Fig. 3. In case when FOPA is too short (FoM < 7), the parametric interaction is too weak to deplete the pump appreciably. In a special case (FoM = 8.9), the amplifier exhibits high sensitivity to the input signal, leading to 6.4 dB ON/OFF depletion contrast. The maximal sensitivity is exhibited with FoM = 11.51, in case when pump depletion is dominated by vacuum noise amplification and signal/idler creation.

It is sufficient to observe the depletion effect while increasing FOPA FoM and note the range in which the mixer becomes dominated by amplified vacuum noise, thus losing the sensitivity to the input signal. Figure 11 shows an example of FOPA saturated behavior as a function of its FoM, when vacuum noise and higher order idlers are accounted by homogeneous NLS model.

3.3. Small-Signal FOPA Saturation: Inhomogeneous Model

OPA sensitivity to small signals can be increased by spectrally inhibiting the amplification of vacuum noise. In conventional approach, OPA is embedded within resonant structure [120] that suppresses the creation of new frequencies outside of the intended pass band. In case of distributed mixer such as FOPA, a more promising approach would comprise of gain synthesis that matches either the input signal or

select idlers bandwidth. Such spectral inhibition would guarantee that pump depletion not originating with the input signal be limited to noise confined to the specific (signal/idler) band. However, long before reaching FOPA sensitivity levels that would justify vacuum noise suppression, one must first address the stochastically varied nature of distributed parametric interaction. This also means that we must dispense with homogeneous model description of high FoM mixers. Indeed, the homogeneous FOPA model rests on a simple, but false premise that fiber physical characteristics are constant along its entire interaction length. As seen in previous section, this leads directly to the conclusion that a mixer with an arbitrary efficiency can be trivially constructed by merely extending the fiber.

Unfortunately, the very assumption that local phase matching can be maintained over hundreds of meters of interaction length also means that fiber transverse geometry cannot be perturbed [103]. Local phase matching (dispersion) in FOPA is directly defined by the corresponding modal distribution [135], which, in turn, is dictated by the effective index and waveguide geometry [136]. The importance of transverse core fluctuations have been recognized and extensively studied in case of wideband parametric amplification [33,104,105,132,137,138,139,140,141,142], [15,143]. Both experimental [33,104,105,137,138,139,140,141] and theoretical studies [132,142,15,143] have confirmed the existence of the stochastic bandwidth limit [103] imposed as a consequence of random phase matching along the fiber length. In case when FOPA is designed to operate in linear (unsaturated) regime, small HNLF fluctuations were sufficient to decrease its bandwidth considerably, reduce gain and affect spectral equalization [105,132]. A conventional HNLF index profile is

specifically designed to provide high confinement [94] and is very sensitive to transverse scaling effect: even a small change in a core radius can have significant impact on its dispersive properties. Indeed, it is only necessary to perturb the HNLF core by a percent to generate tens of nanometers variations in its zero-dispersion wavelength (ZDW) [94,104]. As HNLF core radius measures approximately 1.6 μm, this also means that nanometer-scale fluctuations will result in drastically different local parametric response for fibers that are otherwise indistinguishable, in global (macroscopic) terms.

As long as FOPA bandwidth is comparable to the conventional communication (~100 nm) band, the effect of HNLF transverse variations can be accurately modeled by ZDW shift while keeping the dispersion slope constant [104]. This approximation is not only accurate but is also instructive as it allows for an intuitive understanding of the core impairment mechanism. Indeed, if ZDW shifts are large enough, they can randomly translate the pump frequency from the anomalous (amplifying) to the normal (attenuating) dispersion regime, thus qualitatively changing the photon exchange along the FOPA interaction length.

By establishing clear equivalency between transverse HNLF geometry fluctuations and ZDW variations, the performance limits of saturated FOPA can be studied by longitudinally-varied ZDW model [142]. Specifically, we identify the continuous variation model [142] in which ZDW fluctuations are represented by correlated Gaussian noise, defined by the correlation length and standard deviation parameters. To describe physical FOPA behavior, an ensemble of HNLFs was generated, with each member possessing dispersive fluctuations constrained by the

realistic fabrication limit [94]. For each HNLF realization, stochastic transverse fluctuation was modeled by zero-mean ZDW perturbation profile $\delta\lambda_0(z)$. At any point along FOPA, local HNLF ZDW is then defined by $\lambda_0(z) = \lambda_0 + \delta\lambda_0(z)$, where λ_0 denotes the *global* ZDW satisfying $<\lambda_0(z)> = \lambda_0$. This normalizes *global* ZDW for all ensemble members and guarantees that HNLF samples under investigations remain indistinguishable in macroscopic terms. Indeed, any shift in global ZDW can be regarded as a dispersion offset that can be measured by accessing two fiber ports and subsequently compensated by merely repositioning the signal and pump. In contrast, local ZDW fluctuations, as long as they are described by zero-mean process, cannot be compensated, even in principle, by shifting the pump and signal wavelengths. Finally, each HNLF realization is treated as an independent FOPA and is modeled using NLS model with identical input (power and wavelength) conditions, nonlinear parameter, loss and dispersion slope across the ensemble population. The procedure guaranteed that the operation of saturated FOPA was investigated using *globally identical fibers*, emulating the condition one faces with physically realizable device.

NLS solution of each HNLF sample generated full field FOPA description posing an interpretation challenge, particularly in case of a large ensemble. To gain an insight, we limit the observation only to physically measurable parameters originally motivating this study. Consequently we consider the performance of one-pump device in which weak (signal) beam interacts with strong (pump) beam, as shown in Figure 12. Since this topology strongly resembles the conventional notion of photon-photon gate and single photon switching [29,80,87,88,90,144,145], we use the terms FOPA and photon gate interchangeably henceforth. The performance of such gate is

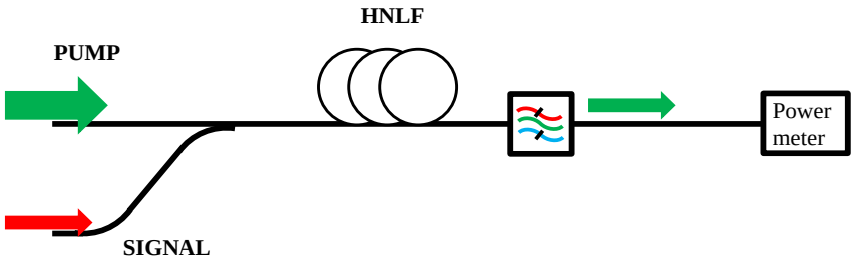

Figure 12: Schematic Description of a Generic Distributed Photon Gate System | The scheme illustrate a weak (signal) and a strong (pump) beams which are coupled into a HNLF. The system is designed to saturate in a presence of signal. Following the interaction, the pump is optically filtered and detected. The system is rated by its ability to directly manipulate the strong beam using the weak beam.

considered higher if a weaker signal can induce higher pump extinction (depletion). The second aspect of its performance, gate speed, will be addressed subsequently.

The signal and pump were combined and sent to a HNLF section with dispersion fluctuation and pump power at the output of the mixer is measured for each ensemble member. The pump power was measured in the temporal domain, both in presence of the input signal and in its absence. The performance of the gate is evaluated in terms of the extinction ratio (ER), defined as the ratio of the pump output power in absence of the input signal (P_{OFF}) and its presence (P_{ON}). Since the HNLF ensemble size must be finite, it poses a challenge with respect to gauging the effect of the stochastic dispersive variations on FOPA performance parameter such as ER. Recognizing this problem, we devised a simple strategy that compares ER of stochastically varied HNLF to that of ideal (homogeneous) fiber. In first step of this investigation, we have sought physical parameters of homogeneous FOPA with respect to ER. Specifically, we considered a longitudinally uniform HNLF segment with maximal ER with CW input signal set to -35 dBm (0.31 μW). To define such HNLF, we used a conventional Simplex optimization [146] operated under constraints

of practical HNLF fabrication limits for loss ($0.5 < \alpha < 1$ dB km^{-1}), nonlinear coefficient ($10 < \gamma < 20$ W^{-1}km^{-1}) and dispersion slope ($0.03 < S < 0.05$ ps km^{-1}nm^{-2}). The ZDW was centered at 1550 nm, pump power was limited to 1.5 W (31.8 dBm) and HNLF length to 500 m. The optimal ER of 11.46 dB was reached for a unique HNLF homogeneous segment possessing $\alpha = 0.77$ dB km^{-1}, $\gamma = 18.29$ W^{-1}km^{-1}, $S = 0.0478$ ps km^{-1}nm^{-2} and $L = 470.99$ m. The optimized gate was driven by 31.44 dBm pump centered at 1562.83 nm and signal was centered at 1571.04 nm. The vacuum noise was generated using an identical seed during the parameter sweep while the pump power was measured using 50 GHz wide bandpass filter.

After identifying the optimal homogeneous HNLF segment, we have effectively obtained the calibration gauge that can be used to measure ER performance of a stochastically fluctuating fiber. Consequently, HNLF ensemble was generated by perturbing the ZDW to obtain fluctuation map $\lambda_0(z)$. The ensemble shared the global (mean) ZDW, $\langle \lambda_0^{(i)}(z) \rangle_z = \lambda_0 = 1550$ nm while the standard deviation (STD) was defined as $\sigma^2 = \langle \delta\lambda_0(z)^2 \rangle$ where $\delta\lambda_0(z) = \lambda_0(z) - \lambda_0$. Maximal STD was constrained below 8 nm, in accord with recently reported HNLF fabrication tolerances [94]. The ensemble was composed of 6000 realizations and each one was characterized with respect to STD (σ) and ER. The results are presented in Figure 13, showing an x-y scatter distribution of the entire ensemble. Each point in the plot represents a single realization performance characterized by ER(i) and its standard deviation $\sigma(i)$, where $1 \leq i \leq 6000$.

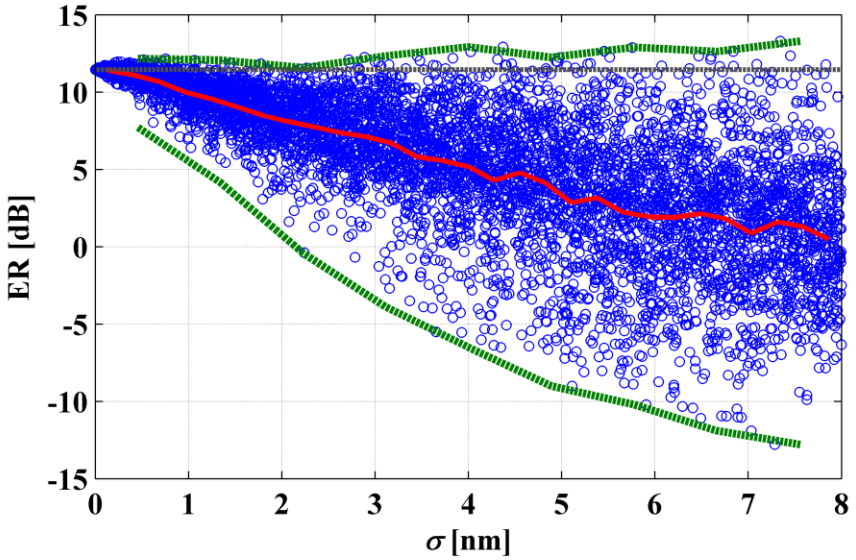

Figure 13: Performance Limit of a Deeply Saturated FOPA Subject to ZDW Fluctuations | Each point in the figure represents a member of the HNLF ensemble, all of which share identical global properties. The members were treated as independent FOPAs, simulated under identical input conditions, and were characterized with respect to their ZDW STD (σ) and ER (P_{OFF}/P_{ON}). The horizontal gray line represents the gate ER level (11.46 dB) when the sample is homogeneous (σ = 0). The red line represents an average ER vs. STD, with green lines illustrating the upper and lower limit of the distribution. The ensemble was generated using a correlation-length parameter set to 250 m, which is about half of the length of the fiber, a time window of 1.28 ns, and a sample rate of 25.6 THz.

The perturbation condition used the continuous variation model [39] to represent $\delta\lambda_0(z)$ as a zero-mean, correlated Gaussian noise. In the process of creating the ensemble, many fluctuation maps were generated using model-parameters' setting of: 250 m correlation length, and standard deviation which varied between members. As it was important to sample in a uniform manner, σ-axis was divided to 6,000 bins from 0 to 8 nm. Following the creation of each fluctuation map, its σ was characterized and only those with a σ corresponding to an empty bin were selected as member of the ensemble, where others were discarded. This process continued until no bin was left empty.

We have specifically chosen to plot the pump extinction ratio against the standard deviation characterizing the stochastic phase matching fluctuation in each HNLF ensemble member. This choice gives not only a direct measure of the gate performance but also provides an insight in its operation. Firstly, as the magnitude of fluctuations grows, signal-induced pump depletion diminishes. While the uniform ($\sigma = 0$) fiber corresponds to ER of 11.46 dB, dispersion fluctuations with only $\sigma = 2.2$ nm are capable of cancelling any signal effect (ER = 0). Since glass matrix is composed of silicon-oxygen rings that are only 0.6 nm in diameter [147], this also means that fluctuations measured by only four Si-O molecular diameters can, at least in principle, lead to the total function loss. To note a likely performance degradation, we note that the averaged ER across the ensemble with 2.2 nm STD is only 8 dB. In practical terms, this means that random trials of HNLF possessing molecular-scale core fluctuation are likely to produce less than 50% of the homogeneous gate performance. Secondly, as ZDW deviations grow beyond 2.2 nm, we observe a finite probability that logarithmic ER assumes negative value. Physically, this means that the vacuum noise is more efficient in depleting the pump for a particular HNLF dispersive fluctuation realization than when the signal is present. Worse, the ensemble-averaged ER severely degrades (ER ~ 2 dB) when dispersive fluctuations reach 6 nm – the condition corresponding to most physical fibers in use today.

3.4. Inhomogeneous FOPA non-Reciprocity

The ability to construct a high-FoM mixer originates in the distributed nature of parametric process supported by nearly lossless fiber waveguide. It is also this

distributed characteristic that prevents the construction of mixers with very high FoM. Indeed, the transverse control required for a long mixer device poses a fundamental challenge that is not necessarily easier to overcome than the limit imposed by optical loss in non-silica (lumped) mixer devices. Until we identify the physics that can synthesize low-loss fiber waveguide and guarantee that its transverse geometry control is comparable to the constituent (SiO_2) molecular scale, any high-FoM mixer construction will have to incorporate the knowledge of distributed fluctuations.

However, the very fact that stochastic fluctuations lead to different outcomes in saturated, high-FoM mixers also opens a path to new applications that were not considered in the past. Indeed, since the pump depletion (and mixer response) critically depend on the longitudinal evolution of the local phase matching, it is intuitively plausible to expect that this process is not spatially reversible. In practice, the question can be articulated in terms of inhomogeneous FOPA reciprocity: if high-pump depletion can be achieved in specific HNLF, will reversing its port change the response of the device? While Marhic [148] has originally shown that inhomogeneous FOPA operating with non-depleted pump is strictly reciprocal, this analysis needs to be generalized for a case when high mixer FoM allows for finite pump depletion.

To investigate reciprocity of inhomogeneous FOPA, we consider 500 m-long HNLF realization possessing ZDW variation smaller than 4 nm, as shown in Figure 14(a). The fiber is characterized by γ = 15 $W^{-1}km^{-1}$ and S = 0.025 ps $km^{-1}nm^{-2}$ and used in single-pump architecture illustrated in Figure 12. The HNLF was pumped by a CW pump centered at 1554 nm with 1 W power and combined with CW signal tuned with respect to power (-40 < P_{SIG} < -20 dBm) and wavelength (5 < $\lambda_{SIG} - \lambda_{PUMP}$ < 15

nm). Each wavelength-power state of the input signal was used to calculate ER of the device; the aggregate result is plotted as a performance map shown in Figure 14, (b) and (c).

The ER is shown in case when the device is operated in two directional modes: Figure 14(b) indicated pump-signal launched at port A of the fiber while Figure 14(c) corresponds to port B launch condition. While the FOPA response is obviously different in two cases, indicating true non-reciprocal transfer characteristics, a distinct set of characteristics can be identified in both operational regimes. When the signal is off, the pump output power is P_{OFF} 29.16 dBm for both directions. In small-signal regime (P_{SIG} < -32 dBm), the signal induced pump depletion remains below 2 dB and the

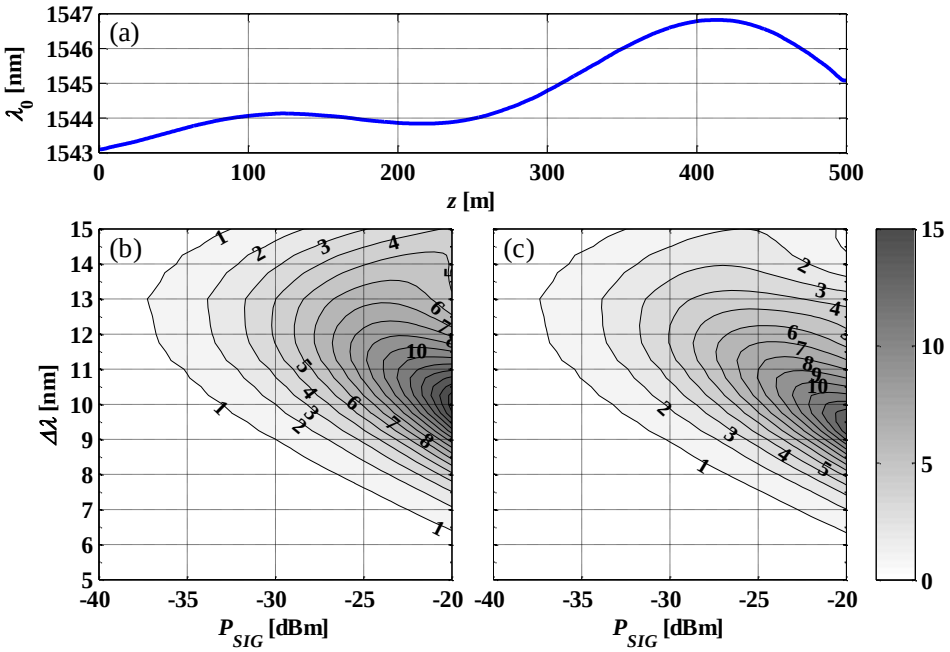

Figure 14: Simulation of Inhomogeneous FOPA Exhibiting Nonreciprocal Response | This simulation is based on the NLS model (including vacuum noise and higher order idlers creation). (**a**) ZDW profile of 500 m long inhomogeneous HNLF. Fiber ports located at 0 and 500 m are labeled as ports A and B, respectively. Figures (**b**) and (**c**) correspond to signal-pump launched from port A and B, respectively. The color map represents the pump ER (P_{OFF}/P_{ON}) on a decibel scale starting from 0 dB where each step in the contour is of 1 dB. The fiber is assumed to be lossless, and the time window and sample rate were set to 2.56 ns and 51.2 THz, respectively

FOPA response can be approximated as reciprocal, as originally predicted by Marhic [148]. As the input signal power is increased, the directional FOPA performance diverges as expected since signal induced pump depletion also grows. More importantly, the spectral response of the device depends significantly on the launch direction choice.

To quantify it, we introduce the notion of the parametric gate bandwidth, illustrated in Figure 14(b). If we assume that the FOPA is designed as a photon gate, then it is important to define not only the input power necessary to deplete the pump to a target ER value but also the maximal bandwidth that such signal can occupy. The upper limit for the input signal bandwidth can be estimated by simply tuning the CW probe with fixed power and measure the resulting ER. As an illustration, Figure 14(b) shows that a photon gate operated with -24 dBm input and producing over 7 dB ER can accept the signal within 3.1 nm (377 GHz) range. Consequently, FOPA operated in opposite directions shown in Figure 14, (b) and (c), possesses drastically different bandwidth characteristics.

It is important to note that such bandwidth characteristic is still an estimate since it is derived using CW pump and probe. In case when pulsed interaction occurs in inhomogeneous, high-FoM FOPA, the photon exchange will also be limited by incoming signal/pump self- and mutually-induced chirping effects that can alter these estimates. However, if pump is operated in CW regime and the signal power remains low, the CW performance mapping will be reasonably accurate. In case of specific HNLF fluctuation shown in Figure 14(a), this means that a 1 μW signal possessing bandwidth of 3.1 nm (380 GHz) is capable of 50% (3 dB) ER of a Watt-level pump.

Equivalently, this means that ~2.7 ps pulse possessing only 21 photons can induce additional depletion, $P_{OFF} - P_{OFF}/2$, of 412 mW on the pump output power.

Finally, we need to highlight the importance of vacuum noise role in high-FoM FOPA designed to operate in high-depletion regime. While we have emphasized the impact of dispersion fluctuation on distributed mixer performance, we have not attempted to spectrally inhibit its response. In other words, all cases discussed in this report possess a dispersion-defined phase matching intended to maximize gain and depletion effects. Unfortunately, the FOPA design in this case does not impose any restrictions on its bandwidth, allowing for a significant role of amplified vacuum noise (parametric fluorescence). Indeed, Fig. 7 illustrates non-reciprocal FOPA behavior in case when vacuum noise is absent, indicating a qualitatively different transfer characteristics. While such example is also non-physical, it does serve an important message: the fundamental operational limit of high-FoM FOPAs will be reached by

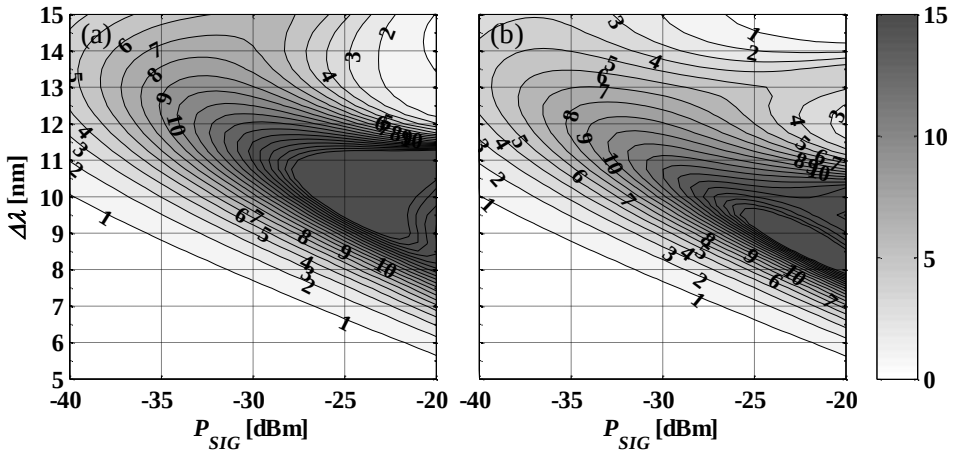

Figure 15: Inhomogeneous FOPA Exhibiting Improved Sensitivity in the Absence of Vacuum Noise | Figures (a) and (b) correspond to Figs. 14(b) and 14(c) respectively. In contrast to Fig. 14, this simulation does not include vacuum noise. The maximal ER was above 40 dB, however, for clarity, contour levels were limited up to 20 dB. The y-axis represents the detuning between the signal and the pump wavelength, $\Delta\lambda = \lambda_{SIG} - \lambda_{PUMP}$, where the 1 W pump was positioned at 1554 nm; and the HNLF global parameters were set as follows: $\gamma = 15$ W^{-1}km^{-1}, $\alpha = 0$, $S = 0.025$ ps km^{-1}nm^{-2} and $L = 500$ m; the HNLF local ZDW profile is described in Fig. 14(a).

investigating both stochastic variations and means for spectral inhibitions in HNLF.

3.5. Conclusions

We have considered the construction of a FOPA with a very high FoM. When operated in saturation, this device is capable of controlling a strong beam using either rapidly varying weak beam or fast pulses containing only few photons. Given a moderate pump, we recognize that such a device can currently be implemented only in a manner of distributed amplification via high confinement fiber and requires strict local phase matching control across hundreds of meters. The local dispersion of conventional HNLF is inherently sensitive to nanoscale variations of the fiber core, and therefore we investigated the performance limit of an inhomogeneous FOPA model.

By performing a statistical study using full NLS model, we showed that the production of a high performance device requires a fiber fabrication process with nanometer scale control. Given the currently available HNLFs it is not possible to efficiently construct a high performance photon gate, as it is likely to produce poor performance. The wide distribution generated by an ensemble of macroscopically identical fibers indicates it is imperative to incorporate knowledge on the HNLF local dispersion to accurately describe photon gate response, and therefore cannot be studied using the homogeneous FOPA model.

This work extends Marhic reciprocity theory. Taking advantage of the distributed nature of parametric process in high FoM FOPAs, we showed for the first time, to best of our knowledge, that an inhomogeneous FOPA possess not reciprocal

transfer function when operated in deep saturation. In fact, a small 4 nm drift of the ZDW across 500 m was sufficient to produce non-reciprocal transfer characteristics. Homogenous fibers in addition to being non-physical are not able to describe this feature of high FoM FOPA. The assumption that fibers are uniform is clearly not a valid approximation for high FoM FOPAs.

HNLF, as a platform, can produce an extremely wide bandwidth photon gate device. The example presented in section 4 demonstrates a device capable of responding to 1 μW input signal occupying bandwidth of 380 GHz. The compatibility of this technology with future data rates makes it interesting as it has the potential to be applied for high speed low power direct light manipulation.

We also recognize the role of vacuum noise in limiting the sensitivity of photon gate. Once the local dispersion will be controlled; further progress may be achieved by spectral inhibition of vacuum noise in order to diminish the total power of parametric fluorescence.

In applications where latency is not critical, areas such as low power switching, sensing, single photon detection, photon counting and more may benefit greatly.

Chapter 3, in part or in full, has been submitted for publication of the material as it may appear in IEEE/OSA Journal of Lightwave Technology, 2014, Ron R. Nissim, Evgeny Myslivets, and Stojan Radic. The dissertation author was the primary investigator, and a primary co-author of this article.

Chapter 4

Enhanced Parametric Interaction via Local Dispersion Engineering

4.1. Introduction

Optical parametric amplifiers (OPAs) have been studied since the sixties, initially in bulk crystals [149] and later in waveguides [150]. One of the OPA numerous advantages [151,95] over conventional optical amplifiers [117,118,119] is its ultrafast response time [151], which originates from the non-resonant optical nonlinearity [64,116]. The parametric effect can be described in terms of frequency conversion of pump photons to signal/idler photons [121], where OPAs with higher efficiency will deliver more pump power to the signal and idler. In fact, a high efficiency (HE) OPA can be saturated using a very weak signal and cause the pump to deplete [29]. The ability of ultrafast, direct manipulation of light using a rapidly varying, weak control beam is of great importance in both science and engineering.

A common way to estimate the efficiency of a parametric amplifier is according to its nonlinear Figure of Merit (FoM), given by the product of the pump power, the amplifier's length L, and its nonlinear coefficient γ [152]. Although high FoM can be achieved using a pulsed pump, it will be beneficial from a standpoint of both energy and practicality to limit the pump to moderate power levels consequently

supporting CW pump operation. In fact, a highly efficient OPA with an increased value of γL product will reduce the power requirement on the pump and will enable new functionalities.

The fabrication of materials and structures which are characterized by high γL product is technologically challenging. The advancement of material science and processing capabilities lead the creation of controlled and high quality structures with improved characteristics. Consequently, optical waveguide technology demonstrated lower propagation lose [153], higher nonlinearities [154], and improved dispersion engineering [155]. A variety of platforms have been studied to date; among the dominant ones are Photonic Crystal Fiber (PCF), chalcogenide, silicon, and silica [11]. PCF platform, although being successful in the visible spectrum, has yet to demonstrate a good fiber that can operate in the telecom band because the design requirements impose a complex fabrication process [30]. When limiting the pump to moderate power levels or alternatively searching for a high γL material, at least currently, the leading platform to explore HE OPA is a high confinement silica fiber, commonly known as Highly Non Linear Fiber (HNLF) [94].

While FoM dictate the gain of an OPA, its operation band is set by dispersion. The dispersion of conventional HNLFs has been studied extensively [104,105,138]. HNLF local dispersion has a strong impact on the OPA behavior. Indeed, due to its relatively high confinement, nanometer–scale variation in the fiber transverse geometry drastically affects its local zero–dispersion wavelength (ZDW) [94]. The perturbations of the HNLF core size along the fiber are caused by finite fabrication tolerances, and translate to ZDW fluctuations along the fiber, effectively making it

inhomogeneous [15]. Various studies have shown that ZDW fluctuations reduce the performance of unsaturated (low FoM) OPA by degradation of its bandwidth (BW), gain, and gain-equalization [105,132].

Given this concern, the affect of fiber inhomogeneity on a high FoM OPA was investigated (Chapter 3). Its two main findings were: 1) High FoM OPAs can have very high performance; unfortunately, however the quality of currently available fibers is not sufficient and significantly reduces the likelihood to observe it experimentally. 2) Remarkably, high FoM OPAs exhibit non-reciprocity. Both findings require attention to the fiber inhomogeneity, which is normally treated as uniform.

At the same time, in spite of the fiber inhomogeneity, when inspecting the distribution of a large ensemble of seemingly identical inhomogeneous fibers, we are able to identify a few members which do provide high performance (Figure 13). This special group contains a variety of members possessing different magnitudes of average core radius variations, which implies the existence of ZDW profiles that are able to positively influence the mixing process. This contradicts the common notion that a uniform fiber, i.e. with a constant ZDW, is the most desirable profile. Although it can be argued that this previously held rule is true for the case of a low FoM OPA, it is not clear whether a certain ZDW profile, i.e. not uniform, would improve the response of a deeply saturated OPA, in particular the effect of signal–induced pump depletion.

The report presents an investigation in which an attempt was made to find a unique dispersion profile. This was done by optimizing the fiber profile showing that non-uniform fibers are able to outperform a uniform fiber in the case of a high FoM

FOPA. We initially provide details on the problem (Section 4.2) and set a benchmark (Section 4.3). Then, various profile optimization methods and their respective results are presented (Section 4.4), and these are followed by conclusions (Section 4.5).

4.2. High Efficiency OPA

Following the introduction we describe a highly efficient (FoM $\gtrsim$ 7) OPA comprised of a weak CW signal coupled to a HNLF pumped by a CW beam. The fiber based OPA (FOPA) under investigation is operated in deep saturation. Operating the FOPA in deep saturation requires positioning the wavelength of the pump in resonance with respect to the fiber dispersion properties. Then, launching a weak signal into the FOPA may induce pump depletion, as schematically illustrated in Figure 12. A practical example can be a FOPA that is pumped by 1 W beam, and have HNLF with a nonlinear coefficient of 20 $W^{-1}km^{-1}$, and a length of 500 m which results in a FoM of 10.

In fact, even in the absence of a signal, a FOPA with a high FoM operated in deep saturation depletes the pump as a result of vacuum noise amplification, i.e. efficient generation of parametric fluorescence [12]. In a case the FoM is low, the FOPA will not be saturated and the output spectrum will show modulation instability (MI) side bands around the pump [134]. As the FoM increases, the MI bands draw more power from the pump, and generate higher orders of MI bands, hence broadening the total BW and increasing the power occupied by noise. After the FoM becomes sufficiently high, the noise will contain a significant portion of the spectral

power and the pump will be depleted. A simulation illustrating the process is shown in Fig. 2(a) and its corresponding trace (Signal OFF) at Fig. 2(b).

The pump of a FOPA of sufficiently high FoM can be further depleted by introducing a weak signal, as shown in Figure 16(b). However, as the FoM increases, so does the total noise power, as shown by Figure 16(c), and therefore the reduction in the pronunciation of the signal–induced pump depletion effect, as shown in Figure

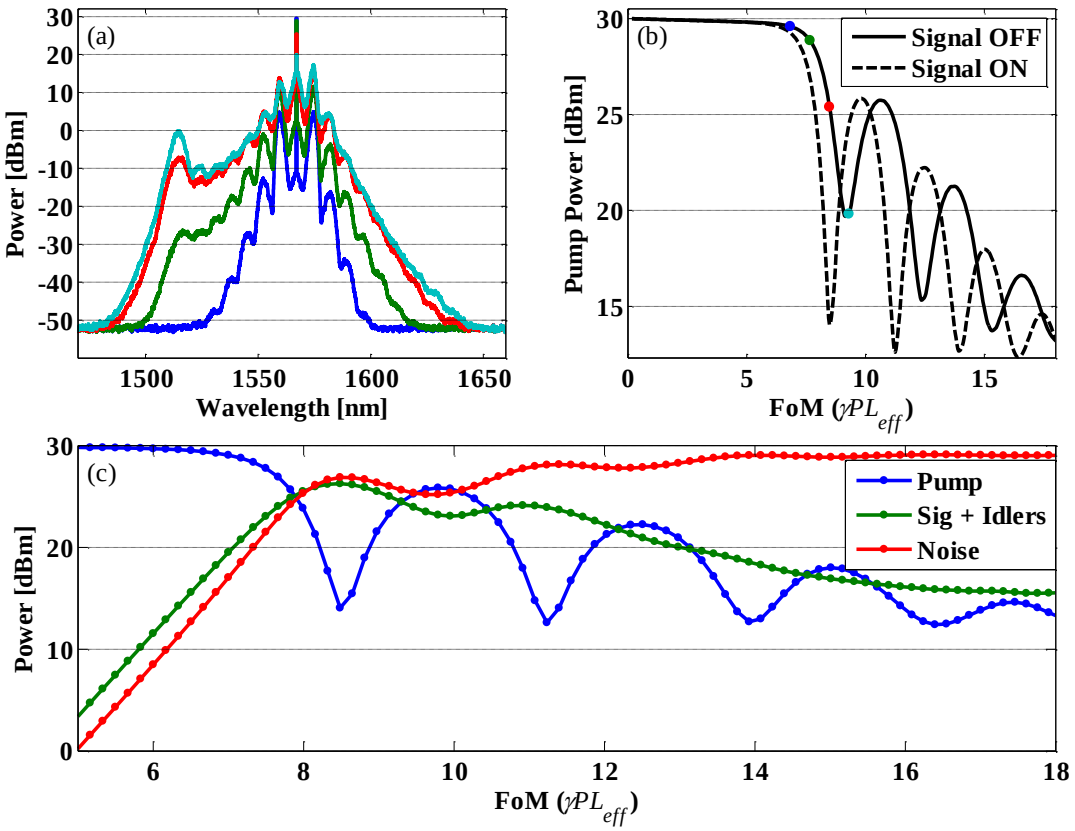

Figure 16: Power Analysis of a Typical Pump Deplition Effect in a Highly Saturaed FOPA | (**a**) The optical spectrum (RBW 50 GHz) at the output of the HNLF in the absence of a signal. Each trace corresponds to the matching color point in (b) (signal OFF), describing the FOPA output spectrum at that point. (**b**) The dependence of the pump power at the output of the amplifier as a function of the FoM in the presence and absence of the input signal using a 50 GHz band pass filter. (**c**) The distribution of the optical power at the output of the HNLF as a function of the FoM in the presence of the signal. The figure shows the power distribution between the pump power, integrated noise power, and the sum of signal and idlers power. The CW components were measured within a 50 GHz BW. The FoM was expressed in terms of the effective length of the fiber, Leff = [1-exp(-αL)]/α, where α is the propagation loss.

16(b). Indeed, each FOPA, depending on its fiber's parameters and input condition, has an optimal FoM which will generate a maximal increase in the pump depletion when a signal is introduced, i.e. maximal signal–induced pump depletion. For clarity we shall make use of the following notations: P denotes the pump power; P_{ON} and P_{OFF} denote the pump output power in the presence and absence of the signal, respectively; The pump depletion represents the ratio between the pump input and output power, $P(0)/P(L)$, where L denotes the length of the amplifier; the signal–induced pump depletion is represented in terms of extinction–ratio (ER), and is calculated according to the ratio of P_{OFF}/P_{ON}.

The amount of pump ER depends on the quality of the parametric interaction. As pump and signal are launched into the FOPA, the system evolves and power is exchanged between the pump, signal, newly generated idler(s), and noise. The quality of this interaction will determine amount of pump ER. The strength of the interaction between various participants also depends on the phase matching of the particular parametric process. For example, the phase matching of the process describing the photon exchange between the pump, signal and 1st order idler is given by the following expression [27],

$$\Delta\beta = k_S + k_I - 2k_P \tag{35}$$

which can be expressed in terms of the ZDW of the HNLF,

$$\Delta\beta = -\frac{2\pi c}{\lambda_P^{\,2}} S(\lambda_P - \lambda_0)(\lambda_S - \lambda_P)^2 . \tag{36}$$

Subscripts P, S, I, and 0 denote the pump, signal, idler, and zero–dispersion, respectively. S denotes the dispersion slope at the ZDW, and λ and k denote the

wavelength and wave–vector respectively. Along the fiber, changes in its transverse geometry generate *local* ZDW. Therefore, according to (36), the phase matching acquires spatial dependence which will consequently affect the parametric process. In practice, for a system which is not spectrally inhibited, a FOPA with good ER will tend to generate many idlers and have a wide (noise) BW. This will result in many simultaneous processes, including mixing between different spectral components of the noise, and will not be practical to trace each individually.

Consequently this complicates the search for a unique dispersion profile as one cannot simply rely on enhancing a specific process. By using the standard NLSE, it is possible to account all aforementioned parametric interactions simultaneously [13]. The equation can be expressed in the following scalar compact form,

$$\frac{dA}{dz} = (\hat{D}(z) + \hat{N} - \frac{\alpha}{2})A, \tag{37}$$

where the dispersion has a spatial dependence to account for the fiber inhomogeneity. The fiber characteristics were described using the following parameters: ZDW profile $\lambda_0(z)$, dispersion slope S, propagation loss α, nonlinear coefficient γ, and length L. Indeed, it is possible to consider higher dispersion–orders terms; however, they were neglected for simplicity.

During the search for a unique ZDW profile various profiles were simulated. Each profile under test was divided and simulated as a collection of many short uniform segments. The length of each segment was set to correspond a 0.005 nm average shift in the ZDW with respect to its adjacent segments but was limited to no shorter than 1% of L_{NL} where $L_{NL} = (\gamma P(0))^{-1}$. As implied by [142], in a FOPA which

is driven using CW fields, the ZDW variations are effectively averaged on length scales which are much shorter than L_{NL}, which can be treated as a uniform segment. Once the optimizer was done maximizing the ER, the solution, i.e. the optimized ZDW profile, was validated. In the validation process, the optimized profile was simulated multiple times using different segment sizes and ensured the ER converges to the declared value as the segment size becomes shorter.

Another type of uncertainty concerning the validity of the solution originates from vacuum noise. The simulated ER is influenced by the noise field realization at the input. Namely, various noise realizations will generate different values of ER. The uncertainty of the ER is inversely related to the length of the simulation time–window. As a result of averaging, a longer time–window will reduce any uncertainty associated with the noise realization. As part of the validation process, the performance level was guaranteed by performing multiple simulations using random noise seeds to quantify the level of uncertainty in the calculated ER due to noise.

It's important to bear in mind that the reported performance of a FOPA with good ER, is limited by the BW of the optical filter at the receiver; then, introducing the signal will tend to bring the pump closer to the (amplified) noise floor. Consequently the simulated value of P_{ON} will be limited by the optical BW. For example, narrowing the BW will reduce the amount of integrated noise power reaching the detector and vice versa, therefore affecting both the ER and the noise performance. In this report the investigation focused on the static (CW) response of the amplifier and the pump detection was simulated using a 50 GHz optical filter followed by a power meter.

4.3. The Optimization Criterion

The question of whether a high FoM inhomogeneous FOPA can outperform a homogenous one requires establishing a benchmark. This was done by optimizing FOPA based on uniform fiber model which resulted in an ultimate performance limit and will be used in the next section, both for comparison and as a starting point to find an optimal fiber profile.

Initially the parameters of a high FoM *homogenous* FOPA were optimized using realistic HNLF values [94] to provide the highest possible ER that can be reached using this type of fiber model. Following the optimization, if the signal wavelength will be detuned from its optimal value the ER will decrease, thus enabling an estimate of the BW of the device. In a similar manner, one can have such a discussion about the stability of the optimal solution to other parameters. The goal then is to find an upper bound to the ER, a so–called performance budget from which any parameter deviation causes a reduction.

When declaring a benchmark it is important to state the value of certain parameters to create a common ground for future comparisons. In the framework of an ideal three wave model [27], the problem of depleting the pump is reduced to three parameters: normalized phase matching, FoM, and the ratio between the pump power and the signal power, from which the ER can be calculated [28] (Section 3.2). Therefore, when defining the benchmark level, in addition to declaring the signal input power and the maximized ER, it is necessary to declare the pump input power. As indicated by the three wave model, for a given FoM and signal input power, it would

be easier to saturate (deplete) a weaker rather than a stronger pump. For this report the pump and signal powers were set to 30 dBm and -35 dBm, respectively, and will remain as such for the entire report.

After setting the system power levels, the remaining FOPA parameters were optimized. The optimization was made within the normal working range of the HNLF parameters: $L \sim 500$ m, $10 < \gamma < 30$ $W^{-1}km^{-1}$, $0.5 < \alpha < 1.0$ dB/km, and $0.03 < S < 0.05$ ps/(nm^2 km). λ_0 was set to 1550 nm, where λ_S and λ_P were treated as free parameters. The FOPA modeling was done using an NLSE [13], injected vacuum noise was included [131], and the model was solved using the split-step algorithm [13]. Matlab optimization toolbox was used to perform the optimization using the conventional simplex algorithm [146]. An initial guess was provided to the optimizer: The fiber parameters were set to the middle values of the normal working range, where the initial signal and pump wavelengths were set to $\lambda_P = \lambda_0 + 10$ nm and $\lambda_S = \lambda_P + 10$ nm.

The optimization yielded an intermediate solution of 500 m long fiber which in principle corresponded to the location of the ER's "first peak" (FP), as illustrated at Figure 16(b). The length of the fiber was then prolonged (swept) to find the corresponding position of the second peak which provided a higher ER. The parameters of the system were then loaded as an initial guess for a second round of optimization, to ultimately yield a maximized ER of 12.88 dB for the following set of values: $\gamma = 17.66$ $W^{-1}km^{-1}$, $L = 672.3$ m, $\alpha = 0.69$ dB/km, $S = 44.89 \times 10^{-3}$ ps/(nm^2 km), $\lambda_P - \lambda_0 = 17.06$ nm, $\lambda_S - \lambda_P = 6.11$ nm. This level of ER and its corresponding parameters of system serve as the benchmark and will be compared against that of an *inhomogeneous* FOPA.

4.4. Unique ZDW Profile

This section describes a search for a unique dispersion profile; during which the fiber's parameters: α, S, and γ remained set to the corresponding values of the benchmark. Thus ensuring the fiber remains of the same type while the ZDW (global and local) is being modified. Regarding the length of the fiber, the FoM of the benchmark is relatively high (11.26) which makes it computationally expensive to work with. Therefore, the length of the fiber was shortened (swept) in order to locate the ER's FP. It was found at fiber length of 507.5 m, provides an ER of 11.64 dB and corresponds to a FoM of 8.62. In general, the higher the FoM, the longer the time it takes to simulate the system. Due to limited computational power, one profile optimization was made using a fiber length corresponding to the benchmark (672.3 m) while all others were made based on the length corresponding to the FP (507.5 m).

During the search for an optimal fiber profile, it may be necessary to reposition the pump and signal wavelengths. By fixing the pump wavelength to have it serves as a reference for the signal wavelength and the ZDW profile, insignificant wavelengths drift were prevented during the optimization process. The other parameters of the system, excluding L, were set according to the benchmark and the optimization algorithm remained the same as described in Section 4.3. The following subsections will each describes the ZDW profile representation, the initial guess, and the associated optimization result.

4.4.1. Static Grid Representation

In the following description, the ZDW profile of the fiber was represented by six equally spaced nodes, as illustrated by Figure 17. The ZDW profile was defined by interpolation of the nodes using piecewise–cubic method. This interpolation method kept the profile smooth and monotonous between each of the neighboring nodes, with no over–shoot.

In the first profile optimization of the static grid, the benchmark settings were used as the initial guess that was provided to the optimizer. Namely, the signal wavelength was set such that λ_S - λ_P = 6.11 nm, L = 672.3 m, and each of the six nodes was positioned at wavelength 1550 nm. The optimization yielded a maximized ER of 13.31 dB (6-Benchmark) with its associated profile shown in Figure 18. Afterwards a similar optimization was made where the FP settings were used as the initial guess, namely L was set to 507.5 m. This optimization resulted in ER of 17.75 dB (6-First

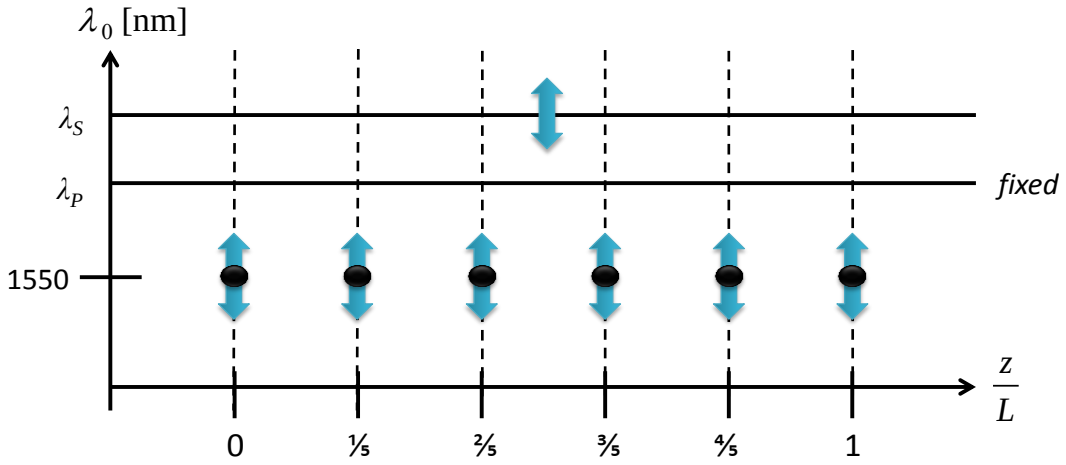

Figure 17: Representation of the ZDW Profile: Static Grid | Illustration of ZDW profile representation of a fiber using "static grid". The profile is represented by six equally spaced nodes where the first and last nodes are positioned at the entrance and exit of the fiber, respectively. The full profile description is given by interpolating the ZDW between the nodes. Each of the double headed arrows represents a degree of freedom. The signal wavelength (λ_S) remains a free parameter, and a reference is formed by keeping the pump wavelength (λ_P) fixed.

peak) with its associated profile presented in Figure 18.

The finite number of nodes previously described was chosen somewhat arbitrarily; additionally, the grid is equally spaced and fixed. It is then plausible that the optimal solution attained under those constraints is in fact an approximation of a more successful solution. Therefore the number of nodes (degrees of freedom) was increased to ten (eleven) which was then used to optimize the profile. The grid was made in a similar manner to that presented in Figure 17, using spacing of $L/9$. Also, in order to gain access to new possible solutions, the number of nodes was chosen such that the grid will be displaced relative to the six nodes grid. The initial guess of the optimizer was set to be an interpolation of the latter solution. The ten nodes optimization resulted in an ER of 19.18 dB (10-First peak) with its associated profile also presented in Figure 18.

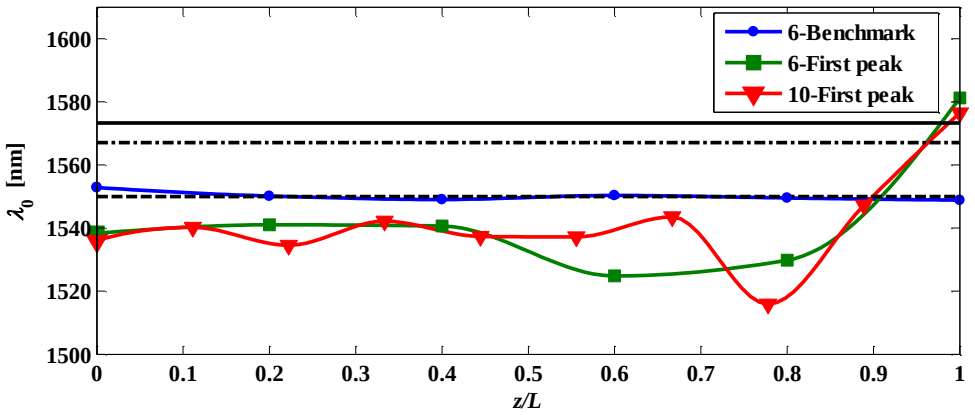

Figure 18: Optimized Dispersion Profiles on a Static Grid | A plot of the optimized ZDW profiles. The dashed line shows the profile of the benchmark. The blue trace (round markers) and green trace (square markers) describe solutions which were made using the six nodes static grid profile representation in the case that the initial guess of the optimizer was set as the benchmark and first peak settings, respectively. The red trace (triangular markers) describes a solution which was made using the ten nodes static grid profile representation in the case that the initial guess of the optimizer was set as the green trace. The markers represent of the nodes while traces shows the interpolated profile. The pump (dash-dot) and the signal (solid) positions are described by the two uppermost horizontal lines. The optimizations resulted in a practically identical signal wavelength.

Better solution may exist: The usage of a fixed grid representation confines the solution of the optimizer to a continuous profile and of a specific predetermined length. It is possible that an optimal solution may include discontinuities in the ZDW profile with a corresponding optimal length, as it is likely to depend on the shape of the profile. Such a solution will be effectively described by concatenation of two or more fibers.

4.4.2. Dynamic Grid with Variable Fiber Length

In this subsection, the profile optimization was done on a dynamic grid. This profile was described using six nodes as before, only in this section their spatial location was considered a variable. Only the first node was spatially fixed since it indicates the beginning of the fiber. This type of representation has a total of 12

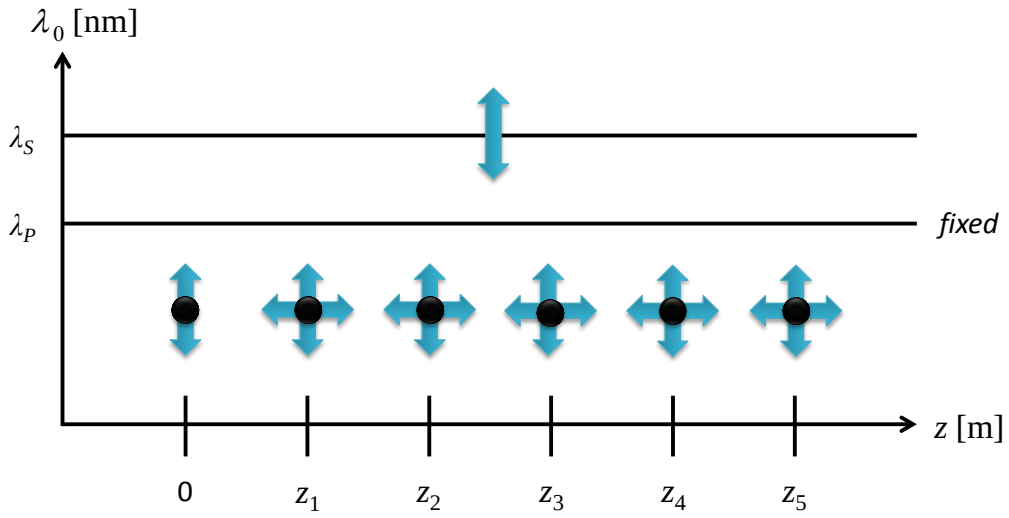

Figure 19: Representation of the ZDW Profile: Dynamic Grid | Illustration of ZDW profile representation of a fiber using "dynamic grid". The profile is represented by six nodes where the first and last nodes are positioned at the entrance and exit of the fiber, respectively. Each of the nodes, except the first one which is positioned at the entrance of the fiber, is free to be shifted both laterally and vertically. The full profile description is given by interpolating the ZDW nodes. The position of the signal (λ_S) remains a free parameter; however, the wavelength of the pump (λ_P) is fixed and acts as a reference.

parameters to optimize. In addition to being able to simulate a bigger variety of curves in comparison to the previous representation, the length of the fiber was also a variable. An illustration of the dynamic grid structure is shown in Figure 19.

Two optimization attempts were made using this profile representation. In the first case, the initial guess of the optimizer was set to the fixed grid six node solution (6-First peak); whereas in the second case the initial guess was set as FP. This resulted in an ER of 19.65 dB (6 nodes – FP) and 18.29 dB (FP), respectively. Their associated profiles are shown in Figure 20.

The latter result effectively reduced the solution from six to four nodes, thus simplifying and smoothing the solution while keeping a relatively high level of performance. The former result, in comparison to the ten node solution, was able to achieve a similar ER level while having a relatively different profile.

The optimized profiles have demonstrated a rapid change in the ZDW at the

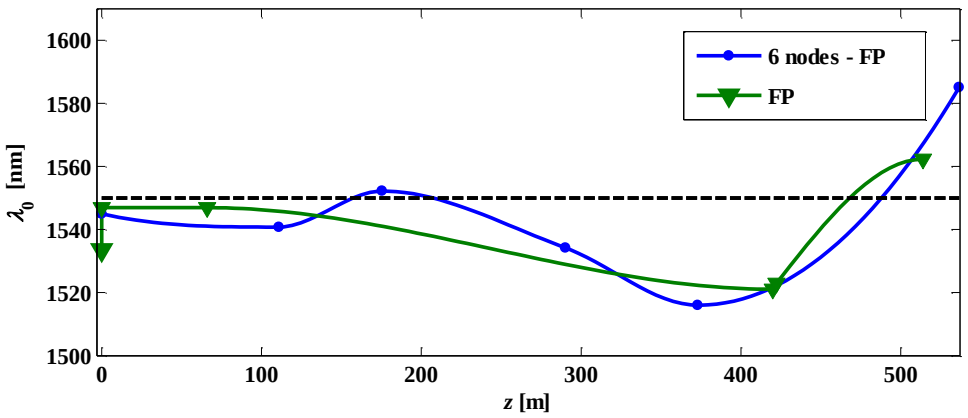

Figure 20: Optimized Dispersion Profiles on a Dynamic Grid | The dashed line shows the profile of the benchmark. The upper horizontal line (dash-dot) represents the wavelength of the pump. The green trace (triangular markers) describes a solution made by a dynamic grid representation in the case that the initial guess of the optimizer was set as FP. The blue trace (round markers) describes a solution made by optimizing a dynamic grid in the case that the initial guess of the optimizer was set to the solution achieved by the six node static grid (6-First peak). Each of the markers represents a node.

last 100 m of the fiber, a distance which corresponds to approximately twice L_{NL} (L_{NL} = 57 m). Such fast changes tend to average; therefore it is plausible a simpler solution may be found in the form of discontinuity. Additionally, if one would attempt to generate such a profile by applying a varying tension across the fiber [105], a slowly varying profile would be considered more desirable.

4.5. Bandwidth Analysis

Deeply saturated FOPA exhibit a tradeoff between the pump's ER and the BW of the effect [27]. This created an interest to know whether the enhancement of the ER shown by the optimized profiles came at the expense of the BW of the effect. This was investigated by simulating the dependence of the ER on the signal wavelength. As the signal detune from the optimal position the pump's ER will decrease; thus providing a measure to the BW of the signal induced pump depletion effect. Figure 21 shows the results of such analysis.

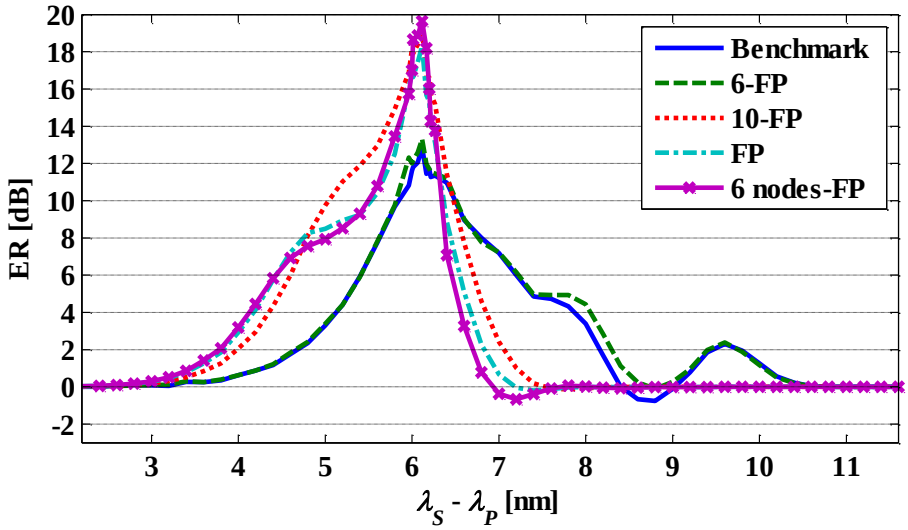

Figure 21: Bandwidth of Dispersion Optimized Mixers | A simulation of the pump's ER dependence on the signal wavelength for different optimized ZDW profiles; the signal position is shown with respect to the pump wavelength.

It is clearly shown, that the BW of the effect was not compromised. In fact for a given ER level of 10 dB the BW broadened from 0.65 nm (Benchmark) to 1.44 nm (10-FP). Even though the accuracy of this estimation is coarse, it indicates the optimized solution can perform well above unphysical uniform fiber model and that opportunities lay in the inhomogeneous fiber model.

4.6. Noise Properties

The optimizer interacts with the simulator by running the simulation repeatedly using a different settings each time to eventually maximize the ER. The same noise realization was used during the simulations in order to assist the optimizer to converge to a solution. For each of the reported solutions a certain level of ER was stated; in practice the pump output power has a certain mean and variance levels. For each of the solutions – i.e. optimized profiles – a histogram was generated using random noise realizations. Each of the histograms consisted of 300 samples. The simulations were performed using a time–window of 2^9/(150 GHz), and a sampling–rate of 2^8×(150 GHz). Table 1 shows a summary of the noise performance of the main solutions.

Table 4: Summary of the optimized FOPA performance

Case	P_{ON} (mW)	P_{OFF} (mW)	ER (lin.)
Benchmark (672.31 m)	18.78 ± 1.59	259.5 ± 6.3	13.92 ± 1.24
6-FP	10.58 ± 1.27	450.9 ± 10.2	43.23 ± 5.37
10-FP	7.77 ± 1.09	435.04 ± 9.45	57.12 ± 8.27
Dynamic grid (FP)	9.41 ± 1.16	433.03 ± 10.3	46.74 ± 6.06
Dynamic grid (6 nodes – FP)	5.65 ± 0.65	359.36 ± 9.57	64.51 ± 8.00

The results remain sufficiently stable to distinguish between the qualities of different solutions. In comparison to the benchmark, the optimized profiles keep the pump less depleted in the absence of a signal and more depleted in the presence of it, thus achieving better ER. Additional improvement in the ER can be made in exchange to reducing the BW of the filter which will lower P_{ON}.

4.7. Conclusions

Deeply saturated high FoM FOPA exhibit a highly sensitive signal–induced pump depletion effect. This report explored the use of local dispersion to enhance the effect and challenged the conception that a longitudinally uniform fiber is the most desirable structure. In fact, optical fibers are commonly treated in the literature as a longitudinally homogenous medium. Previous studies showed that such approximation is not valid for HNLF based FOPA, and even more so for those operating in deep saturation.

The investigation initiated by posing a question of whether a high FoM FOPA which is based on inhomogeneous fiber can have a higher ER in comparison to homogenous one, assuming both fibers are of the same type. A benchmark based on the homogenous FOPA model was established by optimizing the parameters of the system and resulted in an ER of 12.88 dB, effectively posing an upper limit to the achievable ER using this model. The ER levels which were achieved afterward, using the inhomogeneous fiber model, resulted in significant improvement of several decibels, demonstrating ER levels which can only be accounted by an inhomogeneous FOPA model.

As this is the first study on the enhancement of signal–induced pump depletion of high FoM FOPA using local dispersion engineering, it is emphasized on maximizing the pump ER. Future reports may include a broader search with constraints on the profile simplicity, the BW of the effect, performance stability to profile perturbations, and noise performance, to name a few. New profile solutions may be found through the development of the optimizer, e.g. the type of optimization algorithm, fiber representation (degrees of freedom), initial guess (basin of attraction), and the affect of noise which is averaged to a degree within the limits of the available computational power. Modification of these factors could lead to additional solutions.

This work has showed, with regards to deeply saturated FOPAs, that opportunities are available if one is able to abandon the uniform fiber model. Practical FOPA designs may use heterogeneous fibers and include higher–order dispersion, all together provide access to a greater inventory of fibers and will lead to new capabilities.

Chapter 4, in part or in full, has been submitted for publication of the material as it may appear in OSA Optics Express, 2014, Ron R. Nissim, and Stojan Radic. The dissertation author was the primary investigator, and the primary author of this article.

Chapter 5

Low Power Fast Control of Fiber-Optics Parametric Amplifiers

5.1. Introduction

Fiber-optic parametric amplification has been a fruitful research topic in the past two decades and has led to diverse and remarkable experimental demonstrations, including: sampling oscilloscope [156], wide-band amplifiers [157], low-noise amplifiers [158], regeneration [126], long-range wavelength conversion [130], signal processing [159], and frequency comb generation [160]. These successful results all share a key component – a Highly Nonlinear Fiber (HNLF).

This type of fiber was initially introduced in the literature at [93] and has since been gradually maturing to provide high performance [99]. HNLF is in fact a GeO_2 highly doped silica fiber which takes advantage of the high mode-confinement to reduce the mode size in order to generate higher light intensities for a given power level. This, along with its low dispersion and low loss, results in light propagation in a fiber with predominant nonlinear parameter γ compared to standard single mode fibers. Yet, when compared to alternative platforms, HNLF nonlinear parameter is considered to be low [99]. This relative deficiency is more than compensated for – primarily by HNLF unparalleled transparency in the telecommunication band, which

in combination with its highly controlled low dispersion, allows for a long interaction length [95], [11]. Originally, the future of HNLF as a practical platform was questioned, as it was believed that stimulated Brillouin scattering (SBS) would inhibit their use [96]. Since then, effective methods for raising the SBS threshold have been developed [97]. It is currently accepted that the main limitation of HNLF-based parametric amplification is inherent molecular scale fluctuation of fiber core size caused by finite fabrication control [95].

Recent studies have highlighted potential use of HNLF for investigating a new class of parametric amplifier (FOPA), which has the potential to both reduce the power requirement on the pump and to enable new functionalities. The concept relies on FOPA operation in the deeply saturated regime, in which the pump can be controlled using an extremely weak, rapidly varying signal, as was originally demonstrated by Andrekson [29]. In this topology, the signal input power acts as a control knob on the pump output power; owing to its resemblances with an electronic gate, photon gate and deeply saturated FOPA will be used interchangeably. Indeed, it was shown that such a photon gate device has the potential to have broadband operation of several hundred gigahertz at few photons level while producing a substantial pump response of several decibels [161], [162]. Interestingly, a deeply saturated FOPA also shows non-reciprocal behavior. Photon gate high performance and its non-reciprocity are related to each other, as both critically depend on the HNLF's local structure (Chapter 3).

The construction of deeply saturated FOPAs, particularly of moderate pump power, depends on the medium characteristics. The Figure of Merit (FoM) of

parametric amplifiers, given by the product of the pump power P, the amplifier length L and nonlinear parameter γ, provides a simple measure of the amplifier's performance. Deeply saturated FOPAs have high FoM ($\gamma PL > 7$) (Chapter 3, Figure 11): By using a sufficiently high γL material, the pump power may be kept at a sub-Watt power level and promote device operation using conventional laser diodes. Ideally, one could simply use a nearly lossless HNLF to construct an arbitrarily long amplifier to reach any performance level.

The performance of photon gate was numerically studied using an *inhomogeneous* FOPA model (Chapter 3). Although it is a common practice to model physical fibers as a uniform entity, the study showed that fiber non-uniformity dictates photon gate performance. Moreover, it identifies saturated FOPAs as distributed amplification devices which, assuming moderate pump power level, require the ability to rigorously maintain *local* dispersion across hundreds of meters. Evidently, both photon gate and its non-reciprocal behavior require attention to the fibers inhomogeneous nature. In fact, a perfectly uniform fiber lacks the required spatial symmetry breaking needed for non-reciprocal behavior, in which case a light field will experience identical evolution whether it propagates in the forward or backward direction of the fiber. Additional numerical evidence for the importance of FOPA inhomogeneous nature to photon gate performance is found in Chapter 4.

Here we extend previous work, by experimentally studying non-reciprocity in a deeply saturated FOPA. We present a simple manifestation of FOPA non-reciprocity and for the first time, to the best of our knowledge, show clear evidence to the connection between FOPA behavior under deep saturation and its inhomogeneity. In

fact, results indicate non-reciprocity is indeed driven by dispersion rather than polarization. Moreover, we present a simulation strategy for photon gate – a necessary ability needed for the advancement of high FoM FOPAs.

This report is organized as follows: The next section describes the parametric fluorescence of a deeply saturated FOPA and demonstrates that its spectral shape depends on the orientation (i.e. forward or backward direction) of the HNLF. In the absence of a signal, this is the simplest manifestation of FOPA non-reciprocal behavior. Equally important, Section 5.2 shows that the spectral shape is dominated by core size variation rather than birefringence. In Section 5.3, a weak continuous wave (CW) signal is launched into the deeply saturated FOPA. The system is excited at different signal input conditions and the pump response is measured. As in Section 5.2, the pump response depends on the orientation of the fiber. In both sections, the scalar (polarization-independent) inhomogeneous FOPA model was sufficient to successfully explain the experimental results.

5.2. Parametric Fluorescence of Deeply Saturated FOPA

A CW pump launched into a fiber in the anomalous dispersion regime may generate a wideband parametric fluorescence (Figure 10) by amplifying vacuum noise [131]. This process is complex and occurs in cascade. Initially, the pump generates modulation instability (MI) [13]. During the MI process, pairs of pump photons convert into pairs of signal and idler photons at frequencies satisfying energy

conservation. In the absence of an input signal, the process will be seeded by vacuum noise and the converted photons will populate the spectral region of the MI gain profile in the vicinity of the pump effectively generating first order MI bands around the pump (Figure 22(a)). The MI gain profile is set by both the fiber and the pump properties; where higher product of γP will generate a stronger peak gain and a broader gain bandwidth. The latter can also be promoted by using a lower anomalous dispersion.

For a given fiber length, an increase in the pump power saturates the amplifier, that is, it generates stronger first order MI bands which will mix with the pump to efficiently generate higher order bands (Figure 22(b)). (Alternatively, a similar result can be generated by increasing the fiber's length or nonlinearity.) In this case, similar to the MI process, the first order bands act as degenerate pumps and the original CW pump will act as a signal to generate second order (idler) bands using the four wave

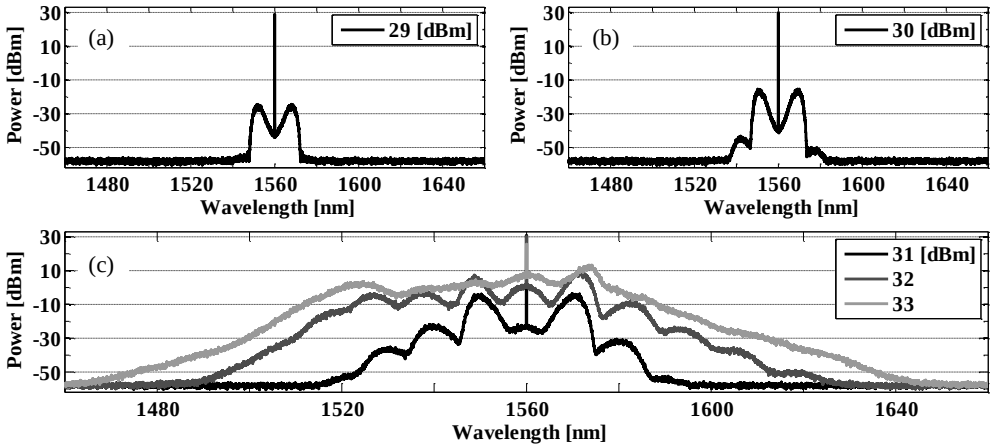

Figure 22: Generation of Parametric Fluorescence in a Cascading Manner Using a Highly Nonlinear Fiber Seeded by a CW Pump | This process relies on four-wave mixing and modulation instability. Figures (a), (b), and (c) show the optical spectrum at the output of a fiber at various input power levels, at a resolution bandwidth of 12.5 GHz. The pump input power is stated in the legend for each figure. The pump output power at Figs. (a) and (b) is 28.9 and 29.9 dBm, respectively; at Fig. (c), the pump output power is 30.8, 30.2, and 25.7 dBm – corresponding to input power levels of 31, 32, and 33 dBm.

mixing effect. Thus, in a cascading manner, additional higher order bands are created. Proceeding further, in a FOPA with a sufficiently high γPL, amplifying vacuum noise leads to saturation and eventually pump-depletion (Figure 22(c)). The simulation shown in Figure 22 is generated using the nonlinear Schrodinger (NLS) model [13] with the following parameters: λ_P = 1560 nm, γ = 13 (W km)$^{-1}$, λ_0 = 1550 nm, S = 0.04 ps/(nm^2 km), α = 0.2 dB/km, and L = 0.4 km, and it includes seeded vacuum noise. Parameters λ_P, λ_0, S, and α represent the pump wavelength, the fiber's zero-dispersion wavelength (ZDW), dispersion slope, and propagation loss.

The broadband amplified vacuum noise is created in a cascaded (distributed) manner. Consequently, the spectral shape of the amplified vacuum noise at the output of the fiber depends on the input condition (pump's power and wavelength) and the fiber's *local* properties. In physical terms, the fiber core experiences geometrical changes along the fiber which may locally affect birefringence and zero-dispersion-wavelength (ZDW). While in recent years [105], [163], [108] methods to handle local ZDW were demonstrated, in the context of fiber-based parametric amplification, a successful experimental approach for local birefringence has not yet been developed. Therefore it is critical to identify which of these two is dominating the parametric process.

FOPA reciprocity theory which holds under the three-wave, undepleted pump approximation, asserts FOPA's reciprocal behavior specifically in the presence of local birefringence and core size variation [148]. In contrast to an unsaturated FOPA, this approximation is broken in photon gate as a result of its high FoM. Indeed, even in the absence of an input signal, a significant amount of amplified vacuum noise is

generated by drawing power from the pump which significantly depletes it. Consequently, this work extends FOPA reciprocity theory by studying FOPA behavior in the pump depleted regime.

In the following experiment a quasi CW pump is launched into a HNLF while monitoring its output using an optical spectrum analyzer (OSA). The quasi CW pump has a repetition rate of 20 MHz and pulse width of 1 ns; it is created by externally modulating the amplitude of a tunable laser source using a pattern generator driven by a 10 GHz RF clock; subsequently, the modulated light is amplified using an EDFA and its power level is set using a variable optical attenuator prior to the HNLF. The suppression of SBS was validated by measuring the optical spectrum of the back reflected light from the HNLF to ensure SBS tone was weaker than Rayleigh scattering for the power levels used in this work. Therefore, SBS can safely be neglected. Although SBS suppression improves with reduction in the pulse temporal width, its duration cannot be arbitrarily short because the goal is to measure the static response of the system; therefore the pulse duration should be sufficiently long to resemble a CW behavior, in which case no additional phase matching limitation associated with nonlinear pulse propagation will exist [164]. This condition will be validated a-posteriori by showing that the measured response time of photon gate is much shorter than the duration of the quasi CW pump. A schematic description of the experimental setup is shown in Figure 23(a).

During the experiment it was evident that the spectral shape of the parametric fluorescence depends on the input state of polarization (SOP) of the pump. Therefore a motorized polarization controller is placed before the HNLF to average out the

dependence of the pump SOP from the OSA trace (Figure 23(a)). The optical spectrum is measured for both orientations using an average input pump power level of 14.6 dBm: In the first measurement the pump is launched in the "forward" direction and afterwards the measurement is repeated in the "backward" orientation, by swapping the HNLF's ports (Figure 23(b)).

For each fiber orientation three traces are displayed. During the measurement, the ratio between the polarization scrambling rate and the OSA scanning rate is sufficiently low to enable the OSA to capture an optical spectrum generated by a nearly constant pump SOP during a single sweep. By capturing many traces, it is possible to establish the *range* in which each spectral component is varying. Traces "max" and "min" describe the upper and lower bound of this range, respectively. Trace "average" on the other hand is created by averaging many traces. The measurement of the average optical spectrum trace was validated by a repeated measurement in which the polarization controller was replaced with a piezo based scrambler, which operates at kilohertz rates. The OSA sweep time was then slowed to enable the scrambling rate of the pump SOP to be significantly faster than it; consequently, each sample on the OSA trace represents an average value.

It is evident that the optical spectrum of the parametric fluorescence is distinctive and depends on the orientation of the HNLF. Moreover, it is not possible to compensate the difference between them by manipulating the SOP of the pump. Therefore, this non-reciprocal behavior is solely attributed to the combination of the fiber's inhomogeneous nature and the high FoM FOPA. Indeed, if the FOPA had a low FoM these traces would overlap, regardless of the fiber inhomogeneity.

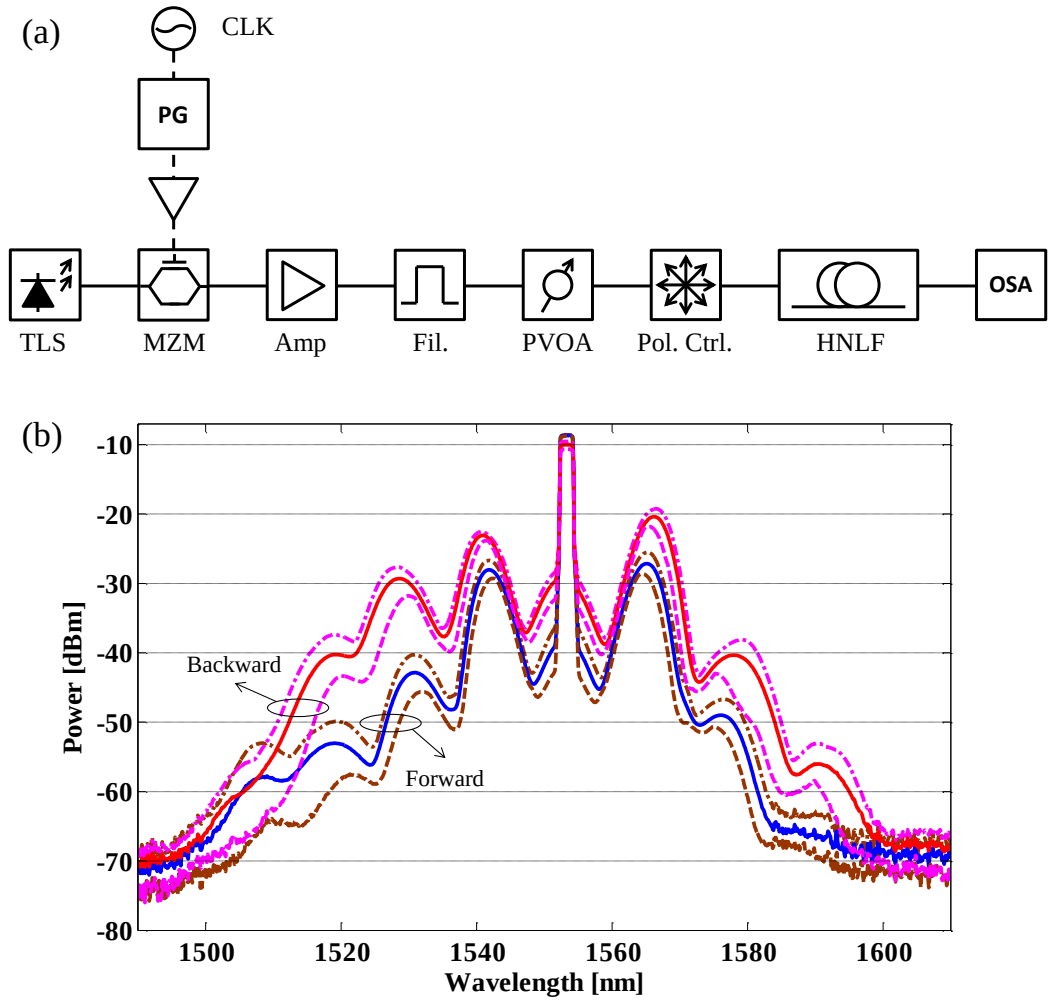

Figure 23: Simple Manifestation of FOPA Non Reciprocal Behavior in the Form of Parametric Fluorescence Created by a Quasi-CW Pump | (**a**) Experimental setup: CW tunable laser source (TLS), Mach-Zehnder modulator (MZM), pattern generator (PG), 10GHz RF clock (CLK), erbium doped fiber amplifier (Amp), optical filters (Fil.), programmable variable optical attenuator (PVOA), and polarization controller (Pol. Ctrl.). Optical filtering is applied to eliminate amplified spontaneous emission (ASE) and pump residues from the amplifier. The HNLF output is connected to an OSA using the 1% port of a 20 dB coupler (not shown). The performance of the setup is monitored to ensure the stability of the quasi CW pump (not shown). (**b**) The pump's input polarization state influences the optical spectrum at the output of the HNLF, measured at a resolution bandwidth of 2 nm. The solid, dashed, and dot-dashed traces represent a measurement of the average, min, and max power levels, respectively, when sweeping the pump's SOP.

Interestingly, the result in Figure 23 can be simulated using a scalar inhomogeneous FOPA model. Using the counter-colliding method [163], we attained the local ZDW profile of the fiber (Figure 24) and subsequently incorporated it into

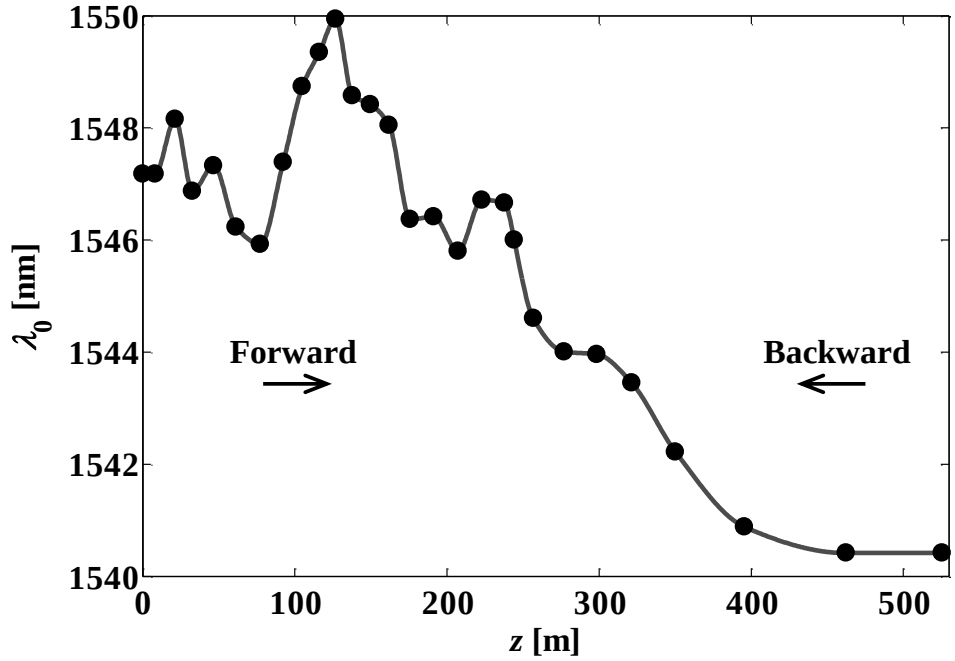

Figure 24: The Zero Dispersion Wavelength Profile of the Fiber | The fiber length is 525 m, with a propagation loss of 1.27 dB/km, spliced at 245.2 m with 0.27 dB splice loss, and an average dispersion slope of 0.025 ps/nm^2/km.

the simulation. The spectral profile of the wideband parametric fluorescence, generated by a high FoM FOPA, is highly sensitive to the system's parameters – global and local. Given the local information, the wideband spectral profiles may be used to calibrate the following parameters of the system: pump power, dispersion (including higher orders), and fiber nonlinearity. The calibration process optimizes these parameters to numerically produce the measured optical spectrum shown in Figure 23. Thus, this unique, rich spectral content can be used to extract information on the associated fiber. The other parameters of the system were predetermined and remained fixed in the calibration process: fiber length, propagation loss, splice loss, and, most importantly, ZDW profile. This process is done using the Simplex method

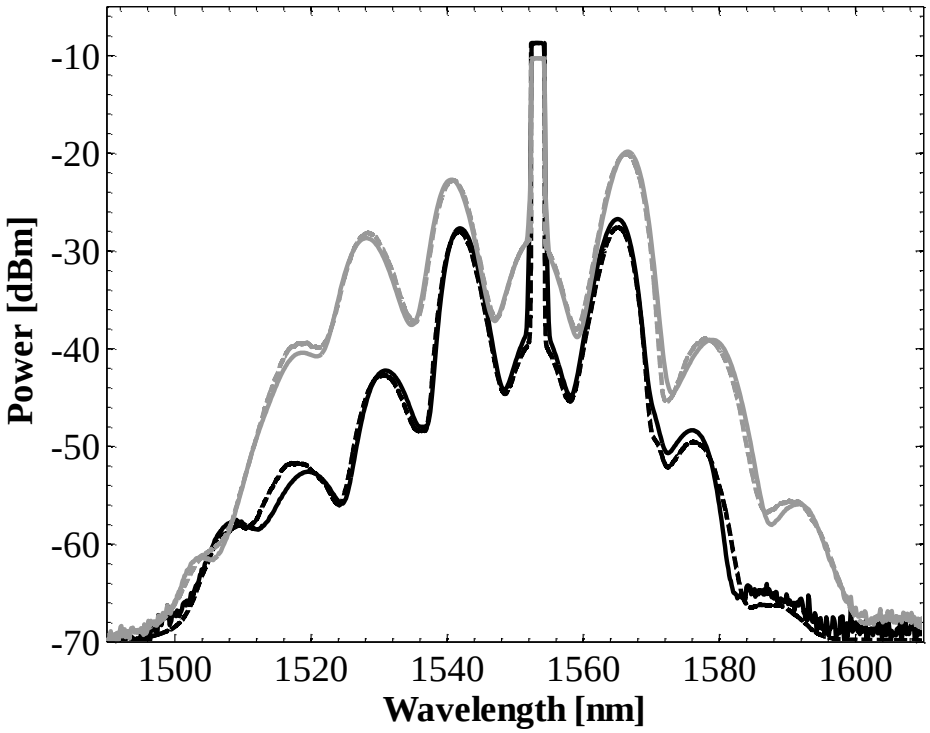

Figure 25: Simulated Optical Spectrum at the Output of the Fiber in Both Orientations | The solid traces correspond to the measurement of the polarization averaged optical spectrum from Fig. Figure 23(b). The simulated (dashed) traces are the result of the calibration process. The black and gray traces represent forward and backward orientation, respectively. This calucaltion is done using a scalar NLS model.

[146] under constraints for: pump peak power ($31 < \bar{P} < 32.7$ dBm), nonlinearity ($10 < \gamma < 15$ $W^{-1}km^{-1}$), slope ($20 < S < 50$ s/m^3), slope derivative ($-7e8 < S' < 9e8$ s/m^4), and dispersion ($-40e\text{-}9 < D < 80e\text{-}9$ s/m^2). Although the input peak power is nominally identical, the optimization allowed for a power difference between the input peak power of the forward and backward pump to account for uncertainties associated with fiber coupling ($-0.7 < \delta P < 0$ dB). The outcome of the calibration process is shown in Figure 25 and resulted in the following parameters: $\bar{P} = 31.13$ dBm, $\delta P = -0.53$ dB, $\gamma = 12.88$ $(W\,km)^{-1}$, $S = 24.12$ s/m^3, $S' = -1.2e8$ s/m^4, and $D = 17e\text{-}9$ s/m^2; the ratio D/S

indicates a displacement of the global ZDW by +0.7 nm from 1554.6 nm. When compared to realistic fibers [99], the slope derivative parameter is practical as it gives rise to a β_4 value of 0.6e-55 s^4/m. It's important to recognize that this calibration method succeeded even though polarization effects (including local birefringence) were excluded from the model. This can only work when a system is dominated by local dispersion. On the other hand, a perfectly uniform fiber with constant ZDW will clearly generate an identical spectrum when its fiber ports are swapped.

The quasi CW nature of the pump is included in the simulation. A long flat top pulse has the advantage that it can be simulated using a CW beam. Then, the simulated CW beam will generate an optical spectrum which can be scaled down in power to give correct results based on the pulse duration and the repetition rate. Such a

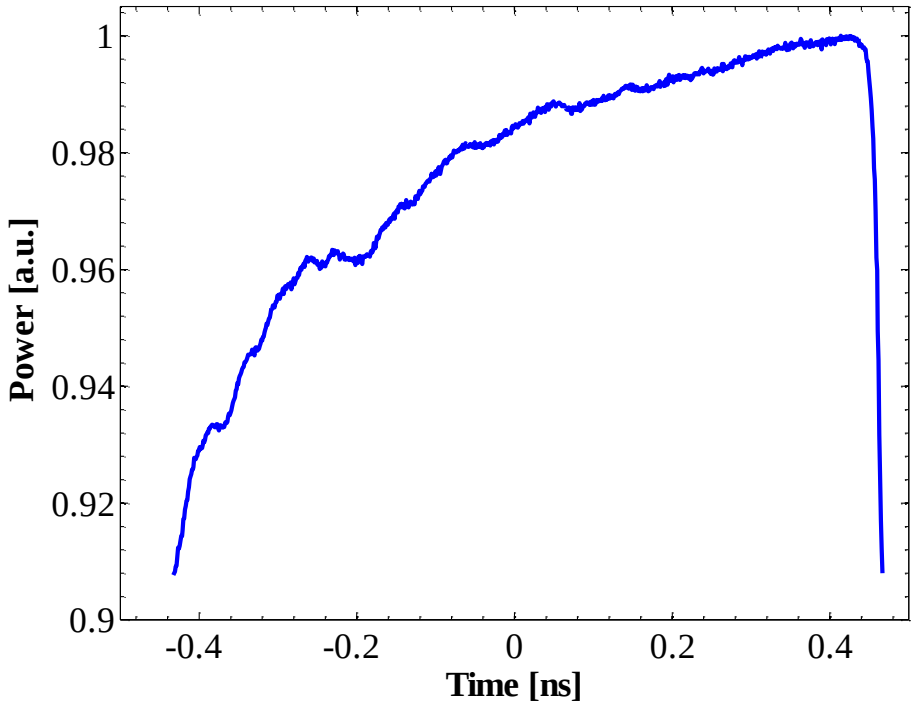

Figure 26: Temporal Measurement Showing the Top Part of the Quasi-CW Pulse | This measurement is taken at the 1% tap of the amplifier (shown in Fig. Figure **23**(a)); the optical power is normalized and presented in linear scale.

computation method will indeed be the fastest. Unfortunately, this is not the case; the pulse top has a significant variation of several percent. On the other hand, simulating the exact temporal input as in the experiment will give accurate result but will incur unreasonable computational cost. Fortunately, only the high power region of the temporal input contributes to the nonlinear optical creation of parametric fluorescence. Therefore, it is only the variations on the top of the pulse which are needed in the simulation. In fact the optical spectrum measurement shows a contribution from a collection of power levels, where the spectral shape created by each power level is different. The field input used for the calibration was comprised of seven temporal concatenation of the pulse top as captured by the equivalent time scope; the number of concatenations was chosen in accordance with computational resources. Regarding the y-axis, the pulse top was selected from its peak down by 9% (0.42 dB), as shown in Figure 26.

5.3. Photon Gate Static Response

In this section we provide additional support to the claims made previously by showing that photon gate static response can be simulated using the results of the calibration process. The static response is described as the signal-induced depletion of a quasi-CW pump in a deeply saturated FOPA using a weak CW signal. This reflects our original motivation for this study: mapping a rapidly varying weak signal on top of a moderate pump; therefore we limit the measurement to the pump response. Generally, using this type of static characterization serves two purposes: extract an

upper limit on the dynamic behavior of photon gate [161], [162], and identify the extent of its non-reciprocal behavior (Section 3.4).

During this measurement, the pump input state is kept fixed while the signal input (power and wavelength) is swept to measure the extinction ratio (ER) of the pump, resulting in a two-dimensional contour map. The ER is defined here as the ratio of the pump output power in the presence and absence of the CW signal. (A different terminology can be chosen in which pump and signal are labeled as signal and control, respectively [29].) By introducing a signal into the system, in addition to the creation of a parametric fluorescence, the FOPA will amplify the signal and generate idlers. Consequently, when a signal is present, FOPA saturation increases and so does the depletion of the pump (Figure 11), thus generating an inverse response of the pump output power to the signal input power. For example, if the insertion of a given signal weakens the pump output power by 3 dB then this is the ER at that specific signal state. To observe an appreciable signal-induced pump depletion using a weak signal, the FoM of the amplifier needs to be sufficiently high. However, if the FoM is too high, amplified vacuum noise may dominate the system's response and reduce the pump sensitivity to the presence of the signal (Figure 16).

Conversely to the measurement in the previous section where it is possible to average the affect of the pump SOP, for the static measurement, specific SOPs need to be selected for pump and signal. Prior to measurement, the SOP of signal and pump is each manually optimized to produce maximal pump ER at a signal power level of -30 dBm (Figure 27). This power level is in accordance with our interest in weak signals,

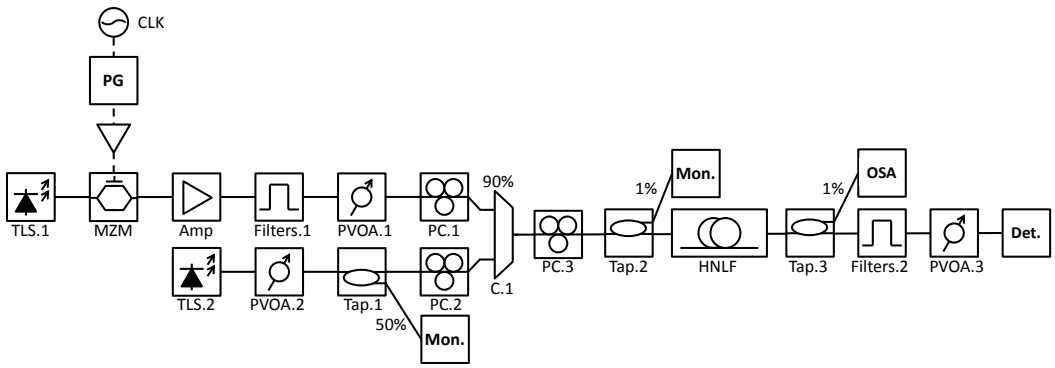

Figure 27: Schematic Description of the Experimental Setup for Photon Gate's Static Response Measurement | CW tunable laser source (TLS), Mach-Zehnder modulator (MZM), pattern generator (PG), 10 GHz RF clock (CLK), erbium doped fiber amplifier (Amp), optical filters (Filters), programmable variable optical attenuator (PVOA), power meter (Mon), detection (Det), and polarization controller (PC). TLS.1 and TLS.2 are the pump and the signal branch respectively. A circulator is located before PC.2 to monitor for SBS (not shown).

particularly when viewed as pulses temporally confined to picosecond scale. For this demonstration the pump wavelength is set to 1552 nm, although other pump wavelengths can equally be used; in fact, measurements were taken at additional pump wavelengths: 1553, 1554, and 1555 nm and resulted in similar quality of agreement with simulation (Figure 28), but for brevity are not displayed. After the CW signal and quasi-CW pump are launched into the HNLF, a 2 nm bandpass filter is used to filter the depleted pump following the HNLF. The filtered pump is then optically attenuated and subsequently detected using a 10G photodiode and a time-equivalent scope (Figure 27). By monitoring the averaged trace on the scope, specifically the voltage reading at the center of the pulse and comparing it with the signal-off state reference level, the pump ER is extracted for each signal state. The experiment is automated, including the signal sweep and the detection, to ensure rapid and stable measurement. During the experiment the CW signal is swept both in power between -40 and -20 dBm in intervals of 1 dB, and in wavelength between 1557 and 1567 nm at intervals of 0.1 nm, corresponding to a signal-pump detuning ranging from +5 to +15 nm. The

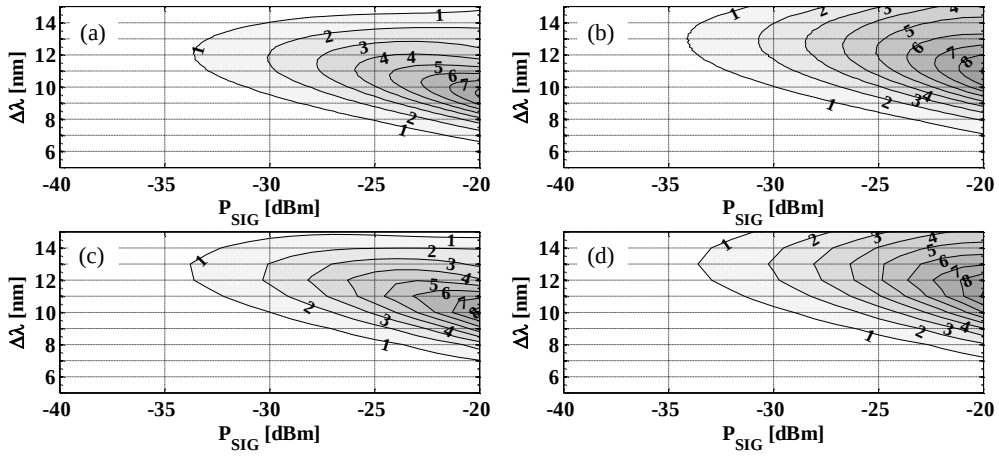

Figure 28: Photon Gate Static Response | The figures show both experimental, (a) and (b), and simulated, (c) and (d), results. The forward orientation response is shown at (a) and (c), and the backward orientation is shown at (b) and (d). The figures show pump ER (contour-levels) in decibel as a function of the signal state: power level (x-axis), and wavelength position with respect to pump wavelength (y-axis).

average pump power at the input to the HNLF is 14.4 dBm, with period and pulse durations of 63.1 ns and 1 ns, respectively. Figure 28, (a) and (b), show the static measurement results for both forward and backward orientation. The ER is presented in units of decibels, where each step in the contour map is of 1 dB. Indeed, experimental results of the static measurements show photon-gate's non-reciprocal transfer function.

Using the results from the previous section, a simulation of the static-measurement is performed for both orientations; however, since the measurement is done in the temporal domain, specifically at the center of the pulse, and is focused on a particular power level, it is possible to simulate the pump as a CW which simplifies the simulation. Nevertheless, simulating a single map requires a significant amount of time and computational resources, deeming map-optimization, at least currently, unfeasible. As fiber parameters are known from the calibration process, the CW pump power level was gauged by fitting the spectral trace of the parametric fluorescence at

the signal-off state. The simulated maps are generated using pump power levels of 31.0 and 30.8 dBm for the forward and backward orientation, respectively –shown in Figure 28, (c) and (d). The simulated results are computed at signal-sweep intervals of 1 nm and 1 dB. Remarkably, even though the scalar model neglects polarization effects, the simulation is able to reproduce the measurement including FOPA non-reciprocal behavior. This is the first time, to the best of our knowledge, a simulation strategy capable of predicting FOPA non-reciprocal behavior is demonstrated. As shown in this case, polarization effects (global and local) are not the factor dominating the non-reciprocal response of the system, but instead it is dispersion; however, from a fundamental standpoint, this does not rule out the possibility of observing non-reciprocity in high FoM FOPAs due to random birefringence.

Following this experiment, further optimization was performed on the system in an effort to produce a static response map with higher performance to investigate the efficiency and speed of few-photon control. In the first set of measurements, the depletion of a high-power pump seeded by a small continuous wave (CW) signal was characterized. To eliminate any effect of Brillouin scattering, the high-power CW pump was converted into quasi-CW, 1-ns pulse with 1.59-W peak power and 47-dB OSNR, using 0.1 nm RBW. The pump depletion map (Figure 29(a)) illustrates the static transfer characteristics of the photon gate when the pump was centered at 1554 nm. The static measurement accuracy (±0.065 dB) imposed the minimum observable depletion level, limiting the smallest input signal power to 30 nW during the measurement. To estimate the maximum bandwidth of the control signal pulse, we

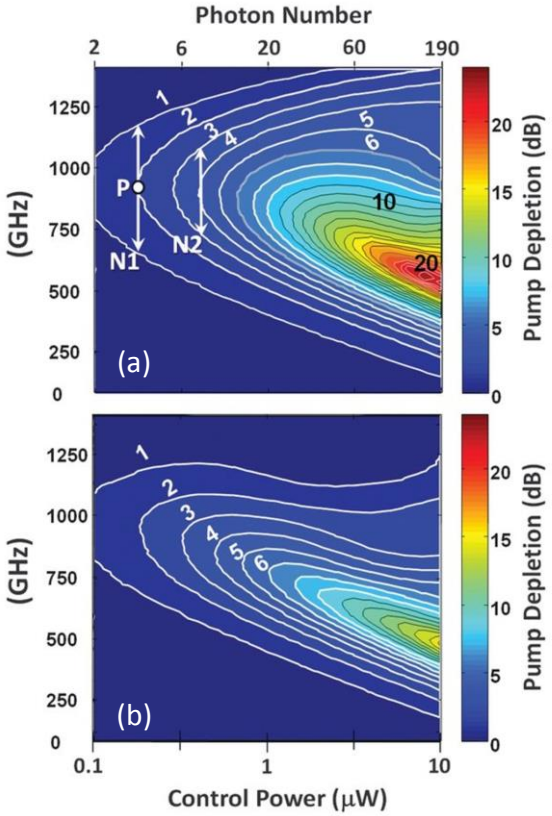

Figure 29: Static Response of a High Performing Photon Gate | (**a**) Measured bandwidth-depletion map for fiber shown in Figure 24; 1-dB pump depletion corresponds to a 3-photon pulse (N1), and 3-dB pump depletion corresponds to an 8-photon pulse (N2). Pump-signal spectral separation was measured with 12-GHz resolution. Control power was varied with 1-dB step. (**b**) FWM non-reciprocity; Bandwidth depletion map obtained by reversing the direction of pump and signal propagation. Horizontal axis indicates power in the input (control) pulse (bottom) and the corresponding average photon count (top).

consider a 1-dB pump depletion level that is ~10 times above the measurement accuracy. For an input control power of 178 nW, the signal can be tuned over 520 GHz (line N1 in Figure 29(a)) while maintaining the minimum 1-dB pump depletion level. This underestimates the true pump depletion level: The 178-nW signal positioned in the middle of this frequency range (point P in Figure 29(a)) will lead to higher (~2 dB) pump depletion. However, even with this constraint, it is possible to estimate the minimum photon number in the control pulse allowed by this fiber: A 2.5-ps-long pulse with peak power of 178 nW contains less than three photons, indicating

the feasibility of few-photon switching at a 500-GHz rate. The same experimental architecture was used to test the non-reciprocity hypothesis of this work by inverting the physical direction of the interaction. Indeed, if a unique core variation function leads to optimum photon switching, then a directionally inverted process would be suboptimal. Consequently, the input and output ports of the fiber were swapped, and the CW depletion map was measured again (Figure 29(b)). We note the striking differences between the responses shown in Figure 29, (a) and (b), with respect to both the maximum pump depletion and the depletion-bandwidth product. Although useful in estimating the performance of few-photon control, these static depletion measurements alone cannot accurately quantify the ultrafast switching response because wide signal bandwidth precludes the assumption of monochromatic phase matching.

5.4. Conclusions

This work studied the origin of non-reciprocal behavior in high FoM FOPAs. Although this behavior was numerically shown to be related to local dispersion, prior to this work a direct connection between the two including attention to polarization in this context had not yet been discussed.

Initially, we demonstrated the simplest manifestation of high FoM FOPA non-reciprocal behavior in the form of parametric fluorescence. We showed that this was indeed the result of the fiber's inhomogeneous nature rather than a polarization effect, and specifically were able to demonstrate that the unique and complex signatures of both forward and backward orientation can be described using a scalar model with the

use of a single set of fiber parameters which include the local dispersion profile of the HNLF. At the same time, this method was used as a calibration process for the fiber global parameters.

In the second half of this work, we showed the strength of this method by demonstrating its ability to correctly describe photon gate response to a weak CW signal – the static response. The result of the experimentally measured static response describes the gate's non-reciprocal transfer function. Remarkably, using the calibration process, the inhomogeneous scalar model incorporating the local dispersion profile of the HNLF was able to accurately reproduce the static measurement including the feature of non-reciprocity. This indicates that the affect of (local) random birefringence is sufficiently weak compared to that of local core scaling effects, which cause the ZDW to vary along the HNLF. Had polarization effects dominated the system, the scalar model could not succeed in reproducing the experimental results even in principles.

While it is important to establish local dispersion as the driver of this system, the limitation of this model needs to be recognized. Future studies should include an extended model which incorporates the pump optical signal to noise ratio (OSNR) [162]. The extent to which this model can accurately describe the system is not clear, specifically when it has a wider bandwidth and a higher signal-sensitivity level of the signal-induced pump depletion effect. Then, the system might have an increased dependence on birefringence, require inclusion of higher order dispersion term, and at its ultimate performance limit of few photons levels might even require a fuller description of the quantum nature of the interaction. Bearing in mind the

computational cost of simulating high FoM FOPAs, development of a computationally-efficient method to solve the NLS equation will be extremely beneficial in expediting design studies and the exploration of their dynamical properties [165].

Additionally, the high-performance static response measurement confirms that HNLF is a feasible platform for construction of high FoM (distributed) FOPAs driven by a moderate pump power level. The results predict that such distributed switching device poses ultrafast switching capability (control power and response time) at few photons level.

Lastly, it is important to emphasize the need to include the inhomogeneous nature of the system when studying a high FoM FOPA. This report serves as an additional step in highlighting the influence of local dispersion in dictating high FoM FOPAs' performance.

Chapter 5, in part, is currently being prepared for submission for publication of the material. Ron R. Nissim, Ana Pejkic, Evgeny Myslivets, Nikola Alic, and Stojan Radic. The dissertation author was the primary investigator, and the primary author of this material.

Chapter 5, in part, is a reprint of material as it appears in *Science* **345**(6195), 417-419 (2014), Ron Nissim, Ana Pejkic, Evgeny Myslivets, Bill P. Kuo, Nikola Alic, and Stojan Radic. The dissertation author was a co-primary investigator.

Chapter 6

Summary and Future Directions

6.1. Summary

This dissertation discussed the topic of locally controlled, deeply saturated parametric amplifiers and explored a new approach to light manipulation using low-power ultrafast optical control. At the starting point of this research, in 2010, little was known about such physical systems, let alone when they are operated in a weak input regime. At that time, on the theoretical part, analytical analysis to the problem of deep saturation in OPAs was limited to a uniform, noise-less, three-wave model. On the empirical part, a single experiment was published in 2008 showed interesting results but failed to address the underlying physics. In the second half of 2014, with the completion of this dissertation, publication activity on this topic resumed as a result of this work.

In April 2010, the starting date of this project, little was known and the goal of the first part was set high: Studying the performance limit of this system. It included establishing a benchmark by finding the ultimate performance limit of an ideal, (unphysical) perfectly uniform fiber, and then introducing core-size longitudinal fluctuation into the fiber, exploring its influence on the performance and establishing engineering rules concerning device realization. With the completion of this part it was understood that (1) core size fluctuations play a major role in this system and

require molecular-scale fabrication control; (2) vacuum-noise must be included when addressing this system; (3) at least theoretically, the system can be ultrafast and extremely sensitive to weak inputs; and (4) have a non-reciprocal transfer function.

The consequences were clear and had broad implications: (a) previous simplified models which were widely used were not valid for this type of problem. Any model related to deeply saturated OPAs had to include broad-band vacuum noise, higher order idlers, and the inhomogeneous nature of the fiber. (b) The effect of non-reciprocity could especially not be predicted using a uniform fiber model, and certainly cannot be studied without a non-uniform model. (c) Since this model had to be solved numerically using a high FoM, it required significant computational resources, which were not easily accessible at that time. (d) The benchmark predicted the system can have, despite the presence of noise, very high performance – much more than has been observed so far - but also that a fiber's core will need to be controlled to a nanometer scale; (e) fibers with identical global properties (mean and variance) can show diverse level of performance in physical fibers and therefore inhibits efficient construction of high performance deeply saturated OPAs.

The second part of this work was as a direct continuation of the previous part, which showed a group of well-performing fibers composed of a variety of members with different variance of core fluctuations. It implied the existence of dispersion profiles which are able to positively influence the mixing process. Indeed, this contradicted the common notion at that time, which considered a uniform fiber, with a constant ZDW, as the most desirable. Consequently, the second part of this work sought after a "golden" dispersion profile.

The search for a unique dispersion profile was made in three steps: Initially, a benchmark was reestablished using powerful tools. Then, two fiber-profile representations were made, with a high and low number of degrees of freedom. These representations were subsequently used to optimize the fiber profile to a shape that will produce the highest ER. Finally, all the results were validated for their performance. With the completion of this part it was understood that the conception was wrong, and that performance of inhomogeneous (physical) fibers can be significantly superior to that of a uniform fiber, if the fiber is properly designed.

Here, too, results had broad consequences: local dispersion again played a critical role in the behavior of a deeply saturated OPA. The results obtained by the inhomogeneous model demonstrated a significant improvement over the benchmark, showing a performance level which can only be accounted for by introducing spatial non-uniformities into the fiber. It showed that the common notion of uniform fibers being the most desirable structure is not true. Indeed, any experimental result which exceeds the benchmark level cannot be explained with the commonly used uniform FOPA model. The inhomogeneous FOPA model introduces new opportunities, if one is able to abandon the uniform fiber model.

The last part of this work dealt with experimental demonstration of a high performance deeply saturated FOPA. It included (1) a demonstration of non-reciprocity and its origin, (2) developing a simulation strategy capable of predicting FOPA non-reciprocal transfer function, and (3) a static measurement predicting wide-band low-power switching.

The results obtained in this part have confirmed the claims made in the previous parts. Non-reciprocity was demonstrated and was shown to be the result of the local ZDW of the fiber. This was proven in part by numerically reproducing the experiment with the use of inhomogeneous scalar FOPA model. Lastly, the static response of the deeply saturated FOPA was characterized and shown to have high performance.

6.2. Future Directions

This work presented a very promising technology; however, since this is the first study of its kind, much work is left to be done in this area. As was shown, the ability to perform simulations is very important, as it assists in a variety of studies including: optimization; calibration; perturbation analysis; etc. Unfortunately, simulating a deeply saturated OPA is computationally expensive because of its combination of characteristics – that is, of being highly noisy with wide BW and high FoM, and the need to perform averaging. The introduction of GPU computing into this field in the early stages of this work enabled the numerical study; nevertheless, there is a need to develop a computationally efficient method to solve the NLSE. Such studies are occurring elsewhere [165], and could be utilized in this study. For example, stronger simulation ability will enable one to perform constrained optimization, which is necessary to the development of practical FOPA designs. Another point concerning NLSE is related to the fact that as a deeply saturated OPA becomes more sensitive a semi-classical NLSE model might not work well due to its continuous nature. This requires the development of a theory, a more advanced theory which will allow

researchers to explore this device at its fundamental limits: for example, whether photon gate response can be discrete, as in [166]. This issue will need to be addressed at some point. With regards to theory, this work contributed to intuitive understanding of this system: nevertheless the system still lacks analytical and intuitive knowledge, which also have to be extended to engineering rules. Since analytical methods to solving a full NLSE with noise have not yet been demonstrated, a more practical approach will be the development of a semi analytical approach for performance estimation and design which could help reduce the computational load for a deeply saturated inhomogeneous OPA. The discussion on polarization effects need to be extended. Developing polarization stable photon gate will be required to make this technology viable and will contribute to field of FOPAs in general. The first work on the topic of FOPA reciprocity theory was done by Marhic. This work helped extend this theory and show a regime in which FOPAs have non-reciprocal behavior, and it is expected to be further developed. Open questions, for example: What is the role of higher order idlers in promoting non-reciprocal behavior? What are the limits of this non-reciprocal response and how is it affected by local dispersion (and local polarization)? Additional future work can focus on pushing the extinction ratio – bandwidth product. As shown in Torilo's paper, as well as in this work, with the increase in signal induced pump depletion the operating BW tends to shrink, which is not necessarily desirable, and the questions on photon gate limits in this regard still exist.

As this is the first study of its kind, the decision to start with typical HNLFs seemed natural. Consequently this work focused on a (spectrally uninhibited) broad

band single pass amplifier using conventional HNLFs. There are many more architectures which should be studied before concluding on a preferred approach. With the new knowledge encompassed in this work, other architectures can be better evaluated. For example: Open structures (single/double pass amplifier) *vs.* closed structures like an OPO. This work focused on a single pump, whereas future studies can use multiple pumps in various configurations: Non/degenerate, Un/correlated, and Co/Cross polarized.

With a better understanding on the role of noise and local dispersion, a natural continuation will be to use tools to gain synthesis for noise suppression, and dispersion stabilization. A mixer structure could be heterogonous and combine different types of fibers. There is also room to investigate shock wave mixers because of their quality combination of coherence, noise suppressing, and wide band operation; however, their BW-operation capability regarding the acceptance of a modulated signal is not clear. Local dispersion engineering needs to be harnessed and investigated further because of its criticality for photon gate. Additionally, it will also benefit other applications, and will need to be investigated further. Currently photon gate is not phase sensitive; the natural next stage will be to explore the properties of a coherent (phase sensitive) photon gate. The fact the three wave model is analytically solvable gives it an advantage, and makes this system simpler to analyze. It will be interesting to develop architectures which support noise inhibition and which will behave according to this theory. On a general note, as shown in this work, noise plays a critical role in this system, and the ability to discriminate between noise and signal is critical. Therefore,

it will be insightful to continue to study the role of noise by exploring spectrally inhibited systems as the ones mentioned before.

The results shown in this work were based on a CW signal, effectively resulting in a time-independent analysis. Future work should explore the dynamical behavior of the system and include the relation between the behavior of a CW and pulsed signal operation. There is also a need to continue the development of characterization methods.

Lastly, photon gate should be applied to various high-demand applications: (1) measure a sensitive physical effect in previously forbidden regimes; (2) combine photon gate with a threshold-less laser to produce a real low power modulation; (3) create state-of-the-art receivers, and (4) energy efficient amplifiers.

REFERENCES

[1] N. Bloembergen, “Nonlinear Optics: Past, Present, and Future,” *IEEE J. Sel. Top. Quant. Electron.* **6**(6), 876-880 (2000)

[2] T. H. Maiman, “Stimulated Optical Radiation in Ruby,” *Nature* **187**(4736), 493-494 (1960)

[3] The Royal Swedish Academy of Sciences, “Two Revolutionary Optical Technologies,” *AAPPS Bulletin* **19**(6), 10-17 (2009)

[4] Govind P. Agrawal, *Lightwave Technology : Telecommunication Systems*. Hoboken, New Jersey: Wiley, 2005.

[5] J. Berthold, A. A. M. Saleh, L. Blair, and J. M. Simmons, “Optical Networking: Past, Present, and Future,” *J. Lightwave Technol.* **26**(9), 1104-1118 (2008)

[6] R. W. Tkach, “Scaling Optical Communications for the Next Decade and Beyond,” *Bell Labs Technical Journal* **14**(4), 3-10 (2010)

[7] Hideo MIYAHARA, Toward New Generation Networks, September 2010, Opening Session, 13th German-Japanese Symposium, Osaka, Japan.

[8] R. J. Essiambre and R. W. Tkach, “Capacity Trends and Limits of Optical Communication Networks,” *Proc. IEEE* **100**(5), 1035-1055 (2012)

[9] R. Bolla, R. Bruschi, A. Carrega, F. Davoli, D. Suino, C. Vassilakis, and A. Zafeiropoulos, “Cutting the energy bills of Internet Service Providers and telecoms through power management: An impact analysis,” *Computer Networks* **56**(10), 2320-2342 (2012)

[10] P. Green, “Progress in Optical Networking,” *IEEE Commun. Mag.* **29**(1), 54-61 (2001)

[11] B. J. Eggleton, B. Luther-Davies, and K. Richardson, "Chalcogenide Photonics," *Nat. Photonics* **5**(3), 141-148 (2011)

[12] Paul N. Butcher and David Cotter, *The Elements of Nonlinear Optics*, P. L. Knight and W. J. Firth, Eds. New York, United Kingdom: Cambridge University Press, 1990, ch. 7, p. 227.

[13] Govind P. Agrawal, *Nonlinear Fiber Optics*, 4th ed. San Diego, California: Academic Press, 2007.

[14] K. J. Blow and D. Wood, "Theoretical Description of Transient Stimulated Raman Scattering in Optical Fibers," *IEEE J. Quantum Elect.* **25**(12), 2665-2673 (1989)

[15] M. Karlsson, "Four-wave mixing in fibers with randomly varying zero-dispersion wavelength," *J. Opt. Soc. Am. B* **15**(8), 2269-2275 (1998)

[16] X. Bao W. Li, Y. Li, and L. Chen, "Differential pulse-width pair BOTDA for high spatial resolution sensing," *Opt. Express* **16**(26), 21616-21625 (2008)

[17] X. Yin and X. Zhang, "Unidirectional light propagation at exceptional points," *Nat. Materials* **12**(3), 175-177 (2013)

[18] K. Fang, Z. Yu, V. Liu, and S. Fan, "Ultracompact nonreciprocal optical isolator based on guided resonance in a magneto-optical photonic crystal slab," *Opt. Lett.* **36**(21), 4254-4256 (2011)

[19] R. J. Potton, "Reciprocity in optics," *Rep. Prog. Phys.* **67**(5), 717-754 (2004)

[20] G. Leuchs and M. Sondermann, "Time-reversal symmetry in optics," *Phys. Scr.* **85**(5), 058101 (2012)

[21] R. El-Ganainy, K. G. Makris, D. N. Christodoulides, and Z. H. Musslimani, "Theory of coupled optical PT-symmetric structures," *Opt. Lett.* **32**(17), 2632-

2634 (2007)

[22] C. E. Rüter, K. G. Makris, R. El-Ganainy, D. N. Christodoulides, M. Segev, and D. Kip, "Observation of parity–time symmetry in optics," *Nat. Physics* **6**(3), 192-195 (2010)

[23] L. Feng, M. Ayache, J. Huang, Y.-L. Xu, M.-H. Lu, Y.-F.Chen, Y. Fainman, and A. Scherer, "Nonreciprocal light propagation in a silicon photonic circuit," *Science* **333**(6043), 729-733 (2011)

[24] H. Lira, Z. Yu, S. Fan, and M. Lipson, "Electrically Driven Nonreciprocity Induced by Interband Photonic Transition on a Silicon Chip," *PRL* **109**(3), 033901 (2012)

[25] L. Fan, J. Wang, L. T. Varghese, H. Shen, B. Niu, Y. Xuan, A. M. Weiner, and M. Qi, "An All-Silicon Passive Optical Diode," *Science* **335**(6067), 447-450 (2012)

[26] D. Jalas, A. Petrov, M. Eich, W. Freude, S. Fan, Z. Yu, R. Baets, M. Popović, A. Melloni, J. D. Joannopoulos, M. Vanwolleghem, C. R. Doerr, and H. Renner, "What is—and what is not—an optical isolator," *Nat. Photonics* **7**(8), 579-582 (2013)

[27] G. Cappellini and S. Trillo, "Third-order three-wave mixing in single-mode fibers: exact solutions and spatial instability effects," *J. Opt. Soc. Am. B* **8**(4), 824-838 (1991)

[28] P. Kylemark, H. Sunnerud, M. Karlsson, and P. A. Andrekson, "Semi-analytic saturation theory of fiber optical parametric amplifiers," *J. Lightwave Technol.* **24**(9), 3471-3479 (2006)

[29] P. A. Andrekson, H. Sunnerud, S. Oda, T. Nishitani, and J. Yang, "Ultrafast, atto-Joule switch using fiber-optic parametric amplifier operated in saturation," *Opt. Express* **16**(15), 10956-10961 (2008)

[30] Y. Wang, X. Zhang, X. Ren, L. Zheng, X. Liu, and Y. Huang, “Design and analysis of a dispersion flattened and highly nonlinear photonic crystal fiber with ultralow confinement loss,” *Appl. Opt.* **49**(3), 292-297 (2010)

[31] M. Hirano, T. Nakanishi, T. Okuno, and M. Onishi, "Selective FWM-based wavelength conversion realized by highly nonlinear fiber," in *Proc. ECOC TH.1.3.5*, Cannes, 2006, pp. 21-22.

[32] M. Onishi, Y. Koyano, M. Shigematsu, H. Kanamori, and M. Nishimura, “Dispersion compensating fibre with a high figure of merit of 250 ps/nm/dB,” *Electron. Lett.* **30**(2), 161-163 (1994)

[33] M. Hirano, T. Nakanishi, T. Okuno, and M. Onishi, "Broadband wavelength conversion over 193-nm by HNL-DSF improving higher-order dispersion performance," in *Proc. ECOC PDP TH.4.4.4*, Glasgow, 2005, pp. 43-44.

[34] M. Hirano, T. Nakanishi, and T. Sasaki, "Highly nonlinear fiber with reduced dispersion slope and efficient wavelength conversion with sub-ps walk-off," in *Proc. OFC OMP5*, San Diego, 2008.

[35] T. Okuno, M. Hirano, T. Kato, M. Shigematsu, and M. Onishi, “Highly nonlinear and perfectly dispersion-flattened fibers for efficient optical signal processing applications,” *Electron. Lett.* **39**(13), 972-974 (2003)

[36] T. Nakanishi, M. Hirano, T. Okuno, and M. Onishi, "Silica-based highly nonlinear fiber with γ=30/W/km and its FWM-based conversion efficiency," in *Proc. OFC OTuH7*, Anaheim, 2006.

[37] H. Lee, T. Chen, J. Li, O. Painter, and K. J. Vahala, “Ultra-low-loss optical delay line on a silicon chip,” *Nat. Commun.* **3**, 867 (2012)

[38] D. Y. Oh, D. Sell, H. Lee, K. Y. Yang, S. A. Diddams, and K. J. Vahala, “Supercontinuum generation in an on-chip silica waveguide,” *Opt. Lett.* **39**(4), 1046-1048 (2014)

[39] J. H. Lee, W. Belardi, K. Furusawa, P. Petropoulos, Z. Yusoff, T. M. Monro, and D. J. Richardson, “Four-wave mixing based 10-Gb/s tunable wavelength conversion using a holey fiber with a high SBS threshold,” *IEEE Photon. Technol. Lett.* **15**(3), 440-442 (2003)

[40] T. Nagashima, T. Hasegawa, S. Ohara, N. Sugimoto, and K. Kikuchi, "Multi-step-index Bismuth-based highly nonlinear fiber with low propagation loss and splicing loss," in *Proc. OFC ThA2*, Anaheim, 2005.

[41] N. Sugimoto, T. Nagashima, T. Hasegawa, S. Ohara, K. Taira, and K. Kikuchi, "Bismuth-based optical fiber with nonlinear coefficient of 1360 W−1km-1," in *Proc. OFC PDP22*, Anaheim, 2004.

[42] J. H. Lee, T. Nagashima, T. Hasegawa, S. Ohara, N. Sugimoto, and K. Kikuchi, “Bismuth-Oxide-Based Nonlinear Fiber With a High SBS Threshold and Its Application to Four-Wave-Mixing Wavelength Conversion Using a Pure Continuous-Wave Pump,” *IEEE JOURNAL OF LIGHTWAVE TECHNOLOGY* **24**(1), 22-28 (2006)

[43] H. Ebendorff-Heidepriem, P. Petropoulos, S. Asimakis, V. Finazzi, R. C. Moore, K. Frampton, F. Koizumi, D. J. Richardson, and T. M. Monro, “Bismuth glass holey fibers with high nonlinearity,” *OPTICS EXPRESS* **12**(21), 5082-5087 (2004)

[44] A. Mori, K. Shikano, K. Enbutsu, K. Oikawa, K. Naganuma, M. Kato, and S. Aozawa, "1.5μm band zero-dispersion shifted tellurite photonic crystal fibre with a nonlinear coefficient γ of 675W-1km-1," in *Proc. ECOC Th.3.3.6*, Glasgow, 2004.

[45] J. Y. Y. Leong, P. Petropoulus, S. Asimakis, H. Ebendorff-Heidepriem, R. C. Moore, K. Frampton, V. Finazzi, X. Feng, J. H. V. Price, T. M.Monro, and D. J. Richardson, "A lead silicate holey fiber with γ=1860W-1km-1 at 1550nm," in *Proc. OFC PDP22*, Anaheim, 2005.

[46] L. Fu, M. Rochette, V. Ta’eed, D. Moss, and B. Eggleton, “Investigation of self-phase modulation based optical regeneration in single mode As2Se3 chalcogenide glass fiber,” *Opt. Exp.* **13**(19), 7637-7644 (2005)

[47] D.-I. Yeom, E. C. Mägi, M. R. E. Lamont, M. A. F. Roelens, L. Fu, and B. J. Eggleton, "Low-threshold supercontinuum generation in highly nonlinear chalcogenide nanowires," *Optics Letters* **33**(7), 660-662 (2008)

[48] M. Asobe, T. Kanamori, K. Naganuma, H. Itoh, and T. Kaino, "Third-order nonlinear spectroscopy in As2S3 chalcogenide glass fibers," *Journal of Applied Physics* **77**(11), 5518-5523 (1995)

[49] S. J. Madden, D-Y. Choi, D. A. Bulla, A. V. Rode, B. Luther-Davies, V.G. Ta'eed, M.D. Pelusi, and B.J. Eggleton, "Long, low loss etched As2S3 chalcogenide waveguides for all-optical signal regeneration," *Opt. Express* **15**(22), 14414-14421 (2007)

[50] M. R.E. Lamont, B. Luther-Davies, D.-Y. Choi, S. Madden, and B. J. Eggleton, "Supercontinuum generation in dispersion engineered highly nonlinear (γ = 10 /W/m) As2S3 chalcogenide planar waveguide," *Opt. Express* **16**(19), 14938-14944 (2008)

[51] K. Suzuki, Y. Hamachi, and T. Baba, "Fabrication and characterization of chalcogenide glass photonic crystal waveguides," *Opt. Express* **17**(25), 22393-22400 (2009)

[52] K. Suzuki and T. Baba, "Nonlinear light propagation in chalcogenide photonic crystal slow light waveguides," *Opt. Express* **18**(25), 26675-26685 (2010)

[53] X. Gai, S. Madden, D.-Y. Choi, D. Bulla, and B. Luther-Davies, "Dispersion engineered Ge11.5As24Se64.5 nanowires with a nonlinear parameter of 136W-1m-1 at 1550nm," *Opt. Express* **18**(18), 18866-18874 (2010)

[54] C. Lacava, V. Pusino, P. Minzioni, M. Sorel, and I. Cristiani, "Nonlinear properties of AlGaAs waveguides in continuous wave operation regime," *Opt. Express* **22**(5), 5291-5298 (2014)

[55] M. A. Foster, A. C. Turner, J. E. Sharping, B. S. Schmidt, M. Lipson, and A. L. Gaeta, "Broad-band optical parametric gain on a silicon photonic chip," *Nature* **441**(7096), 960-963 (2006)

[56] R. Salem, M. A. Foster, A. C. Turner, D. F. Geraghty, M. Lipson, and A. L. Gaeta, "Signal regeneration using lowpower four-wave mixing on silicon chip," *Nature Photonics* **2**(1), 35-38 (2008)

[57] J. Cardenas, C. B. Poitras, J. T. Robinson, K. Preston, L. Chen, and M. Lipson, "Low loss etchless silicon photonic waveguides," *Opt. Express* **17**(6), 4752-4757 (2009)

[58] M. A. Foster, A. C. Turner, M. Lipson, and A. L. Gaeta, "Nonlinear optics in photonic nanowires," *Opt. Express* **16**(2), 1300-1320 (2008)

[59] P. Dong, W. Qian, S. Liao, H. Liang, C.-C. Kung, N.-N. Feng, R. Shafiiha, J. Fong, D. Feng, A. V. Krishnamoorthy, and M. Asghari, "Low loss shallow-ridge silicon waveguides," *Opt Express* **18**(14), 14474-14479 (2010)

[60] D. J. Moss, S. D. Jackson, A. Pasquazi, M. Peccianti, and R. Morandotti, "CMOS Compatible Chips for Applications in Nonlinear Optics," in *Photonics North*, Ottawa, 2013, p. 89150N.

[61] R. DeSalvo, A. A. Said, D. J. Hagan, E. W. Van Stryland, and M. Sheik-Bahae, "Infrared to ultraviolet measurements of two-photon absorption and n2 in wide bandgap solids," *IEEE J. Quantum Electron.* **32**(8), 1324-1333 (1996)

[62] L. Leontie, M. Caraman, A. Visinoiu, and G. I. Rusu, "On the optical properties of bismuth oxide thin films prepared by pulsed laser deposition," *Thin Solid Films* **473**(2), 230-235 (2005)

[63] W. F. Hagen and E. Snitzer, "Nonlinear Solarization in Flint Glasses by Intense 0.53-μm Light," *IEEE Journal of Quantum Electronics* **4**(5), 361 (1968)

[64] M. A. Newhouse, D. L. Weidman, and D. W. Hall, "Enhanced-nonlinearity single-mode lead silicate optical fiber," *Optics Lett.* **15**(21), 1185-1187 (1990)

[65] A. D. Bristow, N. Rotenberg, and H.M. van Driel, "Two-photon absorption and Kerr coefficients of silicon for 850–2200 nm," *Applied physics letters* **90**(19),

191104 (2007)

[66] T. Umeki, O. Tadanaga, and Masaki Asobe, "Highly Efficient Wavelength Converter Using Direct-Bonded PPZnLN Ridge Waveguide," *IEEE J. Quantum Electron.* **46**(8), 1206-1213 (2010)

[67] P. S. Kuo, J. S. Pelc, O. Slattery, Y.-S. Kim, M. M. Fejer, and X. Tang, "Reducing noise in single-photon-level frequency conversion," *Opt. Lett.* **38**(8), 1310-1312 (2013)

[68] J. S. Pelc, P. S. Kuo, O. Slattery, L. Ma, X. Tang, and M. M. Fejer, "Dual-channel, single-photon upconversion detector at 1.3 μm," *Opt. Express* **20**(17), 19075-19087 (2012)

[69] K. R. Parameswaran, R. K. Route, J. R. Kurz, R. V. Roussev, M. M. Fejer, and M. Fujimura, "Highly efficient second-harmonic generation in buried waveguides formed by annealed and reverse proton exchange in periodically poled lithium niobate," *Opt. Lett.* **27**(3), 179-181 (2002)

[70] M. H. Chou, J. Hauden, M. A. Arbore, and M. M. Fejer, "1.5-μm-band wavelength conversion based on difference-frequency generation in LiNbO3 waveguides with integrated coupling structures," *Opt. Lett.* **23**(13), 1004-1006 (1998)

[71] K. Rivoire, S. Buckley, F. Hatami, and J. Vukovi, "Second harmonic generation in GaP photonic crystal waveguides," *Appl. Phys. Lett.* **98**(26), 263113 (2011)

[72] M. Cazzanelli, F. Bianco, E. Borga, G. Pucker, M. Ghulinyan, E. Degoli, E. Luppi, V. Véniard, S. Ossicini, D. Modotto, S. Wabnitz, R. Pierobon, and L. Pavesi, "Second-harmonic generation in silicon waveguides strained by silicon nitride," *Nature materials* **11**(2), 148-154 (2012)

[73] D. C. Hutchings, S. J. Wagner, B. M. Holmes, U. Younis, A. S. Helmy, and J. Stewart Aitchison, "Type-II quasi phase matching in periodically intermixed semiconductor superlattice waveguides," *Opt. Lett.* **35**(8), 1299-1301 (2010)

[74] T. Matsushita, I. Ohta, and T. Kondo, “Quasi-Phase-Matched Parametric Fluorescence in a Periodically Inverted GaP Waveguide,” *Appl. Phys. Express* **2**(6), 061101 (2009)

[75] F. Laurell, T. Calmano, S. Müller, P. Zeil, C. Canalias, and G. Huber, “Laser-written waveguides in KTP for broadband Type II second harmonic generation,” *Opt. Express* **20**(20), 22308-22313 (2012)

[76] C. Tu, Z. Huang, K. Lou, H. Liu, Y. Wang, Y. Li, F. Lu, and H.-T. Wang, “Efficient green-light generation by frequency doubling of a picosecond all-fiber ytterbium-doped fiber amplifier in PPKTP waveguide inscribed by femtosecond laser direct writing,” *Opt. Express* **18**(24), 25183-25191 (2010)

[77] G. Nava, P. Minzioni, I. Cristiani, A.C. Busacca, L. Curcio, S. Stivala, and G. Assanto, “Integrated frequency shifter in periodically poled lithium tantalate waveguide,” *Electronics Letters* **46**(25), 1686-1688 (2010)

[78] H. Suchowski, B. D. Bruner, A. Ganany-Padowicz, I. Juwiler, A. Arie, and Y. Silberberg, “Adiabatic frequency conversion of ultrafast pulses,” *Applied Physics B* **105**(4), 697-702 (2011)

[79] G W Cong, R Akimoto, K Akita, T Hasama, and H Ishikawa, “Low-saturation-energy-driven ultrafast all-optical switching operation in (CdS/ZnSe)/BeTe intersubband transition,” *Opt. Express* **15**(19), 12123-12130 (2007)

[80] K. Nozaki, T. Tanabe, A. Shinya, S. Matsuo, T. Sato, H. Taniyama, and M. Notomi, “Sub-femtojoule all-optical switching using a photonic-crystal nanocavity,” *Nature Photonics* **4**(7), 477-483 (2010)

[81] H. Nakamura, Y. Sugimoto, and K. Asakawa, "Ultra-Fast Photonic Crystal/Quantum Dot All-Optical Switch for Future Photonic Networks," in *Proc. CLEO CThK1*, Long Beach, 2006.

[82] C. Koos, P. Vorreau, T. Vallaitis, P. Dumon, W. Bogaerts, R. Baets, B. Esembeson, I. Biaggio, T. Michinobu, F. Diederich, W. Freude, and J. Leuthold, “All-optical high-speed signal processing with silicon–organic hybrid slot

waveguides," *Nature Photonics* **3**(4), 216-219 (2009)

[83] M. Waldow, T. Plötzing, M. Gottheil, M. Först, J. Bolten, T. Wahlbrink, and H. Kurz, "25ps all-optical switching in oxygen implanted silicon-on-insulator microring resonator," *Opt. Express* **16**(11), 7693-7702 (2008)

[84] L. Liu, R. Kumar, K. Huybrechts, T. Spuesens, G. Roelkens, E.-J. Geluk, T. de Vries, P. Regreny, D. Van Thourhout, R. Baets, and G. Morthier, "An ultra-small, low-power, all-optical flip-flop memory on a silicon chip," *Nature Photonics* **4**(3), 182-187 (2010)

[85] J. Liu, M. Beals, A. Pomerene, S. Bernardis, R. Sun, J. Cheng, L. C. Kimerling, and J. Michel, "Waveguide-integrated, ultralow-energy GeSi electro-absorption modulators," *Nature Photonics* **2**(7), 433 - 437 (2008)

[86] M. Bajcsy, S. Hofferberth, V. Balic, T. Peyronel, M. Hafezi, A. S. Zibrov, V. Vuletic, and M. D. Lukin, "Efficient All-Optical Switching Using Slow Light within a Hollow Fiber," *Phys. Rev. Lett.* **102**(20), 203902 (2009)

[87] V. Venkataraman, K. Saha, P. Londero, and A. L. Gaeta, "Few-Photon All-Optical Modulation in a Photonic Band-Gap Fiber," *Phys. Rev. Lett.* **107**(19), 193902 (2011)

[88] X.-F. Han, Y.-X. Weng, R.Wang, X.-H. Chen, K.-H. Luo, L.-A. Wu, and J. Zhao, "Single-photon level ultrafast all-optical switching," *Appl. Phys. Lett.* **92**(15), 151109 (2008)

[89] E. Yüce, G. Ctistis, J. Claudon, E. Dupuy, R. D. Buijs, B. de Ronde, A. P. Mosk, J.-M. Gérard, and W. L. Vos, "All-optical switching of a microcavity repeated at terahertz rates," *Opt. Lett.* **38**(3), 374-376 (2013)

[90] T. Volz, A. Reinhard, M. Winger, A. Badolato, K. J. Hennessy, E. L. Hu, and A. Imamoğlu, "Ultrafast all-optical switching by single photons," *Nature Photonics* **6**(9), 605-609 (2012)

[91] O. Wada, “Femtosecond all-optical devices for ultrafast communication and signal processing,” *New J. Phys.* **6**(1), 183 (2004)

[92] Paul N. Butcher and David Cotter, *The Elements of Nonlinear Optics*, 1st ed., P. L. Knight and W. J. Firth, Eds. Cambridge, United Kingdom: Cambridge University Press, 1990.

[93] S Sudo, T Hosaka, and M Horiguchi, “Dimension-control technique in the VAD process and wholly synthesised single-mode fibre preform,” *Electronics Letters* **22**(19), 990-991 (1986)

[94] M. Hirano, T. Nakanishi, T. Okuno, and M. Onishi, “Silica-Based Highly Nonlinear Fibers and Their Application,” *IEEE J. Sel. Topics Quantum Electron.* **15**(1), 103-113 (2009)

[95] S. Radic, “Parametric Signal Processing,” *IEEE J. Sel. Top. Quantum Electon.* **18**(2), 670-680 (2012)

[96] J. Hansryd, F. Dross, M. Westlund, P. A. Andrekson, and S. N. Knudsen, “Increase of the SBS Threshold in a Short Highly Nonlinear Fiber by Applying a Temperature Distribution,” *J. Lightwave Technol.* **19**(11), 1691-1697 (2001)

[97] C. Lundstrom, R. Malik, L. Gruner-Nielsen, B. Corcoran, S.L.I. Olsson, M. Karlsson, and P.A. Andrekson, “Fiber Optic Parametric Amplifier With 10-dB Net Gain Without Pump Dithering,” *IEEE Photon. Technol. Lett.* **25**(3), 234-237 (2013)

[98] M. Hirano, "Highly Nonlinear Fibers and Their Applications," in *NMIJ-BIPM Joint Workshop 2007 Optical Frequency Comb - Comb, Fiber and Metrology*, Tsukuba, May 2007.

[99] M. Hirano, "Advances in High-Confinement Fibers," in *Frontiers in Optics*, San Jose, 2009, p. FTuI4.

[100] T. Okuno, M. Onishi, T. Kashiwada, S. Ishikawa, and M. Nishimura, “Silica-Based Functional Fibers with Enhanced Nonlinearity and Their Applications,”

IEEE J. Sel. Top. Quantum Electron. **5**(5), 1385-1391 (1999)

[101] T. Kato, Y. Suetsugu, and M. Nishimura, "Estimation of nonlinear refractive index in various silica-based glasses for optical fibers," *Opt. Lett.* **20**(22), 2279-2281 (1995)

[102] T. Kato, Y. Suetsugu, M. Takagi, E. Sasaoka, and M. Nishimura, "Measurement of the nonlinear refractive index in optical fiber by the cross-phase-modulation method with depolarized pump light," *Opt. Lett.* **20**(9), 988-990 (1995)

[103] S. Radic, "Parametric amplification and processing in optical fibers," *Laser & Photon. Rev.* **2**(6), 498-513 (2008)

[104] E. Myslivets, N. Alic, J. R. Windmiller, and S. Radic, "A New Class of High-Resolution Measurements of Arbitrary-Dispersion Fibers: Localization of Four-Photon Mixing Process," *J. Lightwave Technol.* **27**(3), 364-375 (2009)

[105] E. Myslivets, C. Lundstrom, J.M. Aparicio, S. Moro, A.O.J. Wiberg, C.-S. Bres, N. Alic, P.A. Andrekson, and S. Radic, "Spatial Equalization of Zero-Dispersion Wavelength Profiles in Nonlinear Fibers," *IEEE Photon. Technol. Lett.* **21**(24), 1807-1809 (2009)

[106] J. Stone, "Photorefractivity in GeO2-doped silica fibers," *J. Appl. Phys.* **62**(11), 4371-4374 (1987)

[107] R. H. Stolen, "Materials and Processing Requirements for Efficient Fiber Optic Nonlinear Devices," in *1989 MRS Fall Meeting*, vol. 172, Boston, 1989, pp. 303-313.

[108] B. P.-P. Kuo, M. Hirano, and S. Radic, "Continuous-wave, short-wavelength infrared mixer using dispersion-stabilized highly-nonlinear fiber," *Opt. Express* **20**(16), 18422-18431 (2012)

[109] X. P. Mao, R. W. Tkach, A. R. Chraplyvy, R. M. Jopson, and R. M. Derosier, "Stimulated Brillouin threshold dependence on fiber type and uniformity," *IEEE*

Photon. Technol. Lett. **4**(66), 66-69 (1992)

[110] Y. Aoki, K. Tajima, and I. Mito, “Input Power Limits of Single-Mode Optical Fibers due to Stimulated Brillouin Scattering in Optical Communication Systems,” *J. Lightwave Technol.* **6**(5), 710-719 (1988)

[111] James Coles, "Advanced Phase Modulation Techniques for Stimulated Brillouin Scattering Suppression in Fiber Optic Parametric Amplifiers," UC San Diego, La Jolla, MSc Thesis b6289908, 2009.

[112] R. H. Stolen and E. P. Ippen, “Raman gain in glass optical waveguides,” *Appl. Phys. Lett.* **22**(6), 276-278 (1973)

[113] Govind P. Agrawal, *Lightwave Technology : Components and Devices*. Hoboken, New Jersey: Wiley, 2005.

[114] J. Bromage, “Raman Amplification for Fiber Communications Systems,” *J. Lightwave Technol.* **22**(1), 79-93 (2004)

[115] R. W. Hellwarth, A. Owyoung, and N. George, “Origin of the Nonlinear Refractive Index of Liquid CCl4,” *Phys. Rev. A* **4**(6), 2342-2347 (1971)

[116] R. H. Stolen, J. P. Gordon, W. J. Tomlinson, and H. A. Haus, “Raman response function of silica-core fibers,” *J. Opt. Soc. Am. B* **6**(6), 1159-1166 (1989)

[117] A. K. Srivastava, Y. Sun, J. L. Zyskind, and J. W. Sulhoff, “EDFA transient response to channel loss in WDM transmission system,” *IEEE Photon. Technol. Lett.* **9**(3), 386-388 (1997)

[118] C. J. Chen and W. S. Wong, “Transient effects in saturated Raman amplifiers,” *Electron. Lett.* **37**(6), 371-373 (2001)

[119] G. Eisenstein, R. S. Tucker, J. M. Wiesenfeld, P. B. Hansen, G. Raybon, B. C. Johnson, T. J. Bridges, F. G. Storz, and C. A. Burrus, “Gain recovery time of traveling-wave semiconductor optical amplifiers,” *Appl. Phys. Lett.* **54**(5), 454-

456 (1989)

[120] W. R. Bosenberg, A. Drobshoff, J. I. Alexander, L. E. Myers, and R. L. Byer, "Continuous-wave singly resonant optical parametric oscillator based on periodically poled LiNbO3," *Opt. Lett.* **21**(10), 713-715 (1996)

[121] R. H. Stolen and J. E. Bjorkholm, "Parametric amplification and frequency conversion in optical fibers," *IEEE J. Quantum Electron.* **18**(7), 1062-1072 (1982)

[122] S. Radic and C. J. McKinstrie, "Optical parametric amplification and signal processing in highly-nonlinear fibers," *IEICE Trans. Electron.* **88**(5), 859-869 (2005)

[123] M. E. Marhic, K. K. Y. Wong, M. C. Ho, and L. G. Kazovsky, "92% pump depletion in a continuous-wave one-pump fiber optical parametric amplifier," *Opt. Lett.* **26**(9), 620-622 (2001)

[124] C. J. McKinstrie, S. Radic, and A. R. Chraplyvy, "Parametric amplifiers driven by two pump waves," *IEEE J. Sel. Top. Quantum Electron.* **8**(3), 538-547 (2002)

[125] S. Oda, H. Sunnerud, and P. A. Andrekson, "High efficiency and high output power fiber-optic parametric amplifier," *Opt. Lett.* **32**(13), 1776-1778 (2007)

[126] S. Radic, C. J. McKinstrie, R. M. Jopson, J. C. Centanni, and A. R. Chraplyvy, "All-optical regeneration in one- and two-pump parametric amplifiers using highly nonlinear optical fiber," *IEEE Photon. Technol. Lett.* **15**(7), 957-959 (2003)

[127] T. Okuno, T. Nakanishi, M. Hirano, and M. Onishi, "Practical considerations for the application of highly nonlinear fibers," in *Proc. OFC 2007*, Anaheim, 2007, p. OTuJ1.

[128] R. E. Slusher, G. Lenz, J. Hodelin, J. Sanghera, L. B. Shaw, and I. D. Aggarwal, "Large Raman gain and nonlinear phase shifts in high-purity As2Se3

chalcogenide fibers," *J. Opt. Soc. Am. B* **21**(6), 1146-1155 (2004)

[129] R. K. W. Lau, M. Menard, Y. Okawachi, M. A. Foster, A. C. Turner-Foster, R. Salem, M. Lipson, and A. L. Gaeta, "Continuous-wave mid-infrared frequency conversion in silicon nanowaveguides," *Opt. Lett.* **36**(7), 1263-1265 (2011)

[130] S.Zlatanovic, J. S. Park, S.Moro, J. M. C. Boggio, I. B. Divliansky, N.Alic, S.Mookherjea, and S.Radic, "Mid-infrared wavelength conversion in silicon waveguides using ultracompact telecom-band-derived pump source," *Nat. Photonics* **4**(8), 561-564 (2010)

[131] E. Brainis, D. Amans, and S. Massar, "Scalar and vector modulation instabilities induced by vacuum fluctuations in fibers: Numerical study," *Phys. Rev. A* **71**(2), 023808 (2005)

[132] F. Yaman, Q. Lin, S. Radic, and G. P. Agrawal, "Impact of Dispersion Fluctuation on Dual-Pump Fiber-Optic Parametric Amplifiers," *IEEE Photon. Technol. Lett.* **16**(5), 1292-1294 (2004)

[133] H. A. Haus and J. A. Mullen, "Quantum Noise in Linear Amplifiers," *Phys. Rev.* **128**(5), 2407–2413 (1962)

[134] K. Tai, A. Hasegawa, and A. Tomita, "Observation of modulational instability in optical fibers," *Phys. Rev. Lett.* **56**(2), 135-138 (1986)

[135] A. F. Milton and W. K. Burns, "Mode coupling in optical waveguide horns," *IEEE J. Quantum Electron.* **13**(10), 828-834 (1977)

[136] Katsunari Okamoto, *Fundamentals of Optical Waveguides*, 1st ed. San Diego, California: Academic Press, 2000.

[137] L. Provino, A. Mussot, E. Lantz, T. Sylvestre, and H. Maillotte, "Broadband and flat parametric amplifiers using a multisection dispersion-tailored nonlinear fiber arrangement," *J. Opt. Soc. Am. B* **20**(7), 1532-1537 (2003)

[138] S. Moro, E. Myslivets, J. R. Windmiller, N. Alic, J. M. Chavez Boggio, and S. Radic, “Synthesis of equalized broadband parametric gain by localized dispersion mapping,” *IEEE Photon. Technol. Lett.* **20**(23), 1971-1973 (2008)

[139] S. Radic, C. J. McKinstrie, A. R. Chraplyvy, G. Raybon, J. C. Centanni, C. G. Jorgensen, and K. Brar and C. Headley, “Continuous-Wave Parametric Gain Synthesis Using Nondegenerate Pump Four-Wave Mixing,” *IEEE Photon. Technol. Lett.* **14**(10), 1406–1408 (2002)

[140] T. Torounidis and P. Andrekson, “Broadband Single-Pumped Fiber-Optic Parametric Amplifiers,” *IEEE Photon. Technol. Lett.* **19**(9), 650-652 (2007)

[141] A. Legrand, C. Simonneau, D. Bayart, A. Mussot, E. Lantz, T. Sylvestre, and H. Maillote, "Impact of the longitudinal variations of the chromatic dispersion on the gain of fiber parametric amplifiers," in *Optical Amplifiers and Applications*, Otaru, 2003, pp. Tu-31.

[142] M. Farahmand and M. de Sterke, “Parametric amplification in presence of dispersion fluctuations,” *Opt. Express* **12**(1), 136-142 (2004)

[143] K. Tsuji, H. Yokota, and A. M. Saruwatari, “Influence of dispersion fluctuations on four-wave mixing efficiency in optical fibers,” *Electronics and Communications in Japan (Part II: Electronics)* **85**(8), 16-24 (2002)

[144] T. Peyronel, O. Firstenberg, Q. Y. Liang, S. Hofferberth, A. V. Gorshkov, T. Pohl, M. D. Lukin, and V. Vuletic, “Quantum nonlinear optics with single photons enabled by strongly interacting atoms,” *Nature* **488**(7409), 57-60 (2012)

[145] A. V. Gorshkov, J. Otterbach, M. Fleischhauer, T. Pohl, and M. D. Lukin, “Photon-photon interactions via Rydberg blockade,” *Phys. Rev. Lett.* **107**(13), 133602 (2011)

[146] J. C. Lagarias, J. A. Reeds, M. H. Wright, and P. E. Wright, “Convergence properties of the Nelder–Mead simplex method in low dimensions,” *SIAM Journal of Optimization* **9**(1), 112-147 (1998)

[147] R. L. Mozzi and B. E. Warren, "The structure of vitreous silica," *J. Appl. Cryst.* **2**(4), 164-172 (1969)

[148] M.E. Marhic, G. Kalogerakis, and L.G. Kazovsky, "Gain reciprocity in fibre optical parametric amplifiers," *Electron. Lett.* **42**(9), 519-520 (2006)

[149] P. A. Franken, A. E. Hill, C. W. Peters, and G. Weinreich, "Generation of Optical Harmonics," *Phys. Rev. Lett.* **7**(4), 118-119 (1961)

[150] R. H. Stolen and A. Ashkin, "Optical Kerr Effect in Glass Waveguide," *Appl. Phys. Lett.* **22**(6), 294-296 (1973)

[151] J. Hansryd, P. A. Andrekson, M. Westlund, J. Li, and P. O. Hedekvist, "Fiber-Based Optical Parametric Amplifiers and Their Applications," *IEEE J. Sel. Topics Quantum Electron.* **8**(3), 506-520 (2002)

[152] J. H. Lee, T. Tanemura, K. Kikuchi, T. Nagashima, T. Hasegawa, S. Ohara, and N. Sugimoto, "Experimental comparison of a Kerr nonlinearity figure of merit including the stimulated Brillouin scattering threshold for state-of-the-art nonlinear optical fibers," *Opt. Lett.* **30**(13), 1698-1700 (2005)

[153] G. Li, J. Yao, H. Thacker, A. Mekis, X. Zheng, I. Shubin, Y. Luo, J.-H. Lee, K. Raj, J. E. Cunningham, and A. V. Krishnamoorthy, "Ultralow-loss, high-density SOI optical waveguide routing for macrochip interconnects," *Opt. Express* **20**(11), 12035-12039 (2012)

[154] S. D. Le, M. Gay, L. Bramerie, M. C. e Silva, K. Lenglé, T. Chartier, M. Thual, J. C. Simon, L. Brilland, D. Méchin, P. Toupin, and J. Troles, "Wavelength conversion in a highly nonlinear chalcogenide microstructured fiber," *Opt. Lett.* **37**(22), 4576-4578 (2012)

[155] M. Pu, H. Hu, C. Peucheret, H. Ji, M. Galili, L. K. Oxenløwe, P. Jeppesen, J. M. Hvam, and K. Yvind, "Polarization insensitive wavelength conversion in a dispersion-engineered silicon waveguide," *Opt. Express* **20**(15), 16374-16380 (2012)

[156] M. Westlund, P. A. Andrekson, H. Sunnerud, J. Hansryd, and J. Li, "High-Performance Optical-Fiber-Nonlinearity-Based Optical Waveform Monitoring," *J. Lightwave Technol.* **23**(6), 2012-2022 (2005)

[157] C. S. Brès, A. O. J. Wiberg, B. P. P. Kuo, J. M. Chavez-Boggio, C. F. Marki, N. Alic, and S. Radic, "Optical Demultiplexing of 320 Gb/s to 8 x 40 Gb/s in Single Parametric Gate," *J. Lightwave Technol.* **28**(4), 434-442 (2010)

[158] Z. Tong, C. Lundström, P. A. Andrekson, C. J. McKinstrie, M. Karlsson, D. J. Blessing, E. Tipsuwannakul, B. J. Puttnam, H. Toda, and L. Grüner-Nielsen, "Towards ultrasensitive optical links enabled by low-noise phase-sensitive amplifiers," *Nat. Photonics* **5**(7), 430-436 (2011)

[159] A. O. Wiberg, D. J. Esman, L. Liu, E. Myslivets, N. Alic, and S. Radic, "Photonic RF-Channelized Receiver based on Wideband Parametric Mixers and Coherent Detection," in *CLEO*, San Jose, 2014, p. STu2I.6.

[160] N. Alic and S. Radic, "Optical Frequency Combs for Telecom and Datacom Applications," in *Optical Fiber Communication Conference*, San Francisco, 2014, p. W4E.4.

[161] R. Nissim, A. Pejkic, E. Myslivets, B. P. Kuo, N. Alic, and S. Radic, "Ultrafast optical control by few photons in engineered fiber," *Science* **345**(6195), 417-419 (2014)

[162] A. Pejkic, R. R. Nissim, E. Myslivets, A. O. J. Wiberg, N. Alic, and S. Radic, "Study, All-Optical Switching in a Highly Efficient Parametric Fiber Mixer: Design," *Opt. Express*

[163] E. Myslivets, N. Alic, and S. Radic, "High Resolution Measurement of Arbitrary-Dispersion Fibers: Dispersion Map Reconstruction Techniques," *J. Lightwave Technol.* **28**(23), 3478-3487 (2010)

[164] D. Anderson, "Variational approach to nonlinear pulse propagation in optical fibers," *Phys. Rev. A* **27**(6), 3135-3145 (1983)

[165] Y. Xiao, G. P. Agrawal, and D. N. Maywar, "Nonlinear pulse propagation: A time–transformation approach," *Opt. Lett.* **37**(7), 1271-1273 (2012)

[166] Z. Zhou, S. Jahanmirinejad, F. Mattioli, D. Sahin, G. Frucci, A. Gaggero, R. Leoni, and A. Fiore, "Superconducting series nanowire detector counting up to twelve photons," *Opt. Express* **22**(3), 3475-3489 (2014)